QUANTUM DOT SENSITIZED ESTROGEN RECEPTOR ALPHA-RECOMBINANT PROTEIN ELECTROCHEMICAL BIOSENSOR FOR 17-BETA ESTRADIOL

UNIVERSITY *of the*
WESTERN CAPE

Abongile Nwabisa Jijana

Bsc Honours Chemistry (Cum Laude), MSc Chemistry (Cum Laude)

This thesis is submitted in fulfilment of the requirements for the degree of

Doctor of Philosophy

in the Department of Chemistry, Faculty of Science, at the University of the Western Cape

Supervisor (s):

Professor Emmanuel I. Iwuoha

Professor Priscilla G.L. Baker

March 2016

ABSTRACT

Estrogens play an extraordinary role in the endocrine system regulation through the stimulation and regulation of endocrine pathways. 17β-estradiol is one of the final metabolites in estrogen regulation by hydroxylase enzymes that are well recognized for their metabolic role in hormone fragmentation and dissociation, through hydroxylation reactions that reversibly convert a series of androgens to estrogens (i.e. or one estrogen to the other). However, the 17β-estradiol hormone has been classified as one of the estrogenic endocrine disrupting compounds {i.e. EDC (s)} that show significant adverse effects in the estrogen pathways of male and female animal species. Estrogen receptor alpha (ER-α) is significantly activated by 17β-estradiol, which is a steroid hormone. A biosensor system for the determination of 17β-estradiol was developed based on the highly selective and specific physiological substrate level activation of the ER-α biomolecule by the (17β-estradiol) compound. The chemically-tuned tin selenide quantum dots capped with 3-mercaptopropionic acid were produced at room temperature and employed to capture the ER-α micro-molecule onto the electrode surfaces. These quantum dots possessed average particle size (APS) diameters between 4.6 ± 0.6 nm and an indirect band gap energy (E_g) of 3.14 eV. Surface modification on the quantum dots permitted the formation of efficient amide bonds between the capping molecules of the quantum dots and the estrogen receptor-alpha. The tin selenide quantum dots platform enhanced the surface bio-reactivity of the receptorsensor film. The receptorsensor's sensitivity towards 17β-estradiol was 5.9 µA/µM associated with a response time ($t_{Response}$) of less than 1.2 s. The formal potential, $E_p^{\circ\prime}$, of the receptorsensor-substrate complex was 149 mV. A detection limit (DL) of 1.9 nM was obtained for the electrochemical biosensing methodology. 17β-estradiol–receptorsensor response kinetics were also evaluated, where a dissociation rate (k_d) of 7.6 µM/s, a 50 % inhibition concentration (IC_{50}) value of 3.4 nM and a binding efficiency (B_{max}) of 7 nM were obtained. Effective measure of 17β-estradiol concentrations as low as 3.8 nM present in surface waters have been reported to induce feminisation in male aquatic species. The receptorsensor's dynamic linear range (DLR) nevertheless showed capability of screening a minimum of 0.2 nM to a maximum of 8 nM of the 17β-estradiol concentrations. Furthermore, during the estrogen replacement therapy (ERT), 17β-estradiol concentration levels are monitored at frequent phases, wherein 17β-estradiol concentrations from as low as 0.37 nM are recovered in the serum (i.e. this value was also evaluated to be within the receptorsensor's-DLR), determining its future capability to be developed for; clinical-diagnosis screening of the 17β-estradiol.

KEYWORDS

Amino acids

Proteins

Nuclear receptors {(NR (s)}

Estrogen receptor-alpha (ER-α)

17β-estradiol (E2)

Ligand binding domain (LBD)

Estrogen receptor-α based biosensor (i.e. receptorsensor)

Estrogen receptor-α based biosensor binding kinetics

50 % inhibition concentration (IC_{50})

Dissociation constant (k_d)

Biosensor response time ($t_{Response}$)

Fluorescence spectroscopy

DECLARATION

I declare that "*Quantum Dot Sensitized Estrogen Receptor Alpha-Recombinant Protein Electrochemical Biosensor for 17-Beta Estradiol*" is my own work, that has not been submitted before for any degree or examination in any other university, and that all sources I have used or quoted have been indicated and acknowledged as complete references.

Abongile Nwabisa Jijana March 2016

Signed.....

ACKNOWLEDGEMENTS

I am grateful to God for existence, the opportunities and good health. To my parentage, thank you for not giving up on me, your encouragement and inordinate support, I will enduringly treasure.

To my supervisor Prof. Emmanuel Iwuoha, this attainment would have not been imaginable if it was not for you accepting my proposition to pursue this doctorate degree under your supervision at the SensorLab Research Group. I am as well grateful for the opportunities you offered me to commutate this research's outcomes in a frequent number of international seminars and symposiums.

The capital assistance for this research project was provided by DST/Mintek of South Africa, which I accurately and equally recognize.

LIST OF PUBLICATIONS

1. **Abongile Nwabisa Jijana**, Priscilla G.L Baker and Emmanuel I. Iwuoha, 'Electrochemical estrogen receptor (α)-based biosensor for 17β-estradiol developed from amidation of N-terminus domain of the ER-α integrated with 3-mercaptopropionic acid functionalised SnSe quantum dots', *Electrochimica Acta*, 2016.
2. Peter M. Ndangili, **Abongile N. Jijana**, Priscilla G.L Baker and Emmanuel I. Iwuoha, '3-mercaptopropionic acid capped ZnSe quantum dot-cytochrome P450-3A4 enzyme biosensor for 17β-estradiol', *Journal of Electroanalytical Chemistry*, (2011), 653, , 67-74.
3. Peter M. Ndangili, **Abongile N. Jijana**, Rasaq A. Olowu, Stephen N. Mailu, Fanelwa R. Ngece, Avril Williams, Tesfaye T. Waryo, Priscilla G.L. Baker, Emmanuel I. Iwuoha, 'Impedimetric Response of a Label-Free Genosensor Prepared on a 3-Mercaptopropionic Acid Capped Gallium Selenide Nanocrystal Modified Gold Electrode', *International Journal of Electrochemical Science*, (2011), 6, 1438-1453.
4. E. Nxusani, P.M. Ndangili, R.A. Olowu, **A. N. Jijana**, T. Waryo, N. Jahed, R.F. Ajayi, P. Baker and E. Iwuoha, '3-Mercaptopropionic acid capped Ga2Se3 nanocrystal-CYP3A4 biosensor for the determination of 17-alpha-ethinyl estradiol in water', *Nano Hybrids*, (2012), 1, 1-22.
5. Rachel Ngece, Nicolette Hendricks, Natasha West, Peter M. Ndangili, **Abongile Jijana**, Stephen Mailu, Tesfaye Waryo, Priscilla Baker, Emmanuel Iwuoha, 'A silver nanoparticles-poly(8-anilino-1-naphthalene sulphonic acid) bioelectrochemical sensor system for the analytical determination of ethambutol', In V. Rajendra, B. Hillbrands, P. Prabu and K.E. Geckeler (eds.): *Biomedical Applications of Nanostructured Materials*, Macmillan Publishers India Limited, (2010), Pages 269-274.
6. Fuku, Xolile, Singh, Baljit, Ajayi, Rachel F., **Jijana, Abongile N**. Baker, Priscilla, Dempsey, Eithne, Iwuoha, Emmanuel, 'A gallium telluride quantum dots bioelectrode system for human epidermal growth factor receptor-2 (Her2/neu) oncogene signalling', *Analytical Methods*, (2015), 7, 6114-6124.

LIST OF FIGURES

TABLE OF CONTENT

RESEARCH PROJECT MAP

The presented research was formulated through the herein recognised scheme.

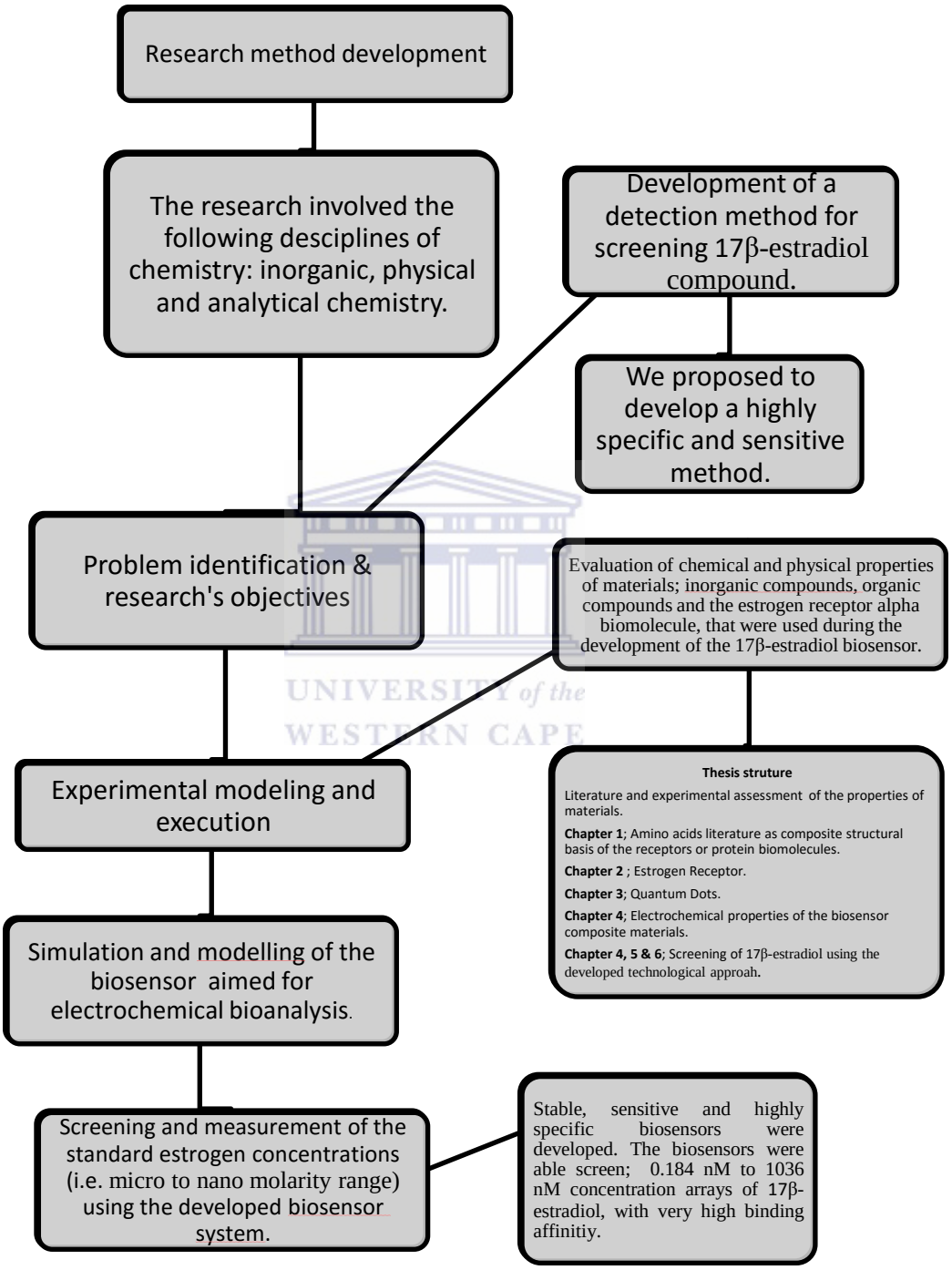

Figure O-A: The research thesis outline.

Chapter 1 Review of amino acids

This designated chapter is dedicated for reviewing the background theory related to amino acids, which are intrinsic in polypeptide biosynthesis. Estrogen receptor alpha (ER-α) is a type of nuclear receptor that is known to be activated by an endogenous and exogenous hormone, 17β-estradiol. Assessment of the diverse classes of receptors was drawn attention to, in section 1.5 of this chapter, illustrating a diverse division of nuclear receptors.

1.1. Description of amino acids.

Amino acids are organic compounds that possess chemical structures associated with the presence of: a carboxylic acid group, an amine group, and a chemical active R-group in their backbone structure (i.e. herein, R represents any other functional groups in association with the primary alkyl backbones of amino acids). A basic structure of an amino acid is highlighted in Figure 1 (Rios, Amyes et al. 2000, Ohno and Fukumoto 2007, Held, Cameretti et al. 2011).

Figure 1: Primary backbone structure of amino acids.

Amino acids are classified into several categories in relation to the attachment position of the chemical active groups on their backbone structures (i.e. the unique R-group with distinct polarity level, pH and chemical properties) (Creighton 1993, Walsh 2002, Na and Olson 2007, Northrop 2010).

1.1.1. Classification of amino acids, by their length.

Amino acids are defined by the nature of the linked R-functional groups in their carbon backbone structures. Moreover, amino acids can be classified through the amine group positions that are related to the length of their alkyl backbone usually derived from the α-carbon positions. A chemical structure of the n-length amino acid is defined in Figure 2 (i.e. n is the number of carbon atoms present in an alkyl backbone of an amino acid including the carbon atom where the amine

group and carboxylic acid groups are linked). Briefly, beta (β) amino acids adopt structures wherein the amine groups are linked at the β-carbon atoms. Relatively, α-amino acids have amine groups that are linked at the α-carbon atom (Shanzer, Somekh et al. 1979, Mishra 2010). An n-length α-amino acid is shown in the next figure, Figure 2.

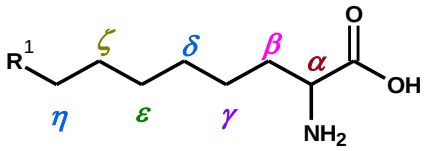

Figure 2: The chemical structure of an n-length amino acid (i.e. R^1 represents the continuation of the alkyl chain).

A number of amino acids possess shorter alkyl chains, in this regard; carboxylic acid groups and amine groups are attached at the α-carbon atoms. A typical molecule is a glycine (Gly) amino acid, wherein; a hydrogen atom, an amine ($-NH_2$) group and a carboxyl acid (-COOH) group are linked at the α-carbon atom (Rios, Amyes et al. 2000, Ohno and Fukumoto 2007, Held, Cameretti et al. 2011). The structure of a Gly amino acid is presented in Figure 3. All amino acids with carboxylic acid groups and amine groups linked through the α-carbon positions are proteinogenic, coined by their involvement in the polypeptide and protein synthesis (Walsh 2002, Rehm 2006).

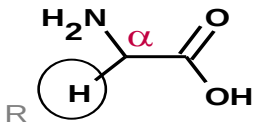

Figure 3: A chemical structure of a glycine (Gly) amino acid.

As highlighted in the structure presented in Figure 3, the R-group of any amino acid may consists of alkyl, cyclic-alkyl, aromatic, hydroxyl, sulfhydryl, and any other chemical reactive groups. Proteinogenic, α-amino acids are intrinsic residues in protein synthesis. A summary of proteinogenic amino acids; categorized by their reactive R-groups are illustrated in the next section; section 1.1.2.

1.1.2. Classification of amino acids by their R-functional groups.

A classified structural description of amino acids is represented through Figure 4 to Figure 9.

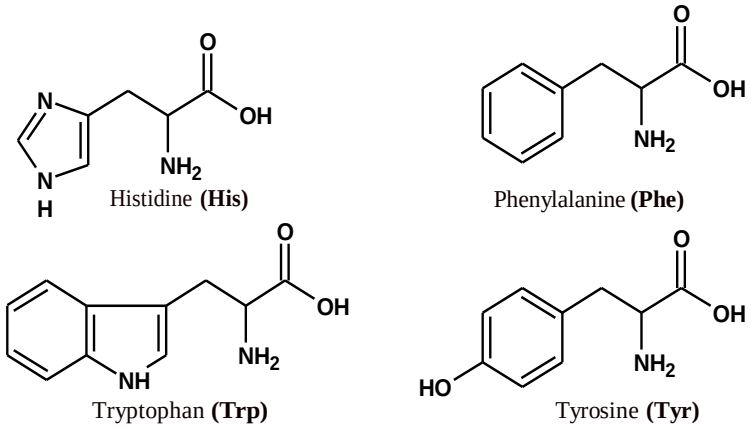

Figure 4: Chemical structures of class-1: aromatic amino acids.

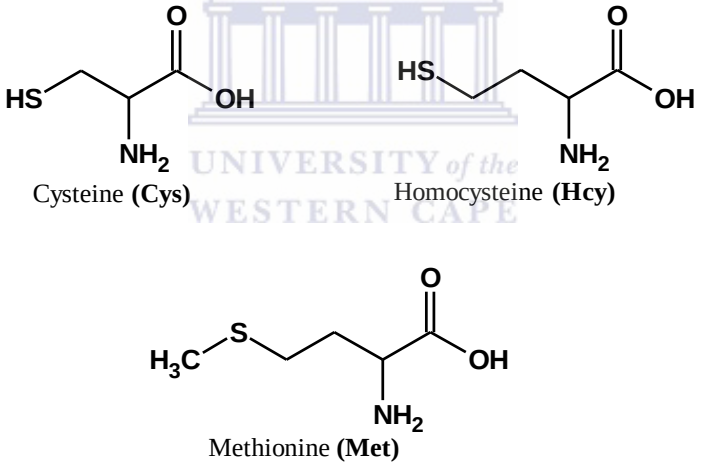

Figure 5: Chemical structures of class-2: thiol amino acids.

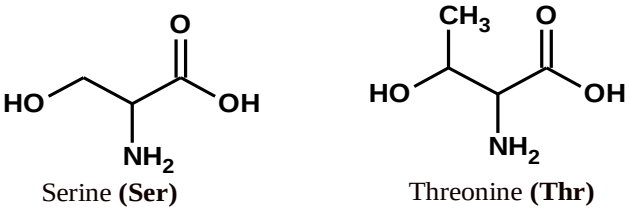

Figure 6: Chemical structures of class-3: hydroxyl amino acids.

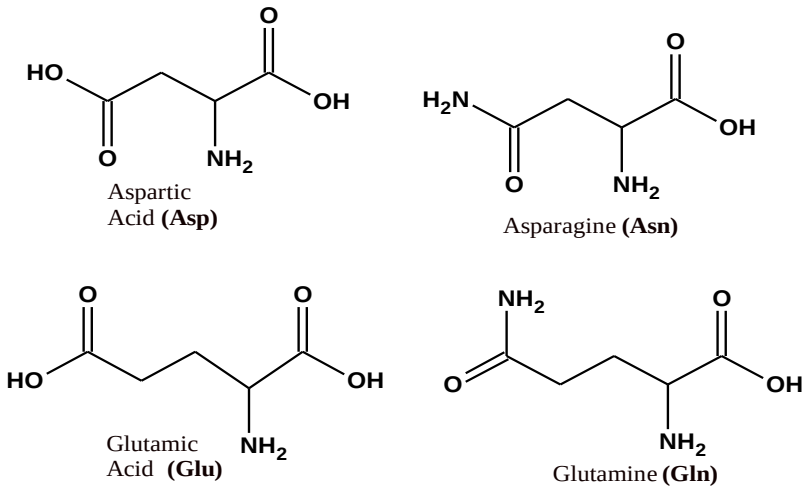

Figure 7: Chemical structures of class-4: carboxyl amino acids.

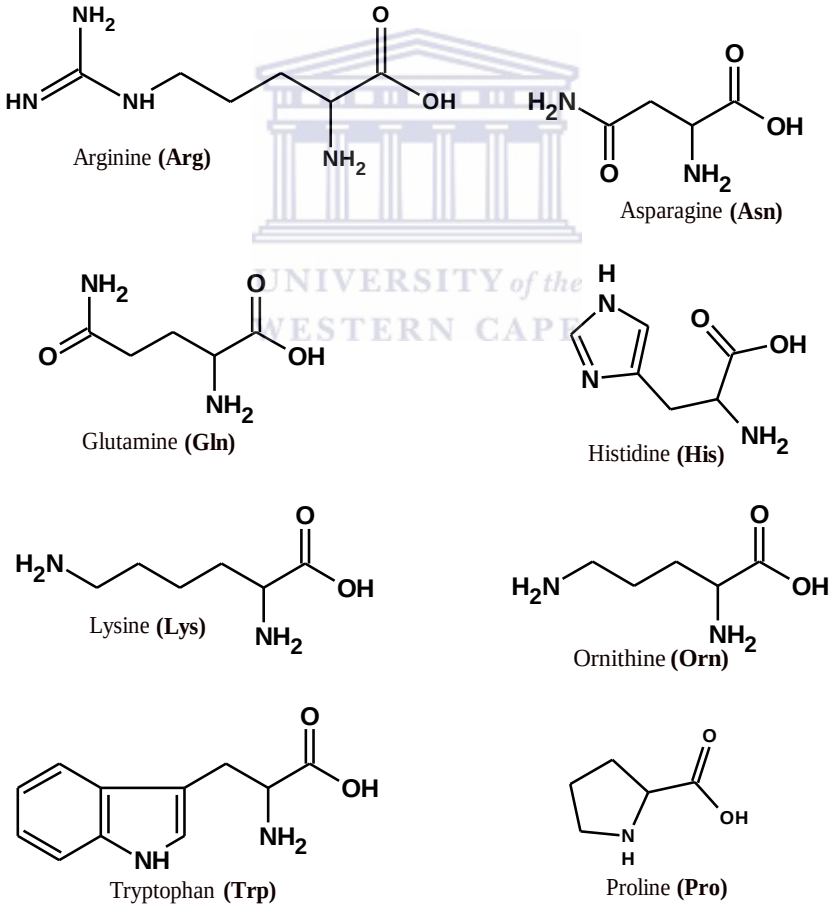

Figure 8: Chemical structures of class-5: amine amino acids.

1.1.3. Classification of amino acid by: the PH, polarity level and chemical structural properties.

Zwitterion is a neutral molecule with a single or multiple positive and negative electrical charges (Walsh 2002, Righetti 2005, Mishra 2010, Xu, Hu et al. 2015). Amino acids are classified as Zwitterions because they consists of slightly positive amine and slightly negative carboxylic acid groups. This implies that any ionization on the amino acid, depending on the solution pH, can occur at either; the amine group or the carboxyl group (Rios, Amyes et al. 2000, Otero and Urquhart 2006, Tian, Wang et al. 2009). The phenomenal ionization characteristics of amino acids is then triggered distinctively by the aqueous medium pH. The amino acid's behaviour at distinct solution pH(s) are highlighted through chemical reactions labelled (1) and (2) in Figure 9.

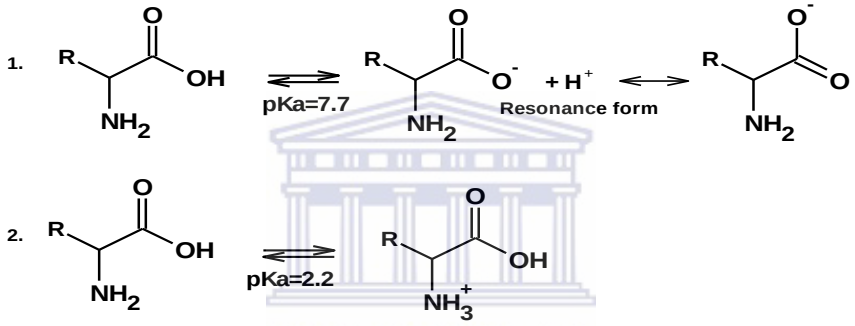

Figure 9: Protonation and deprotonation reaction of the R-linked amino acid Zwitterions at pK_a= 2.2 and pK_a = 7.7.

At acidic medium (i.e. p_{Ka}< 2.2, a pH that is greater than the p_{Ka} value of a carboxylic group), the carboxylic acid is deprotonated acting as a weak conjugate acid. Relatively, at P_{Ka} values greater than 7.7, amino acids are prone to protonation reactions at the ($-NH_2$) functional groups resulting in the conversion of secondary amines to primary amines ($-NH_3^+$).

1.2. Resonance distribution in amino acids.

Resonance structures are observed in molecules when the electrons or negative charges are distributed or delocalized over the molecule or a functional group. Comparatively, mesomerism is a common behaviour adopted by: amino acids, carboxylic acids and ionisable acidic/basic species (Strohmeier, Stueber et al. 2003, Zhong, Patskovskyy et al. 2004). Resonance is known to lower the potential energy of molecules or anions; in this regard, molecules with low resonance energy

tend to exhibit great stability. Relatively, acid-base properties adopted by amino acids can be dependent on the presence of the R-linked ionisable moieties (i.e. the -aryl, -thiol and –hydroxyl functional groups) on amino acids; backbone structures. Thus, mesomerism in amino acids is usually observed at the R-side groups due to the reactivity of the R-linked functional groups. The resonance distributions in different classes of amino acids are thoroughly described in the next section; section 1.2.1.

1.2.1. Resonance distribution and reactivity of amino acids.

Arginine (Arg) amino acid reactivity can be accounted for, by the presence of a guanido group (i.e. $-NH_2-C(=NH_2^+)NH-$) (Julian, Beauchamp et al. 2002, Remko, Fitz et al. 2008). The guanido group at basic solution pH's (i.e. pKa values of 12 and greater) acts as a weak acid. In this regard, the abstraction of a hydrogen atom at this group would result into generation of a reactive lone pair of electrons at the nitrogen group, giving the molecule more than one possible resonance configuration, this behaviour adopted by the Arg amino acid is described through the chemical reaction presented in Figure 10.

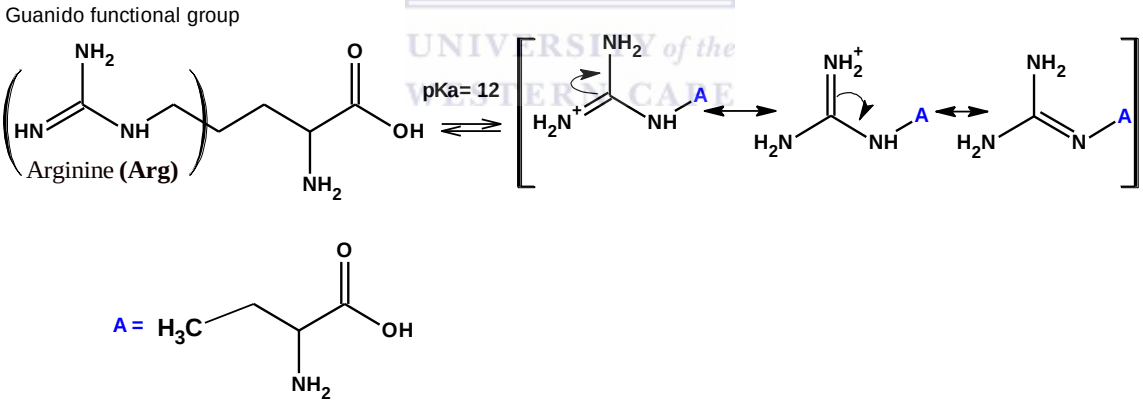

Figure 10: Resonance energy distribution in an arginine (Arg) amino acid.

At physiological acidic pHs, the positive charge carried by the hydrogen atom is delocalized at the guanido moiety stabilizing the molecule over the carbon and nitrogen atoms (Andriole, Colyer et al. 2006). The arginine (Arg) along with lysine (Lys), histidine (His) and ornithine (Orn), possess net positive charges due to the ionisable amine R-side groups present in their structures (i.e. the chemical structures of these amino acids were previously described in Figure 8). Relatively, the amine amino acids; asparagine (Asn) and glutamine (Gln) are denoted by the presence of the ester-

amide moiety (i.e. -C=O(NH_2)) at their amino acid carbon backbones. In Asn, the (-C=O(NH_2) is attached at the β-carbon atom. In Gln, the (-C=O(NH_2) group is linked at the γ-carbon atom. The ester-amide (i.e. -C=O(NH_2) groups in these amino acids contribute to their chemical reactivity and behaviour. Aspartic Acid (Asp) and glutamic acid (Glu) are acidic forms of Asn and Gln respectively. The resonance distribution in the Asp amino acid is shown in Figure 11.

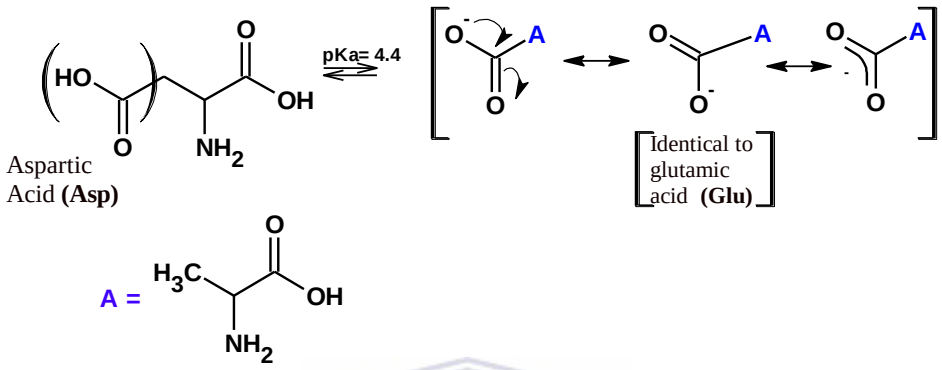

Figure 11: Resonance energy distribution in an aspartic acid (Asp); that is relatively identical to the behaviour of glutamic acid (Glu) and other carboxyl amino acids.

These amino acids are neutrally charged at physiological conditions but intrinsically polar (Walsh 2002, Rehm 2006). When present in a peptide chain, Asn and Gln possess completely different physical and chemical properties related to the; coordination, conformation, and chemical reactivity adopted by a peptide structure. However, the acid conjugate derivatives of these amino acids (i.e. aspartic acid (Asp) and glutamic acid (Glu)) are more reactive than their amide derivatives; Asn and Gln respectively. This is due to the R-linked carboxyl acid functional groups (i.e. –COOH groups) present in their structures, that are susceptible to esterification, amidation and halogenations reactions (Nagy and Noszál 2000, Walsh 2002, Catak, Monard et al. 2008). Histidine (His) is a proteinogenic amino acid associated with a β-carbon hinged R-imidazole chemical reactive ring, highlighted in a structure shown in Figure 12. The chemical behaviour of His is on account of the R-functional group-linked imidazole moiety (Kafka, Kleffmann et al. 2009). The resonance distribution in a His amino acid is described, in Figure 12.

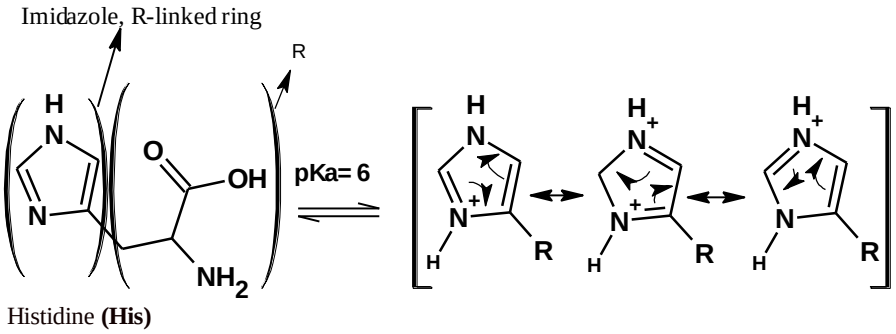

Figure 12: Resonance energy distribution in a histidine (His) amino acid.

At pK_a values, less than 6, His adopts a resonance corresponding to a liable positive charge distributed over the nitrogen atoms of the imidazole functional group affecting its stability and reactivity (Ivanov, Chen et al. 2006, Li and Hong 2011). Under the predefined resonance effect, the imidazole ring becomes positively charged, in spite of electrons delocalized over the entire ring. The un-ionized form of the imidazole ring is known to exist in the presence of a catalytic nucleophile and is known to be highly reactive (Li and Hong 2011). The relative resonance distribution in an imidazole moiety of the His amino acid is described in Figure 12. The protonated imidazole ring is highly aromatic due to possible delocalization of electrons over the imidazole ring at pH values below its acid dissociation value (pKa); of 6. The aromatic amino acids; phenylalanine (Phe), tryptophan (Trp) and tyrosine (Try) show significant aromaticity related to R-side groups associated with the present aromatic R-linked functional groups. In Trp amino acid, the extant indole molecule adopts the aromaticity. Furthermore, in Phe and Try, the aromaticity is adopted by the phenyl and phenol rings respectively. The resonance-electron energy distribution in these classified aromatic amino acids is described in Figure 13.

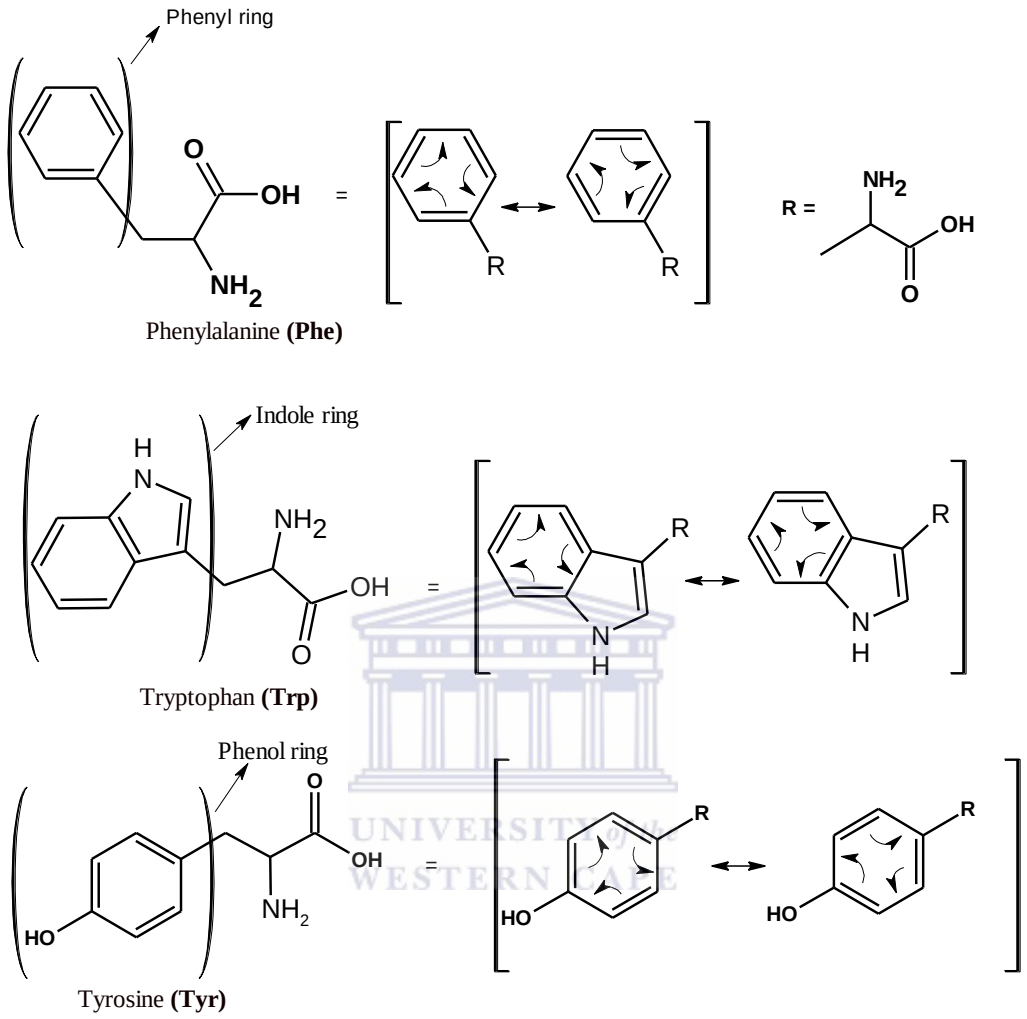

Figure 13: Resonance energy distribution in a phenyl ring of a phenylalanine (Phe) amino acid, an indole ring of a tryptophan (Trp) amino acid and a phenol ring of a tyrosine (Tyr) amino acid.

These amino acids are expectedly highly reactive due to the aromatic R-side groups having high nucleophilicity, on account of the delocalized π-electrons on their aromatic rings. Cysteine (Cys) amino acid consists of a sulfhydryl group at the β-C atom position; the sulfonyl R-functional group is highly reactive, at medium pKa values between 9.5 and 9.0 and acts as a weak acid. High reactivity in the thiol-linked amino acids namely: cysteine, homo-cysteine (Hcy) and methionine (Met) is correlated to the accessibility of sulfhydryl groups present in these amino acids that is capable of forming highly polar covalent bonds between other sulphur ions and show great

chelating affinity with transition metals, which stems from thiol groups having great affinity for the metal ions. When present within a peptide chain Cys readily form di-sulphide linkages that are exceedingly intrinsic in peptide folding and peptide stability (Creighton 1993, Bolstad, Botelho et al. 2010, Mishra 2010). A list of proteinogenic amino acids outlining their chemical properties is illustrated in Table 1 of section 1.3.

1.3. Proteinogenic α-amino acids with their chemical properties:

Table 1: Twenty proteinogenic amino acids: their chemical properties and polarity characteristics. (Garidou, Laffont et al. 2004)

Amino Acid	Abbreviation	Symbol	Molar Mass (/g/mol)	Polarity and Charge
Alanine	(Ala)	A	89	Non Polar
Arginine	(Arg)	R	174	(+) Polar
Asparagine	(Asn)	N	132	Polar
Aspartic Acid	(Asp)	D	113	(-) Polar
Cysteine	(Cys)	C	121	Non Polar
Glutamine	(Gln)	Q	146	Polar
Glutamic Acid	(Glu)	E	147	(-) Polar
Glycine	(Gly)	G	75	Non Polar
Histidine	(His)	H	155	(+) Polar
Isoleucine	(Ile)	I	131	Non Polar
Leucine	(Leu)	L	131	Non Polar
Lysine	(Lys)	K	146	(+) Polar
Methionine	(Met)	M	149	Non Polar
Phenylalanine	(Phe)	F	165	Non Polar
Proline	(Pro)	P	115	Non Polar
Serine	(Ser)	S	105	Polar
Threonine	(Thr)	T	119	Polar
Tyrosine	(Tyr)	Y	181	Polar
Tryptophan	(Typ)	W	204	Non Polar
Valine	(Val)	V	117	Non Polar

1.4. A review section on peptide and polypeptide development.

1.4.1. Peptide development.

A peptide is described as a chain of amino acids that are linked by peptide or amide bonds. Proteins are a series of hinged polypeptides usually infused with biological molecules such as: metals, ligands, co-enzymes, co-factors, co-activators, DNA, and other proteins (Creighton 1993, Wu and Wang 2001, Adhikar and Scheiner 2013). A protein may have an adopted primary structure or a more complex tertiary structure stabilized by internal interactions with the conjugated microbiological units present in its complex structure. A particular paradigm of a polypeptide-chain development mechanism is outlined in Figure 14.

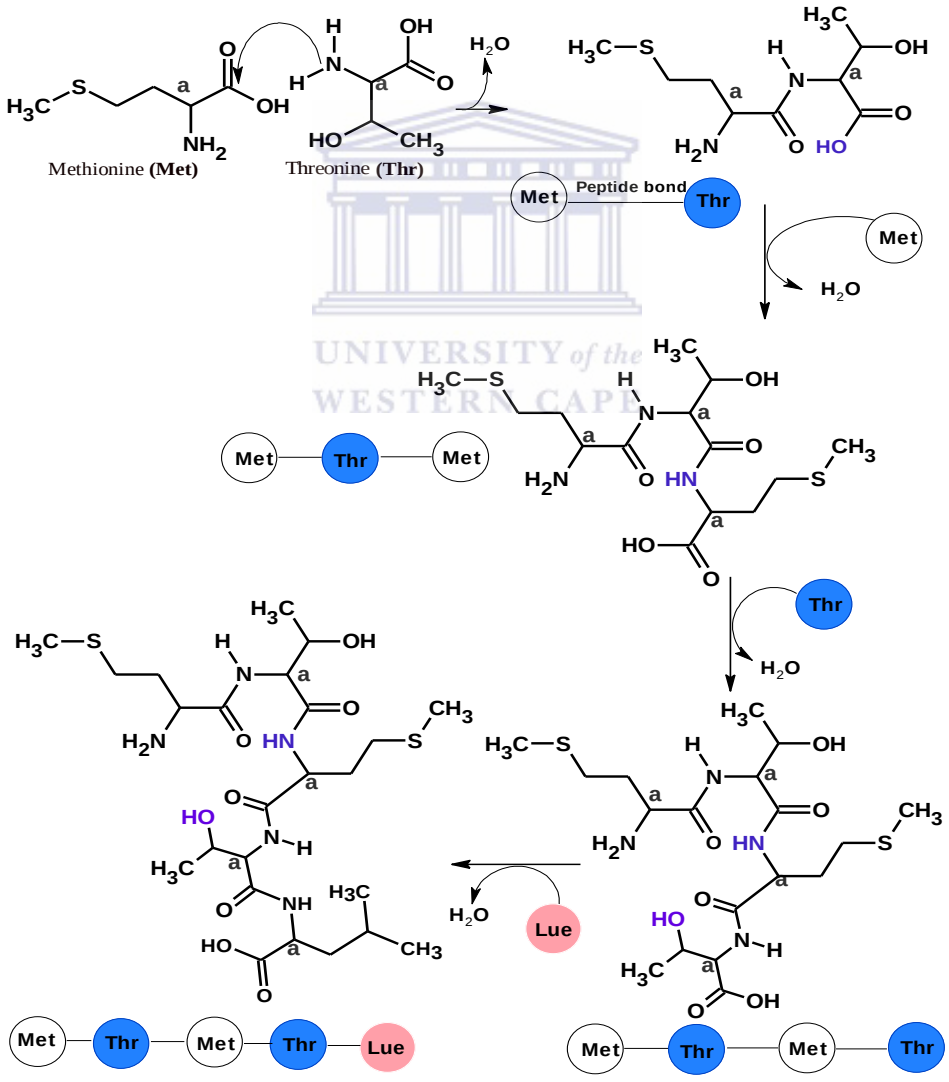

Figure 14: Development of a polypeptide chain.

A synthesis route to a short peptide; Met-Thr-Met-thr-Lue {i.e. methionine (Met), threonine (Thr) and leucine (Lue)} is herein, discussed. Methionine (Met) is usually present as the start codon for the synthesis of many mRNA coded proteins and is usually located at the N-terminus of a polypeptide chain (Creighton 1993, Rehm 2006, McMurry, Ballantine et al. 2013). Met amino acid consists of a short alkyl residue with a sulfhydryl group at the γ-carbon atom. The development of the herein described peptide chain involves; a carbodiimidation reaction between first the; Met and the Thr amino acids, at both the α-carbon linked amine and carboxylic acid groups, respectively resulting in the formation of a covalent amide bond, followed by a dehydration reaction; in a reaction mechanism that is described in Figure 14. The resultant amide-peptide link (i.e. -NH(C=O)) between molecules of these two amino acid residues; 1-(amino-threonine) and Met, have proteinogenic integrity and an amine group of the next amino acid will react in a chain amidation reaction, with the liable carboxylic acid group of the 1-(amino-threonine) amino acid residue. The polypeptide elongation reaction proceeds in due of; a liable α-carboxyl acid group insert on the peptide chain that retains its carboxyl integrity during the peptide bond formation, which then becomes accessible for the next amino acid assembly. Peptide bond is an exceedingly rigid bond associated with a bond length of approximately 1.33 Å, reported by (Creighton 1993, Rehm 2006), nevertheless could undergo very slow hydrolysis resulting in the formation of the (-NH_2) linked and the (-HOC=O) linked peptide by-products. The length of a peptide or a polypeptide chain may vary from 50 to 2500 amino acid residues. It can be noted that during elongation of a peptide chain through condensation reactions of amino acids and the peptide residues, the amine group (-NH_2) at the primary terminus of the peptide chain remains intact; this polypeptide terminus is termed the amine terminus (i.e. N-terminus) of the protein. Consequently, the peptide linked free carboxylic acid group (-HOC=O) can participate in a peptide chain elongation and is termed the carboxyl terminus (i.e. C-Terminus) of the polypeptide.

1.4.2. Conformations adopted by the polypeptide chains, related to the stability of the protein molecules.

Functional groups associated with amino acid residues present in a polypeptide contribute to its chemical reactivity. The orientation and positions of these functional groups in a peptide or a polypeptide chain greatly affect the steric hindrance of the entire peptide chain resulting in static dynamisms of the molecule, seeking to adopt a stable conformation (Michalet, Weiss et al. 2006,

Sugase, Dyson et al. 2007, Dominak, Gundermann et al. 2010). For minimal steric hindrance, the peptide link allows the peptide bonds to adopt either trans or cis configurations that are related to the R-functional groups around the peptide bonds (Creighton 1993, Walsh 2002), to allow free rotation of N-αC and C-αC bonds (Tsujishita, Moriguchi et al. 1993). Figure 15, shows a structural configuration around an amide bond of a typical peptide link (i.e. herein R refers to any peptide link). For a cis-isomerism, the angle of rotation becomes 180°, contradictory in a trans arrangement, the rotation angle becomes 0°. These rotation angles have notations; fi (Ψ) for the N-αC bonds and y (Φ) in the case of C-αC bonds and are illustrated in Figure 15.

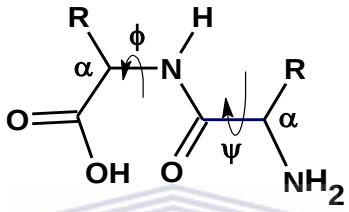

Figure 15: The Ramachandran angles in a peptide bond.

Ramachandran plot of (Φ vs Ψ) rotational angles, details the angle of rotational freedom around each N-αC and C-αC bonds (Yang, Larios et al. 2003, Ho and Brasseur 2005, Carugo and Carugo 2013, DasGupta, Kaushik et al. 2015). A greater angle of rotation is obtained in the case of less bulky R-groups. The rotational angles Φ and Ψ in a peptide chain are the contributing keys to predicting the energetically favoured conformation the polypeptides will adopt. The change of rotation or conformation in a polypeptide molecule can be; in addition evaluated by determining its relaxation time. Relaxation time refers to the time, a molecule takes to change from one state by a magnitude of e^{-1} from its equilibrium (Creighton 1993, Walsh 2002, Ye, Demidov et al. 2003, Gitti, Wright et al. 2005) and is expressed as the function of time (s), as highlighted in next equation; Equation 1.

$$Relaxation\ time = e^{t/\tau}$$

Equation 1

Relaxation times of the peptide chains and carbon atoms can be measured using ^{13}Carbon nuclear magnetic resonance (^{13}C-NMR) spectroscopy, which measures the relaxation times at the α-C

atoms around the peptide bonds. A polypeptide residue can thus adopt many possible rotation modes by adopting either; cis or trans configurations, around the peptide bonds to attain stability and equilibrium. The magnitude of the Φ and Ψ tetrahedral angles determine the possible rotation adopted by peptides such as; coiling and folding, depending on the nature of amino acid residues present.

1.4.3. Chemical sequencing of peptide structures.

A peptide chain sequence can be distinctively determined from the amino acid sequence (Walsh 2002, Mishra 2010, Berg, Tymoczko et al. 2002). The amino acid sequence is frequently referred to as the primary structure of; a polypeptide or a protein molecule. Sequencing shorter length polypeptides or peptides involves a simplified process, than in the case of elongated peptide chains. This is due to fractional complexity of shorter polypeptides': structure, amino acid sequence residues, and the polypeptides intermolecular interactions, that can be effortlessly resolved. Amino acid sequencing examines the protein's; chemical and biological properties and can consecutively, be used for identification of its structure and conformation probabilities. The length of the recognised peptide chain model outlined in Figure 16 is a 30-unit amino acid peptide. The methionine (Met) present as the initiator codon at the primer region has a free amine group located at the peptide's N-terminus.

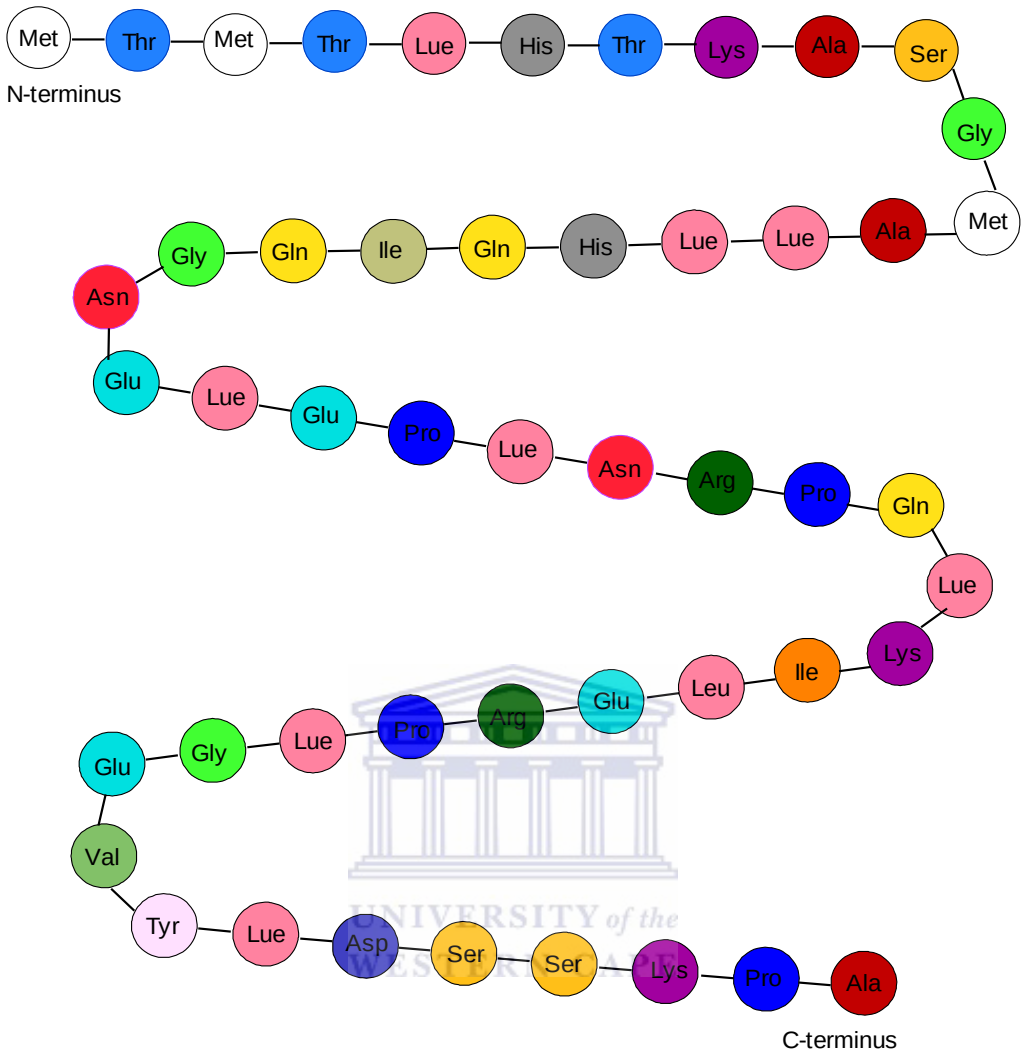

Figure 16: A cartoon-model of the primary structure of a peptide chain with exposed C-terminus and N-terminus.

It can be noted that; in the chemical structure of Met amino acid, explained in the previous section (i.e. section 1.4.1), that the amine group (i.e. NH_2) of the initiator amino acid retains its character and is not affected by the peptide chain elongation. The C-terminus of the peptide chain, outlined in Figure 16 is associated with an amino acid: Alanine (Ala). Alanine amino acid residue at the N-terminus of the described peptide has a free carboxylic acid. The carboxylic acid group on the alanine residues is also liable for the next amidation reaction, thus the C-terminus of the peptide or the polypeptide is highly reactive side and negatively charged, due to the possible delocalization of electrons at the free carboxylic acid group.

1.4.4. Chemical reactivity of proteins.

Disulphide bridges (i.e. S-S bridges) in peptides and proteins are vastly dependent on the number of thiol-containing amino acid residues: cysteine (Cyst) and methionine (Met) within peptides or polypeptide chains. Formation of S-S bridges in peptides or polypeptides transform primary structures of proteins into more intricate secondary and tertiary 3-dimensional structures (Darby and Creighton 1995, Bolstad, Botelho et al. 2010, Mishra 2010, Vo-DinH 2010). The studies involving protein biomolecules take into account understanding the conformations; folding and binding mechanisms of the polypeptides or protein biomolecules (Fischer and Schmid 1990, Darby and Creighton 1995, Benner, Cannarozzi et al. 1997, Déméné and Sugàr 1999, Okimoto, Nakamura et al. 2004). However, the conformations of proteins are essentially dependent on the chemical induced interactions between the amino acids present in their primary structures. A list of possible reactions of α-amino acids associated with the polypeptide biomolecules are outlined in Figure 17 (Shonle and Mitchell 1920, Suzuki, Iwasaki et al. 1973, Garcia-Raso, Deya et al. 1986, Jackson, Wishart et al. 1992, Roos, Lopez et al. 1993, Walsh 2002, Mishra 2010, Reynolds 2014).

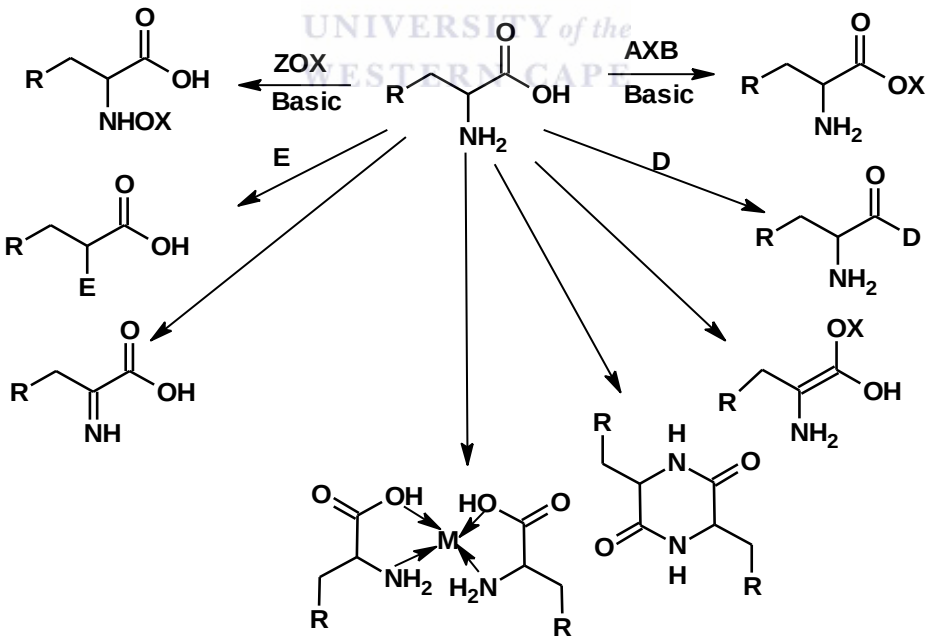

Figure 17: Potential chemical reactions of amino acid residues in polypeptides (i.e. R is any function group).

1.4.5. Biosynthesis of proteins from mRNA(s).

Protein micro-molecules are associated with peptide chains of amino acids linked together by peptide bonds or amide bonds. However, proteins are biologically synthesized from mRNA strands encoded with a genetic nucleotide sequence that codes for a unique protein amino acid sequence. The process of mRNA coded protein, synthesis mechanism is shown in Figure 18 (Walsh 2002, Ataide and Ibba 2006, Rehm 2006, Mittendorf, Deatherage et al. 2012, Barendt, Ng et al. 2013, Yanagawa 2013).

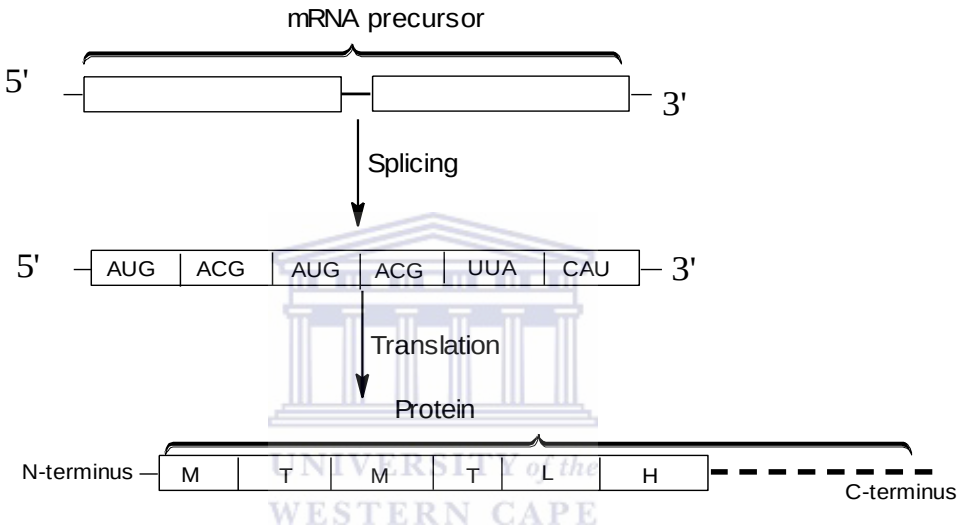

Figure 18: A synthesis route to an mRNA encoded peptide chain (i.e. MTMTLH).

The synthesis of the pre-described peptide sequence; MTMTLH is herein, discussed.

- A transcribed mRNA precursor encoded with a genetic code sequence after transcription and gene regulation, is released as a split segment.
- Precursor fragmented segments of the mRNA oligonucleotide are released for the next synthesis process to incur.
- Splicing of the oligonucleotide sequence segments of the polypeptide precursor; mRNA results in an oligonucleotide single strand mRNA; with an initiator and terminator primer; terminuses 5' and 3'; shielding the cistron encoding mRNA oligonucleotide sequence.
- Cistron/mRNA oligonucleotide sequence shielded by the N-terminus and C-terminus undergoes translation into a protein sequence.

- The protein sequence is comparative to a unique code translated from the mRNA oligonucleotide sequence {i.e. the AUG encoding from the mRNA, codes for the methionine (Met) α-amino acid}.

1.5. Categories of proteins and their binding mechanisms.

1.5.1. Signal transduction in integral membrane proteins.

Membrane integrated proteins have a peptide sequence forming part of the membrane (Zhao, Zhang et al. 2004, Pan, Stocks et al. 2009, Whitelegge 2013). A scheme outlined in Figure 19, shows the broad description of different types of proteins secreted in the plasma membrane.

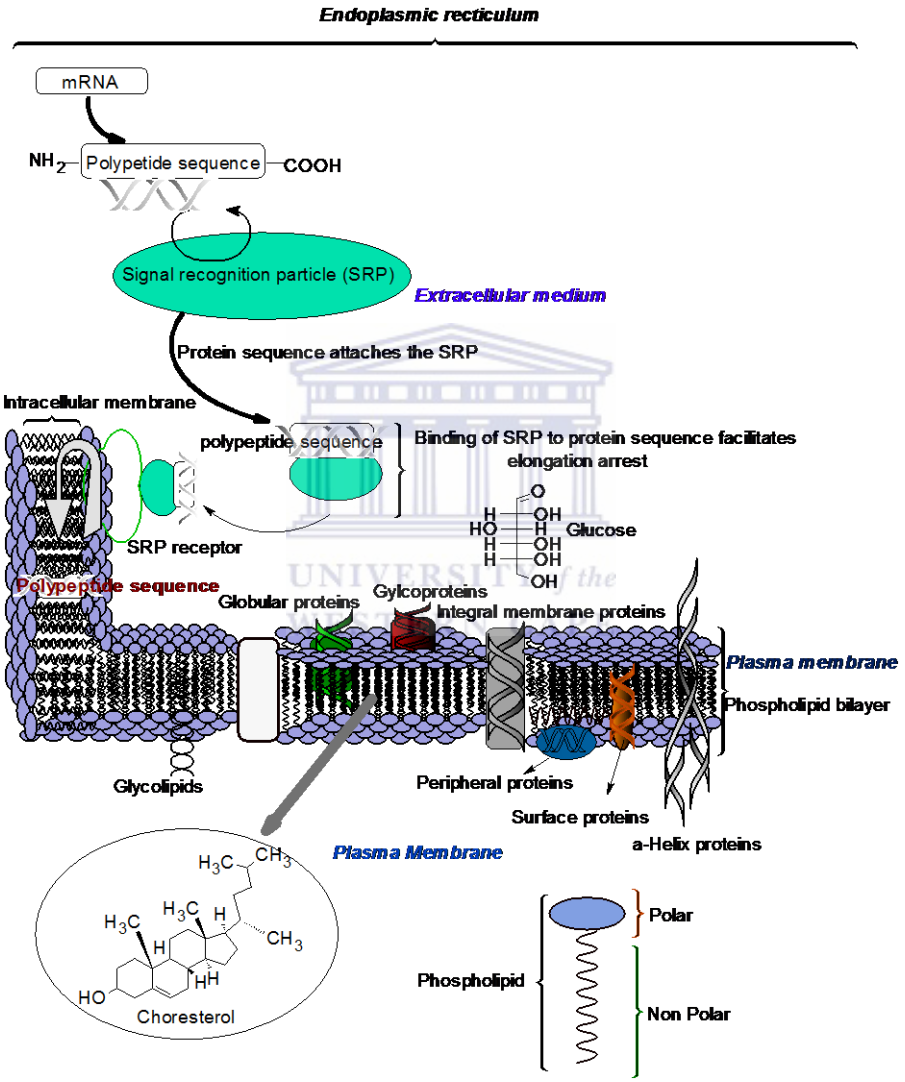

Figure 19: Protein biomolecules secreted in the intracellular, extracellular and plasma membranes. (Cooper 2000, Lodish, Berk et al. 2000, Shao and Hegde 2011)

Once the protein sequence is translated from mRNA with a complete peptide sequence, the full-length polypeptide can then intercept with mRNA sequence of the signal recognition protein (SRP) by affinity to inhibit further translation of the polypeptide chain sequence, this can be observed in

the signal transduction mechanism highlighted in Figure 19. The bound polypeptide/SRP complex is then translocated from the extracellular membrane to the intracellular surface of the plasma-endoplasmic reticulum membrane. Interaction of the polypeptide/SRP with the extracellular membrane's SRP receptor sequence induces the continuation of the translation processes on the polypeptide. Splitting of the complex receptors and the release of the peptide sequence from the SRP receptor chain is catalysed by the enzyme peptidase. Upon the peptidase catalysed dis-integration reaction, the SRP is then released and recycled back in the extracellular membrane. The synthesized protein sequence is then translocated within the membrane. Further translation and regulation processes involving these proteins occur on the membrane integrated polypeptide sequence. The regulation processes of these polypeptides through the extracellular cytosol molecules and other peptides is via the hydrophilic sequence segments of the polypeptide chain and the regulation of the membrane micro-molecules and other types of proteins is via its active hydrophobic intra-membrane helix sequence segments, while the protein molecule remain intact on the plasma membrane surface. For soluble proteins, further polypeptide sequence elongation is terminated after the release of the polypeptide's primary structure. A complete primary structure in this case is released through the protein's membrane to the lumen, where the folding and conformation into a complete 3D structure and subsequent translocation begins.

1.5.2. Signal transduction in nuclear receptors.

Nuclear receptors are proteins found inside the cell whose function are sensing hormones: steroids and thyroid molecules. Suggested by their characteristic name, these receptors function inside the nucleus, but are expressed in the cell's cytoplasm, then transported to the nucleus (Gadaleta and Magnani 2014, Plošnik, Vračko et al. 2015). Nuclear receptors are unique, highly specific types of receptors that directly associate with specific genetic codes for gene expression and thus are responsible for controlling development and homeostasis within a genome, a property that sets them apart from other types of receptors. Effective expression and regulation of genes is induced by the nuclear receptor-protein's interactions with other proteins and biomolecules such as co-suppressors and co-activators. Double membrane structures of the nuclei are associated with flanking micro-nuclear range of specific sequence proteins and specific sequence integral receptors, responsible for regulating specific micro-molecules inside the cytosol. The protein sequences of the integral membrane proteins have specific peptide sequences to allow for protein-

protein interactions and their other functions at the nuclear membrane; allowing the polypeptides to directly interact with the nucleus. Size differentiating specific proteins, transport lower molecular weight proteins with less than 20000 Da to permit freely within the membrane, nucleus, and cytoplasm (Mishra 2010). A schematic model of a steroid binding to different receptors in the cell and nuclear membranes is outlined in Figure 20.

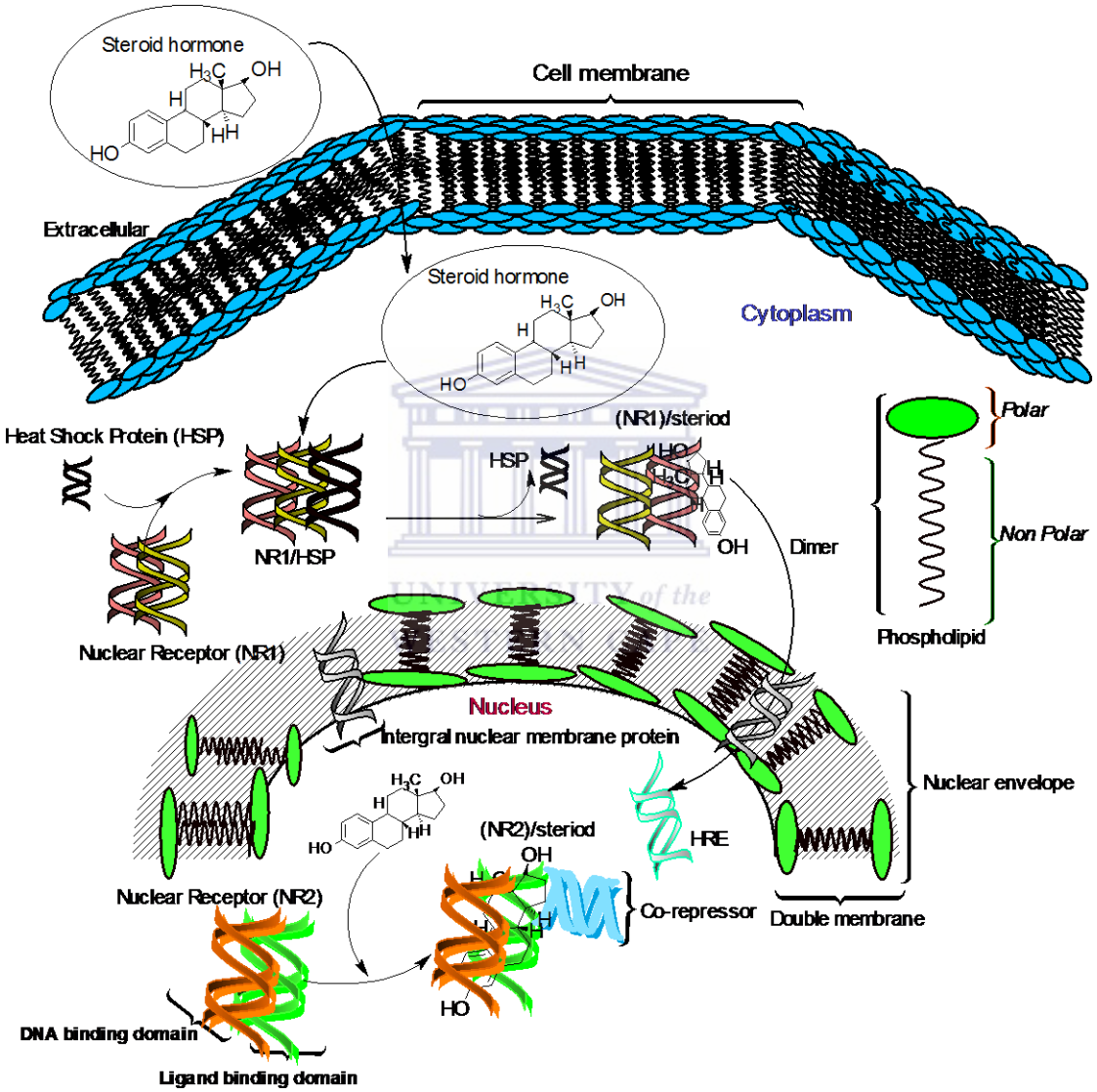

Figure 20: Binding of a steroid hormone to the nuclear receptors: type 1 and type 2. (Chunyou, Wentao et al. 2008).

Nuclear receptors are activated by ligands with great affinity for the receptors' active sites within the double membrane to initiate gene regulation and expression (Plošnik, Vračko et al. 2015,

Gustafsson 2016). Activation of these receptors is contingent to the presence of a binding ligand at the receptor's active site. Described in Figure 20, is the binding mechanism of an example of a steroid hormone, to the nuclear receptors: type 1 (NR1) and type 2 (NR2). The complex 3D structure of these receptors is associated with the presence of a DNA binding domain with a specific DNA sequence allowing them to directly interact with other encoded DNA molecules, thus regulating specific genetic codes of molecules, and referred to as; transcription factors (Klinge, Bodenner et al. 1997, Pawlak, Lefebvre et al. 2012). Signalling in nuclear receptors are induced by ligands, either resulting into up-regulation or down-regulation of gene expression. Classification of signal transduction in different homologous types of nuclear receptor is outlined in section 1.5.2.1 to section 1.5.2.3.

1.5.2.1. Signal transduction in type I nuclear receptors (NR1).

Nuclear receptors of this class are referred to as nuclear receptors of class 1 (NR1) expressed in the cytoplasm (Burris, Solt et al. 2013, Gadaleta and Magnani 2014). The binding mechanism of a NR1 was illustrated in the previous figure, Figure 20. Their mechanism related to gene expression, initiate from the DNA and ligand binding domains interacting with the heat shock proteins {i.e. HSP(s)} co-activators (i.e. activated by heat changes and internal stresses). A hormone that readily diffuses from the extracellular plasma to the cytosol then activates the intermediate NR1/HSP complex. The HSP then dissociates from the NR1-hormone complex and translocates for another association cycle. The NR1-hormone complex then is converted into a dimmer that is translocated from the cytoplasm to the intra-nuclear plasma. The hormone response element (HRE) found in the cell's nucleus binds only specific protein receptor sequence at the DNA binding domain of the nuclear receptor (i.e. NR1) in order to initiate any gene regulation or transcription processes. The HRE in the nucleus is a short nucleotide sequence transcribed with a specific DNA sequence that binds a specific dimmer: NR1/hormone complex. Other segments of the HRE are the inverted sequence of the first segment referred to as the inverted repeats (Righetti 2005, Mishra 2010). The HRE are highly selective and up-regulated by the NR1/hormone complexes. Nuclear receptors can bind to either one or both; the HRE sequences or the inverted repeat regions.

1.5.2.2. Signal transduction in type II nuclear receptors (NR2).

Type II nuclear receptors (NR2) remain located in the plasma of the nucleus at zero-concentration of the signalling ligands, a binding mechanism of an NR2 is illustrated in Figure 20. A hormone diffusing to the nucleus binds to a co-repressor motif of the NR2 resulting in the production of the NR2-hormone complex. The hormone bound or activated NR2 consecutively binds the hormone response element (HRE) resulting into formation of the HRE-NR2/hormone complex, prior to transcription and regulation processes. The complex is further activated by an RNA polymerase enzyme; that consecutively releases an effective repressor on the nuclear receptor. The HRE-NR2/hormone/RNA polymerase complex can further undergo transcription induced by the enzyme, RNA polymerase at the DNA encoded sequence of the RNA. The mRNA is then recovered and recycled back to the cytoplasm.

1.5.2.3. Signal transduction in G- protein coupled receptors {i.e. GPCR (s)}.

G-Protein coupled receptors (GPCR) are a diverse class of nuclear receptors exclusive to eukaryotic cells that constitute a large group of protein receptors that are trans-activated in the intra-cellular membranes by their ligands prior to the extracellular signal transduction (Ando, Hew et al. 2001, Kobilka 2007). GPCRs adopt their appellation from a G-protein molecule (i.e. guanine nucleotide binding protein) coupled to these receptors (Gutkind 1998, Croft, Hill et al. 2013). The G-proteins are reversibly trans-activated by the GPCRs' because of the synergetic effect that occur in both these proteins. Steady metabolic pathways and responsiveness of cells is through activation of the GPCRs by their associated: receptor molecules, signal transducing ligands, trans-activators, and co-suppressors to achieve homeostatic stability. GPCRs are defined by the name 7 trans-membrane receptors (7TM) or seven transmembrane domain receptors, accounted by adopting the hepta-crossing transverse conformations within the membranes and are induced and activated by a series of organic and inorganic molecules such as; odorant, photosensitive compounds, and neurotransmitters (Choe, Park et al. 2011, Kobilka 2013). GPCRs activating molecules may vary in mechanism of action, expression in cells, size, and chemical structures and constitute a diverse group of the receptor's activators expressed in species. GPCRs are classified by their effective ligand transduction mechanisms. A classification of GPCRs is schematized in Table 2.

Table 2: Classification of GPCR families.

CATEGORY OF GPCR	CLASSIFICATION
Rhodopsin like GPCRs	Family A
Secretin-receptor GPCRs	Family B
Metabotropic glutamate GPCRs	Family C
Fungal mating pheromone receptors	Family D
Cyclic Amp receptor	Family E
Frizzed/ smoothen receptors	Family F

The signal transduction in a GPCR initiates when a ligand diffuses to the ligand binding domain proximity of the GPCR. Once the ligand is bound at the ligand binding pocket (LBP) of the receptor, the receptor coupled; G-protein is activated through substrate level transactivation, at the C-terminus domain. A G-protein motif exists as three distinct heterotrimeric active helical protein molecule of G_{α}, G_{β} and G_{γ} subunits (Kobilka 2007, Tilley and Rockman 2011, Ghanemi 2015) and can be identified in the structure, outlined in the mechanism that is described in Figure 21.

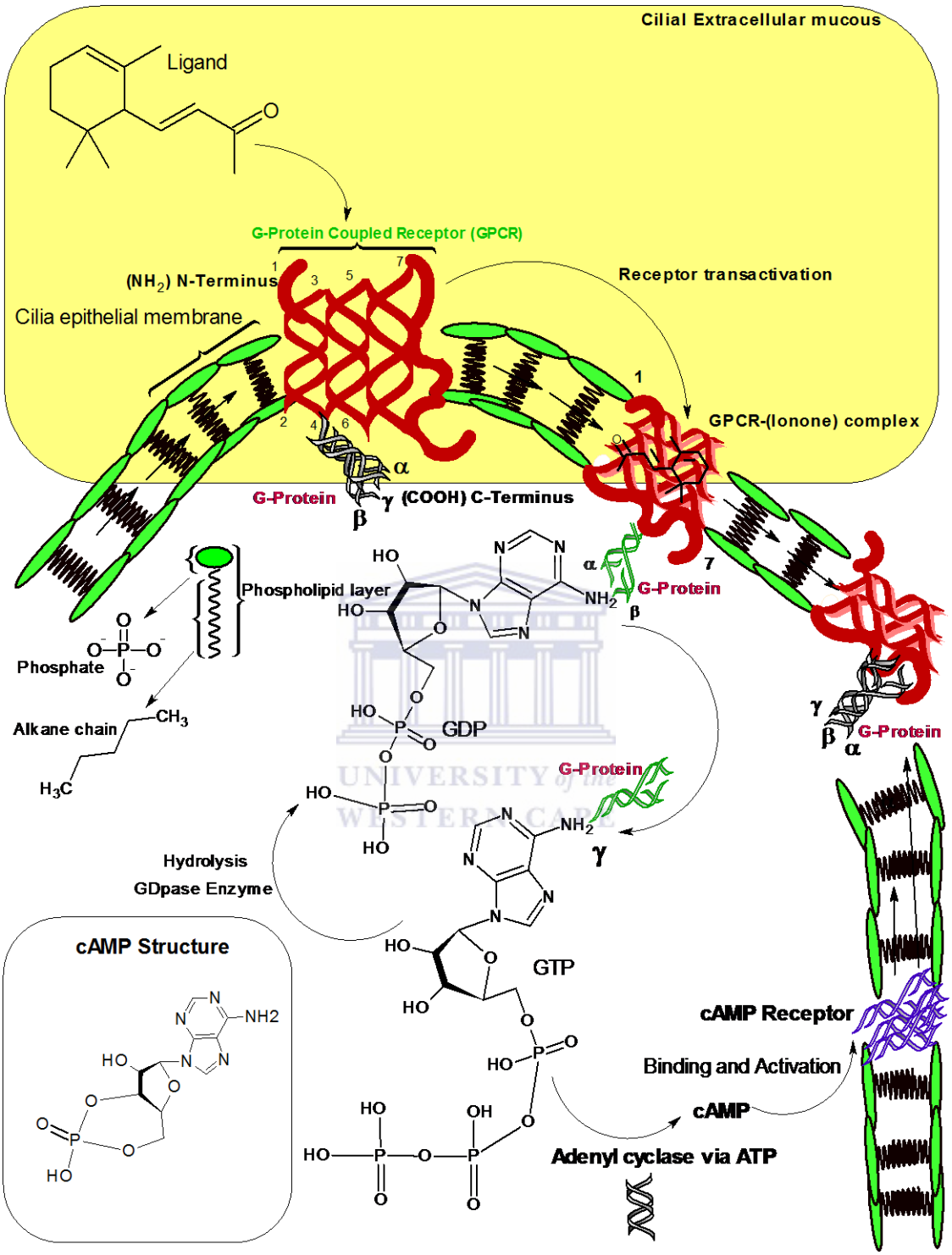

Figure 21: A synopsis of the binding mechanism of a ligand to the rhodopsin like family of GPCRs (Kobilka 2007, Burris, Solt et al. 2013, Gadaleta and Magnani 2014).

G-Protein stable homologies promptly exist coupled to a guanine diphosphate molecule (GDP) (Moller and Amons 1985, Ebrahimi and Chess 1998, Kobilka 2007). Once a ligand activates the GPCR at substrate level, the receptor coupled G-protein, alternatively undergoes a secondary activation at the GDP bound G-protein sequence helix, that triggers the inter-conversion of a GDP molecule to the guanine triphosphate (GTP) molecule, which then dissociates to the plasma. GPCR bound active G-protein-GTP complex initiates a secondary catalytic reaction cycle wherein, a plasma adenylecyclase (AC) enzyme molecule located in the cytoplasm is released with high energy co-factor; adenosine triphosphate (ATP). The ATP is then converted to cyclic adenosine monophosphate (cAMP) through a phosphate hydrolysis reaction. The cAMP can either bind to the cAMP membrane bound receptors, functioning as a modifying molecule that induces the potential of cAMP receptors to interact with; DNA(s), proteins or alternatively can be converted to adenosine monophosphate (AMP) via phosphor-diesterfarase enzyme (PDE). An AMP molecule secondarily undergoes deamination reaction catalyzed by the enzyme myoadenylatede-aminase (MADA) (i.e. also known as adenosine monophosphate deaminase) to inosinic acid (IMP). Figure 22; illustrates a reaction mechanism through AMP enzymatic conversion reaction by MADA.

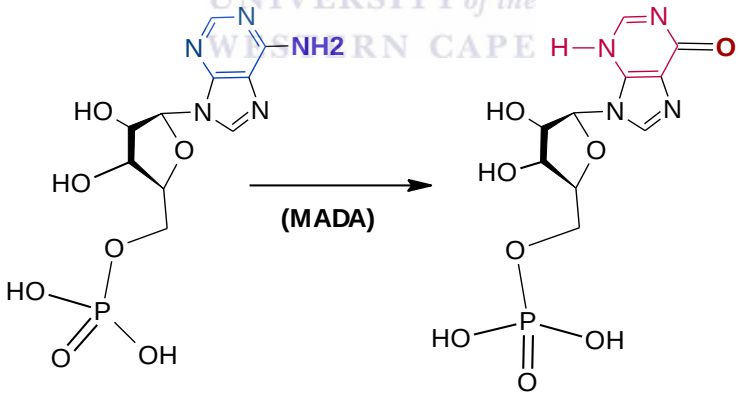

Figure 22: An enzymatic conversion of an AMP to an IMP molecule.

The enzymatic conversion of the AMP molecule involves the oxidation of the amino group (i.e. highlighted) of the adenine ring to a carbonyl group. This is then followed by delocalization of electrons over the purine ring to stabilise the molecule.

1.5.2.3.1. Signal transduction mechanism in olfactory GPCRs (i.e. family A-rhodopsin like GPCRs).

The rhodopsin like family of receptors have several sub-classes that extend their functionality from hormone reception to pancreatic and endocrine regulation (Ebrahimi and Chess 1998, Palczewski 2006, Kobilka 2007). Family A- rhodopsin like GPCRs consists of compromised classes: Class A1 to A19, categorized by their genetic occurrence. Substrates or ligands such; as light emitting ligands, neurotransmitters, lipids can activate rhodopsin like GPCRs (Angelika Krebs, Patricia C. Edwards et al. 2003). Odorants and pheromones are detected by rhodopsin like GPCRs that are expressed in the olfactory receptor neurons, referred to as olfactory receptors (Angelika Krebs, Patricia C. Edwards et al. 2003). Olfactory and vomeronasal receptors are induced by external chemical stimulants, activating the olfactory receptors inside nasal plasma membrane to transmit a nerve impulse to the dendrites of the olfactory nervous system at the glomeruli of the olfactory bulb, located in close proximity to the organelle's: recognition, association and quantification sites in the hypothalamus. A signal transduction mechanism of the olfactory receptors is described in Figure 23.

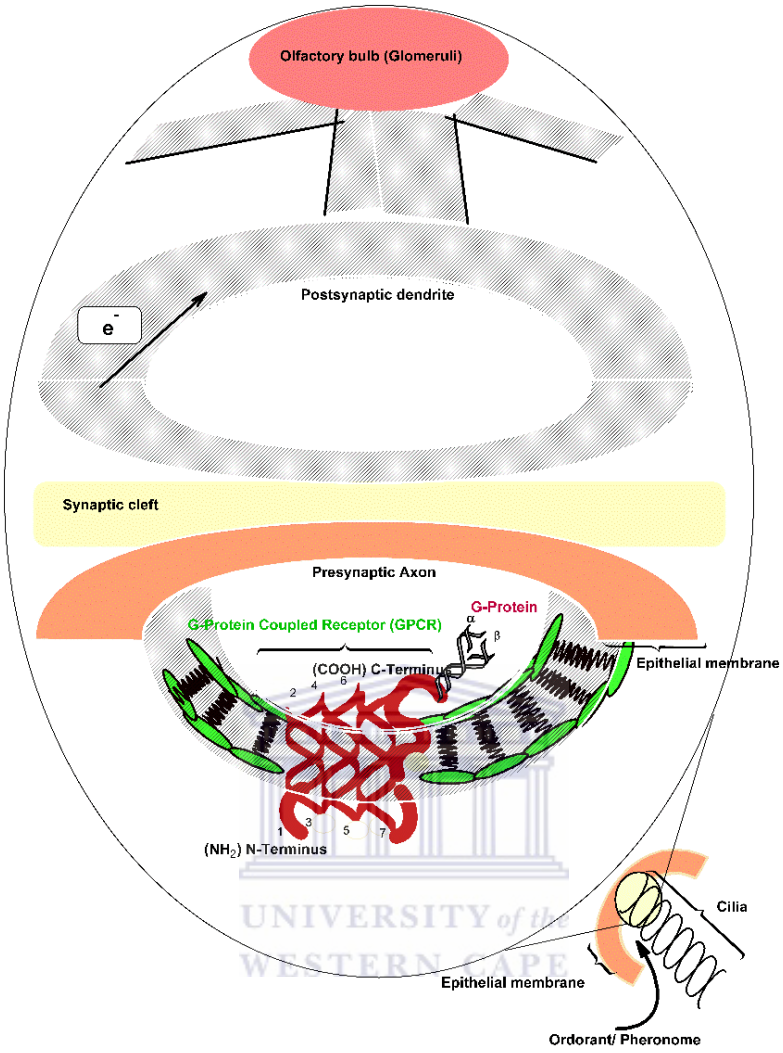

Figure 23: Signal transduction in the olfactory rhodopsin like family GPCRs. (Ebrahimi and Chess 1998).

The olfactory sensory nerves communicate with the central nervous system via electrochemical synapses generated by the interaction of the chemical stimuli with the synaptic receptors and proteins, encoding for chemoreception processes. In Figure 23, the signal transduction of an exogenous odorant by the olfactory receptor is through binding of an exogenous odorant to the GPCRs expressed in the cilia plasma membrane, also designated as olfactory epithelial membrane. Binding of a ligand to the olfactory GPCRs trigger the signal transduction in the olfactory nerve receptors { i.e. ONR(s)} where a synapse in the form of an impulse is transmitted to the terminus of presynaptic neuron, followed by a chemical induced synaptic transmission of an impulse to the prolonged terminus of the post-dendritic neuron, at the synaptic cleft. Signal transduction and

neurotransmission is terminated at the bisected glomeruli in association with an olfactory bulb. Olfaction can trigger two processes excitability and inhibition depending on the types of ONRs' signal transducing compounds or activating molecules. Classes of compounds that are transmitted in ONR are mostly non-volatile compounds, but a number of volatile compounds require pre-adsorption within the membrane's lymphatic system; the mucus, before a signal transmission can occur. Olfactory nerves are induced by exogenous chemical stimuli within micro to millisecond seconds. The split-second chemoreception process is however, highly reversible, with chemoreception incurring in milliseconds depending on dynamic desorption of the volatile chemical from ONRs. The chemoreception is known to be genetic code selective thus, ecological genome variance coding on the ONRs have unique binding mechanisms. Humans have more than 350 ONRs presumably sensing distinctively inestimable classified categories of volatile chemical compounds. Species such; as mice have more than 1500 expressed ONR in the olfactory nervous system, responsible for sensing innumerable odorant and pheromones. These relative species are intrinsic in neurology and pharmacology for assessment of drug interaction studies both *in vivo* and *in vitro*. Signal transduction in these receptors however, initiates with an exogenous chemical binding at the GPCR's ligand binding site. A paragon GPCR signal transduction involving the activation of an olfactory GPCR, with a volatile exogenous ionone molecule is described in Figure 24. Ionone; an odorant molecule, associated with a rosy scent, derived from β-carotene steroid; associated with a β-carotene backbone; R-isoprene group ketonized butanone moiety {i.e. -C=C-C(CH_3)=O} that is attached at the 2-α carbon position of the 1,3,3-trimethyl-cyclohexene (Lalko, Lapczynski et al. 2007). Ionone synthesis is described through two distinctive mechanisms; an enzyme catalyzed biosynthesis route and an organic acid catalytic synthetic route from the nucleophilic reaction of the citral compound with the deprotonated basic acetone (Allen 1964). The enzyme catalyzed synthesis route of α-ionone is metabolized by the oxidative oxygenase enzyme carotenoid dioxygenase. In the presence of the molecular oxygen radical, a β-carotene is catalytically transformed through the dioxygen transfer region-symmetric oxidation of a pi-diene bond between; carbon-15 and carbon-16 bond of the β-carotene, linear isoprene ring to a dioxyl-β-carotene reactive radical. A stable isomer of 10'-apo-10'-carotenal and α-ionone is obtained upon carbonylation of the oxyo-carbonyl radical stabilization reaction of the hemolytic cleavage products. The enzyme catalysed synthesis route to α-ionone is outlined in Figure 24.

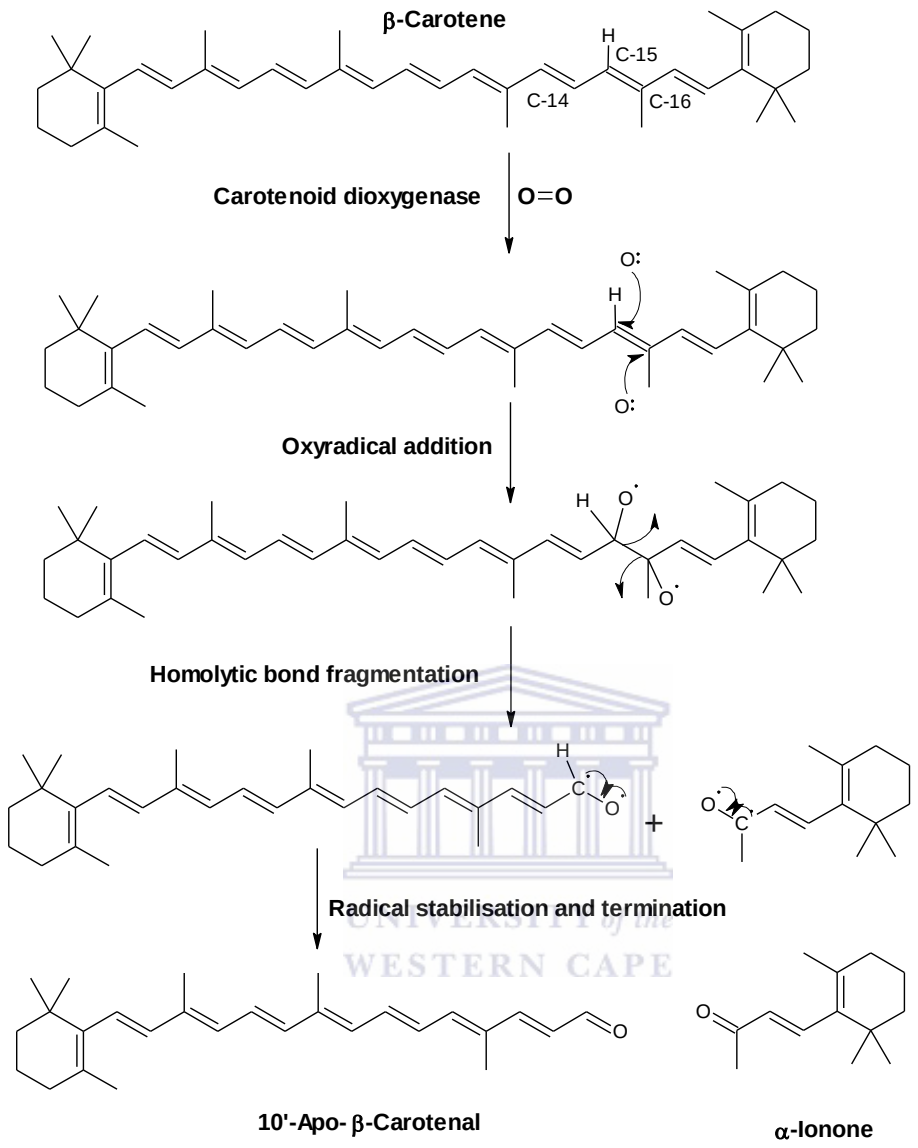

Figure 24: An enzymatic synthesis route to α-ionone from β-carotene.(Allen 1964)

Organic synthesis route of the α-ionone originates from a nucleophilic reaction of the citral molecule (i.e. 3,7 dimethyl-2, 6-octadiene-al), an organic compound expressed in essential oils of citrus fruit plants such as; lemon grass, lemon tea tree, orange, lemon, petit grain. Citral is a type of an aroma organic compound associated with a lemon citric scent, a structure of citral is corroborated in Figure 25**.** The acid catalysis reaction between citral and acetone is dependent on the calcium oxide acting as a heterogeneous catalyst that catabolises the dehydration reaction, before the olefin cyclization reaction of the 6,9,9-trimethyl-3,5,9–deca-trienone can occur. An organic synthesis route to an ionone compound is illustrated in Figure 25.

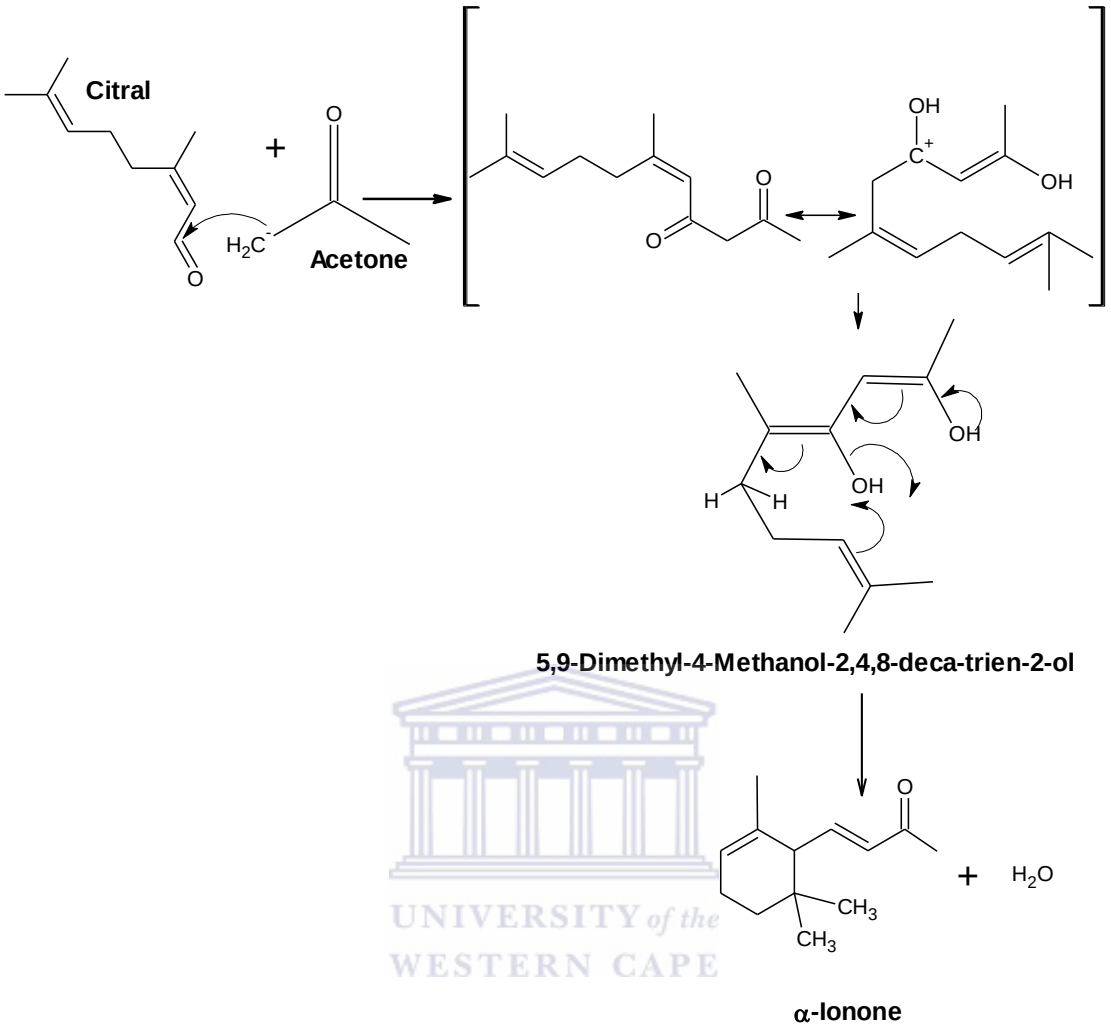

Figure 25: An organic synthesis route to α-ionone from beta-carotene.

(Aumo, Oksanen et al. 2005).

The cyclization of the intermediate product; 6,9,9-trimethyl-3,5,9–deca-trienone is then followed by the aldol condensation reaction that is terminated through the production of the final synthesis product; α-ionone. Other volatile signalling molecules detected via the olfactory G-protein coupled receptors are summarised through Figure 26 and Figure 27.

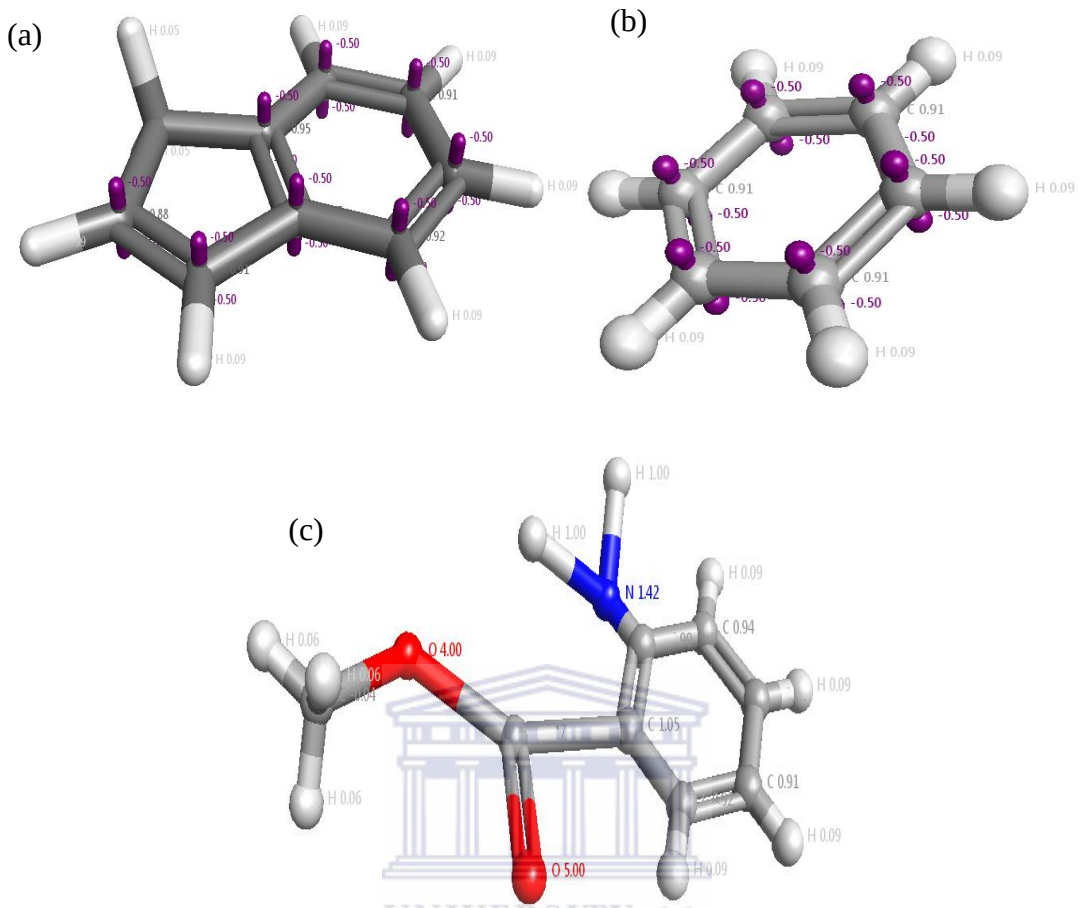

Figure 26: Organic odorants: (a) indene (b) benzene and (c) methyl anthranilate compounds

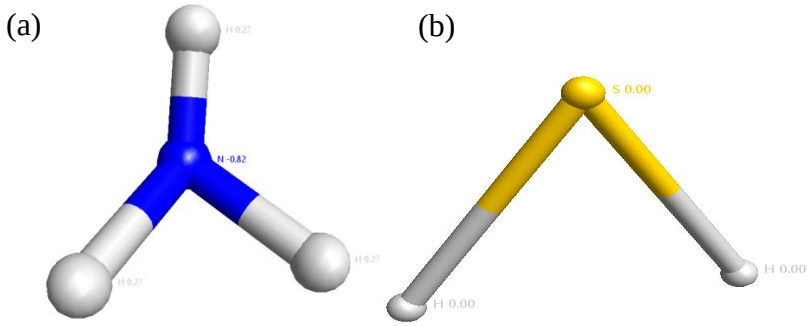

Figure 27: Inorganic volatile odorants: (a) hydrogen sulphide, and (b) the ammonia compounds.

The molecules presented in these figures were created using Torch™ molecular design software.

1.5.2.3.2. Signal transduction in secretin-receptor family of GPCRs (i.e. family B), metabotropic glutamate receptors (i.e. family C) and frizzed/smoothen receptors (i.e. family F).

Signal transduction in family B, family C and family F, GPCRs occurs via the ligand induced activation of the GPCRs in the mechanism that is defined in the previous section; section 1.5.2.3, initiating with binding of the receptor activating ligand to the GPCR resulting in dimerization of a coupled trimeric G-protein, that is then activated through the secondary signalling pathways. The mechanism of signal transduction in GPCR families: family B, family C, and family F is completely distinct from the signal transduction observed in GPCR families; family A and family E wherein, a volatile ligand prior to binding to the receptor is transferred to a plasma phase in the extracellular ligand binding site, prior the signal recognition process. Signal transduction in the extracellular GPCRs' families; family B, family C, and family F however, directly interacts with the ligands in the plasma due to the favourable chemical properties of the membranes such as: the chemical phase compatibility and the chemical potential (i.e. hydrophilicity and chemical polarity). The plasma membrane lipid bilayer possesses hydrophilic phosphate functional group heads and hydrophobic unreactive alkane chains sandwiched within the phosphate heads, which can be identified in the structure presented in Figure 28. The GPCRs that are integrated on the plasma membrane have a part of their protein sequence adopting slight hydrophobicity. In contrast, the GPCRs expressed in the plasma are usually soluble and thus possess hydrophilicity.

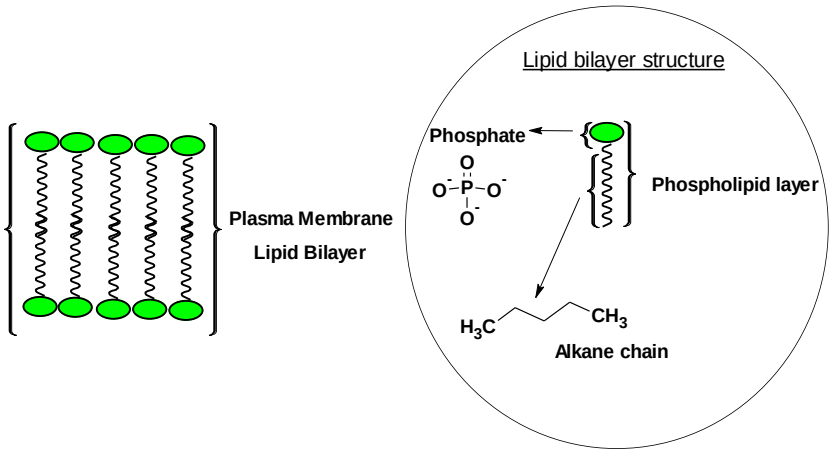

Figure 28: A plasma membrane lipid bilayer. (Cooper 2000, Alberts, Johnson et al. 2002)

In the structure presented in Figure 28, it can be noted that the chemical properties of the ligand are vastly related to ligand reactivity towards the different types of receptors; in the plasma membrane or the cytoplasm. This implies that, a ligand may be liable to induce signal transduction; either on the integral membrane receptors, peripheral receptors and/or plasma receptors, depending on its chemical reactivity and chemical compatibility. Consequentially, signal transduction at substrate level, induced by different ligands is highly dependent on the chemical polarity and chemical functional groups associated with the binding ligand.

Chapter 2 Assessment of the estrogen receptor-alpha (ER-α); chemical and photochemical properties

Estrogen receptors (ER) are types of GPCR; nuclear receptors located inside the cell's endoplasm reticulum known to be activated by the steroid hormone molecules (Heldring, Pike et al. 2007). Three classes of estrogen receptors are known at present: the estrogen receptor alpha (ER-α), the estrogen receptor beta (ER-β), and the estrogen receptor gamma (ER-γ) (Dechering, Boersma et al. 2000, Pearce and Jordan 2004). The estrogen receptors are classified in the family of nuclear receptors activated by steroids; thyroid hormones, and other molecules (Mueller-Fahrnow and Egner 1999, Nuedling, Kahlert et al. 1999, Sundarrajan, Liao et al. 1999, Levin 2001, Pare, Krust et al. 2002, Cherkouk, Rebohle et al. 2011). The ER-α have similar folding with its homologue ER-β, consequently it possesses identical structural features validated by the protein folding sequence identity, reported to be greater than 50 % (Gustafsson 1999, Mueller-Fahrnow and Egner 1999, Karas, Schulten et al. 2001). Receptors are complex protein structures, similar to proteins, they adopt three dimensional conformational structures, accounted by the bond structural properties, such as: the bond length, bond derivation that are associated with their quaternary protein structural folding and coiling (Wu and Wang 2001). Quaternary protein structures adopt a conformation relative to the diverse number of functional groups present in their primary amino acid sequences.

2.1. Structural properties of the estrogen receptor alpha (ER-α).

Estrogen receptor alpha (ER-α) is a type of nuclear receptor, present in diverse mammalian cell tissues; in the cardiomyocytes, ovarian cell tissues, and mammary gland tissues etc. (Zhu, Bian et al. 2002, Asaka, Toshio et al. 2007, Ba, Lu et al. 2007). These receptors have been found to be expressed in *Homo Sapiens*. ER-α is associated with; five inter-dependent domains present within its three dimensional protein complex structure. It is known to be activated inclusively by the extracellular compound; 17β-estradiol (E2) through substrate level activation of the ER-α's, E2 binding site that triggers the translocation of the receptor through the plasma membrane, which secondarily interacts with the co-activators through other sequence encoded binding motifs. This

induces gene expression, gene regulation, further post-transcription processes, and other receptor's directed functions (Yoon, et al. 201, Villablanca, et al. 2004, Tobias, et al. 2007, Sundarrajan, et al 1999, Stokes, et al, 2004, Pare, 2002). The quaternary estrogen receptor alpha structure is nevertheless associated with; twelve distinct helixes that are folded into a unique α-helical conformation with the inter-dependent amino acid sequence subunits (Gustafsson 1999, Mueller-Fahrnow and Egner 1999). The most conserved residues of the ligand binding domain of the ER-α have been identified to be in proximity to the co-activator and the ligand binding sites. Relative to the scope of this work, the coil-coiled structure of the ER-α is defined and outlined in Figure 29. The 3D coiled model was extracted from a SWISS MODEL protein data bank and is studied**.**

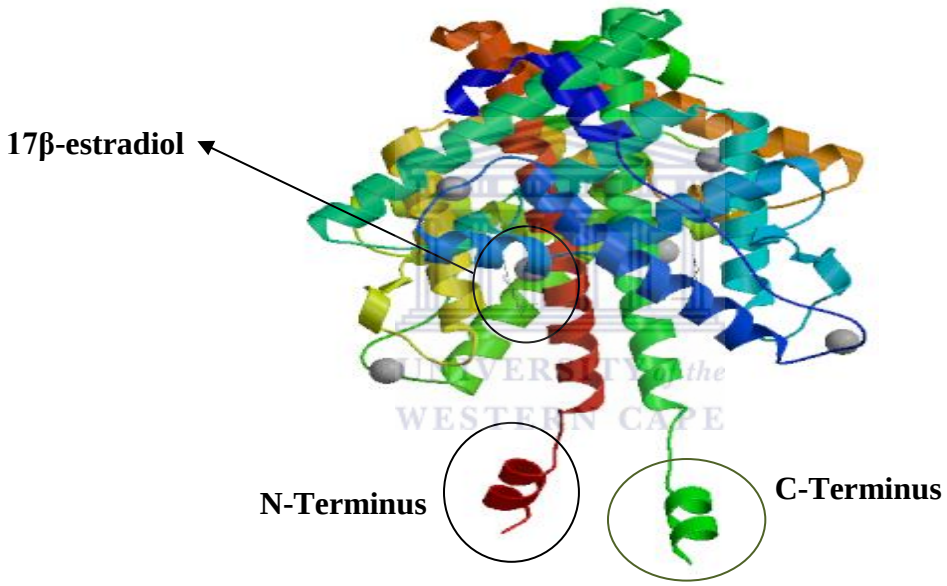

Figure 29: A quaternary coiled-coil structure of the ER-α bound to the 17β-estradiol with exposed N-terminus and C-terminus.(Tanenbaum, Wang et al. 1998)

An amine terminus (i.e. N-terminus) of the ER-α is associated with a free amine residue, a critical site on the receptor for its protein-protein association, post translation modification, and post transcription functions. The DNA binding domain of the receptor interacts with other DNA analogues (Walter, Green et al. 1985, Garidou, Laffont et al. 2004). The carboxyl terminus (i.e. C-domain, labelled C-terminus) is the receptor's domain that interacts with its analogue modulator ligands and co-activators. The ligand binding domain of the ER-α is associated with ligand recognition and has an amino acid sequence that specifically interacts with the hormone; 17β-estradiol with high binding affinity through the specific amino acids; arginine (Arg), histidine (His)

and glutamic acid (Glu), at the ligand binding site on the receptor. A 3D helical structure of the ER-α bound to the 17β-estradiol molecule is herein, described through Figure 30.

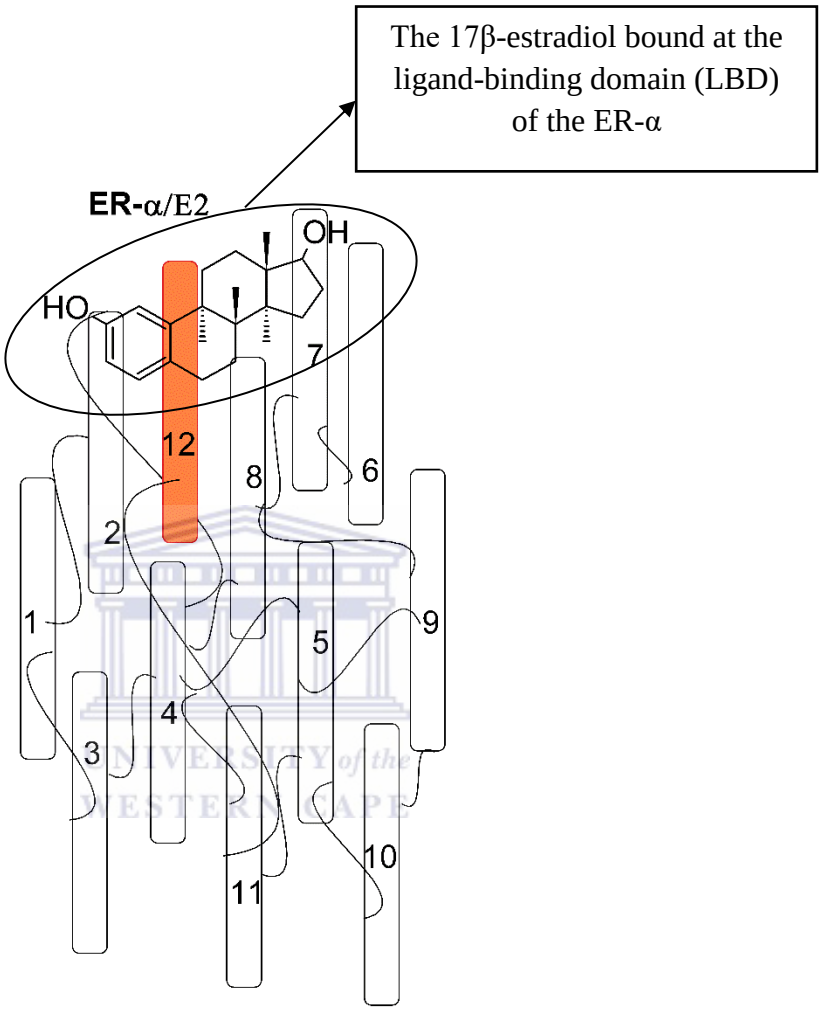

Figure 30: The helical structure of the ER-α bound to the 17β-estradiol. (Heldring, Pike et al. 2007)

The estrogen receptor-alpha models presented through Figure 29 and Figure 30 are both bound to the ligand; 17β-estradiol at the receptors' ligand-binding pocket. Activation of the ER-α by the agonist ligand; 17β-estradiol is through hydrogen bonding that occurs between then the hydroxyl functional groups of the 17β-estradiol molecule (i.e. present at the carbon positions; number 3 and nember 17 respectively) with the amino acids: Arginine-394, Histidine-524 and Glutamine-353 (i.e Arg_{394}, His_{524}- and Glu_{353} respectively) on the ER-α's ligand binding domain (LBD) (Mueller-

Fahrnow and Egner 1999). The binding mode of the 17β-estradiol at the ER-α's LBD is further described through the mechanism described in Figure 31.

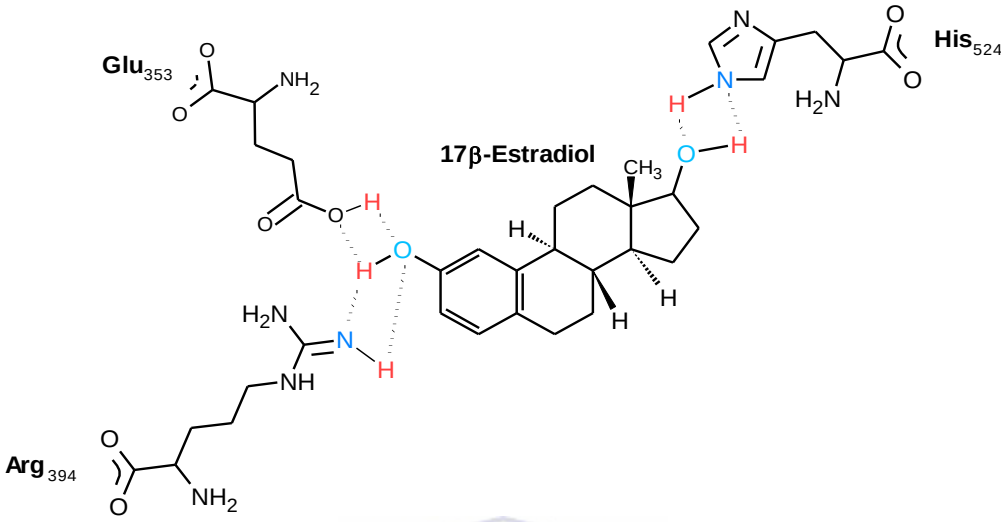

Figure 31: The 17β-estradiol compound locked at the ligand-binding site of the ER-α.

The hydrogen bond association at the 3-hydroxyl group of the 17β-estradiol is via a hydrogen atom of the secondary amine group of an Arg_{394} moiety resulting in the (ER-α)-(17β-estradiol) anchor at the ER-α's ligand binding site. The Glu_{353} residue utilizes its hydrogen to interact with the oxygen of the hydroxyl group of the 17β-estradiol, stabilizing the ligand molecule at the receptor's active site. Relatively the His_{524} amino acid residue in the ER-α utilizes its partial aromatic imidazole ring to polarize the 17-β hydroxyl group of the 17β-estradiol via the imidazole-amino-hydrogen. This results in the formation of a hydrogen bond between the oxygen molecule of the hydroxyl group and the nitrogen atom of the amine of the imidazole ring of the His_{524}, resulting in the polarized hydrogen atom at the 17β-hydroxyl group of the 17β-estradiol.

2.2. Classification of different domains of the estrogen receptor alpha and their amino acid sequences.

This section is designated to explicate the amino acid sequence of the ER-α. In a sequence presented in Table 3, the human recombinant protein ER-α was quantified and its structure was identified with reference to a sequence reported by authors; (Mueller-Fahrnow and Egner 1999, Pike, Brzozowski et al. 1999). The amino acid sequence of the ER-α is a 600-unit amino acids

length polypeptide chain, with a protein initiator codon methionine (Met) (i.e. 1st amino acid) and the terminator valine (Val) amino acid, present at the 600th position of the receptor amino acid sequence. The amino acid sequence of the *Homo sapiens;* ER-α is corroborated in Table 3.

Table 3: The human recombinant ER-α alpha amino acid sequence.

(http://www.abcam.com/recombinant-human-estrogen-receptor-alpha-protein-ab82606.html#description_images_1)

1-50	MTMTLHTKAS	GMALLHQIQG	NELEPLNRPQ	LKIPLERPLG	EVYLDSSKPA
51-100	VYNYPEGAAY	EFNAAAAANA	QVYGQTGLPY	GPGSEAAAFG	SNGLGGFPPL
101-150	NSVSPSPLML	LHPPPQLSPF	LQPHGQQVPY	YLENEPSGYT	VREAGPPAFY
151-200	RPNSDNRRQG	GRERLASTND	KGSMAMESAK	ETRYCAVCND	YASGYHYGVW
201-250	SCEGCKAFFK	RSIQGHNDYM	CPATNQCTID	KNRRKSCQAC	RLRKCYEVGM
251-300	MKGGIRKDRR	GGRMLKHKRQ	RDDGEGRGEV	GSAGDMRAAN	LWPSPLMIKR
301-350	SKKNSLALSL	TADQMVSALL	DAEPPILYSE	YDPTRPFSEA	SMMGLLTNLA
351-400	DRELVHMINW	AKRVPGFVDL	TLHDQVHLLE	CAWLEILMIG	LVWRSMEHPG
401-450	KLLFAPNLLL	DRNQGKCVEG	MVEIFDMLLA	TSSRFRMMNL	QGEEFVCLKS
451-500	IILLNSGVYT	FLSSTLKSLE	EKDHIHRVLD	KITDTLIHLM	AKAGLTLQQQ
501-550	HQRLAQLLLI	LSHIRHMSNK	GMEHLYSMKC	KNVVPLYDLL	LEMLDAHRLH
551-600	APTSRGGASV	EETDQSHLAT	AGSTSSHSLQ	KYYITGEAEG	FPATV

The N-terminus domain of the ER-α amino acid sequence initiates with an amino acid; methionine at position-1 to an amino acid lysine at position-180, consisting of a total of 180 amino acids. The N-terminus of the ER-α consists of the free amine R-side functional groups, derived from the methionine amino acids present at the beginning of the sequence (i.e. the MTMT sequence was abstracted from Table 3). The 65 amino acids unit length sequence from 185-250, beginning with CRVC (i.e. only four amino were recognised) was identified to be the DNA binding domain of the ER-α; responsible for DNA-DNA specific interactions and other estrogen receptor's protein transcription processes. A hinge region of the ER-α is identified by the amino acid sequence established from the amino acid 251 to 310, of 59 amino acid units (i.e. associated with the initiator

-four amino acids; MLGI) linked with the DNA binding via the M-M linkage. The N-terminus, the DNA binding domain, and hinge regions of the ER-α are highlighted through the proposed helical structures presented in Figure 32.

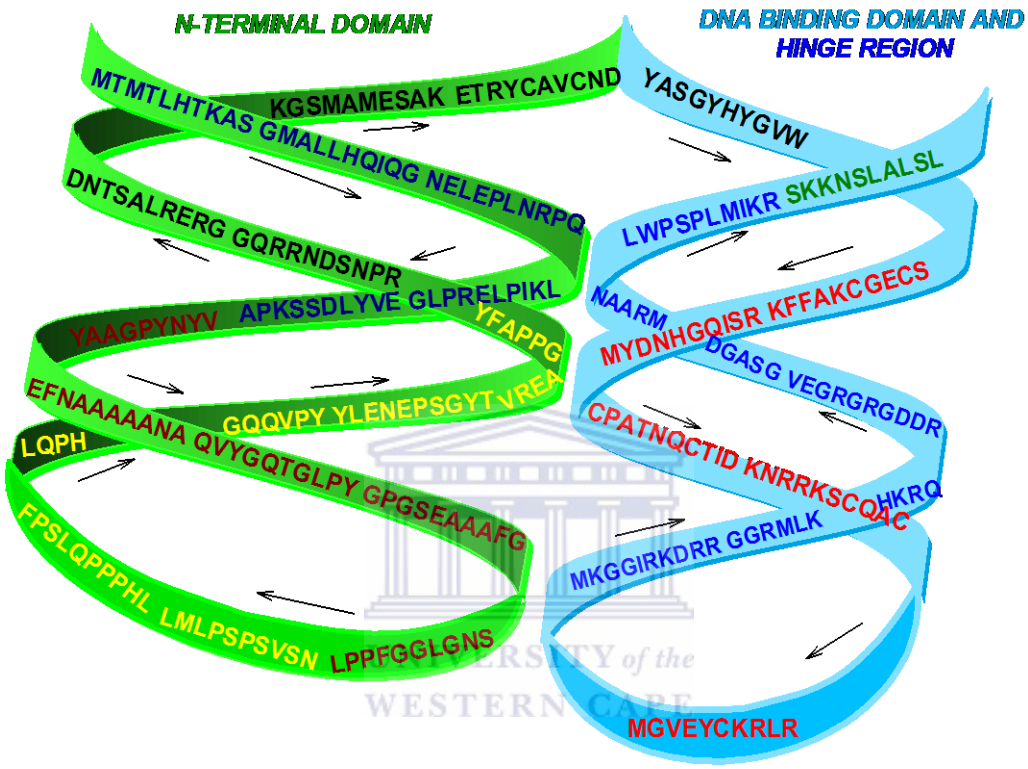

Figure 32: The cartoon coil-coiled amino acid sequence structure of the N-terminus, the DNA binding domain and the hinged region of the ER-α.

The primary codon of the ligand binding domain of the ER-α is associated with the amino acid sequence residue; TADQ and can be identified in the proposed cartoon coil-coiled protein structure presented in Figure 33. The length of the ligand-binding domain and the C-terminus domain of the identified ER-α are 240-unit and 48 amino acids unit lengths respectively and are presented in Figure 33.

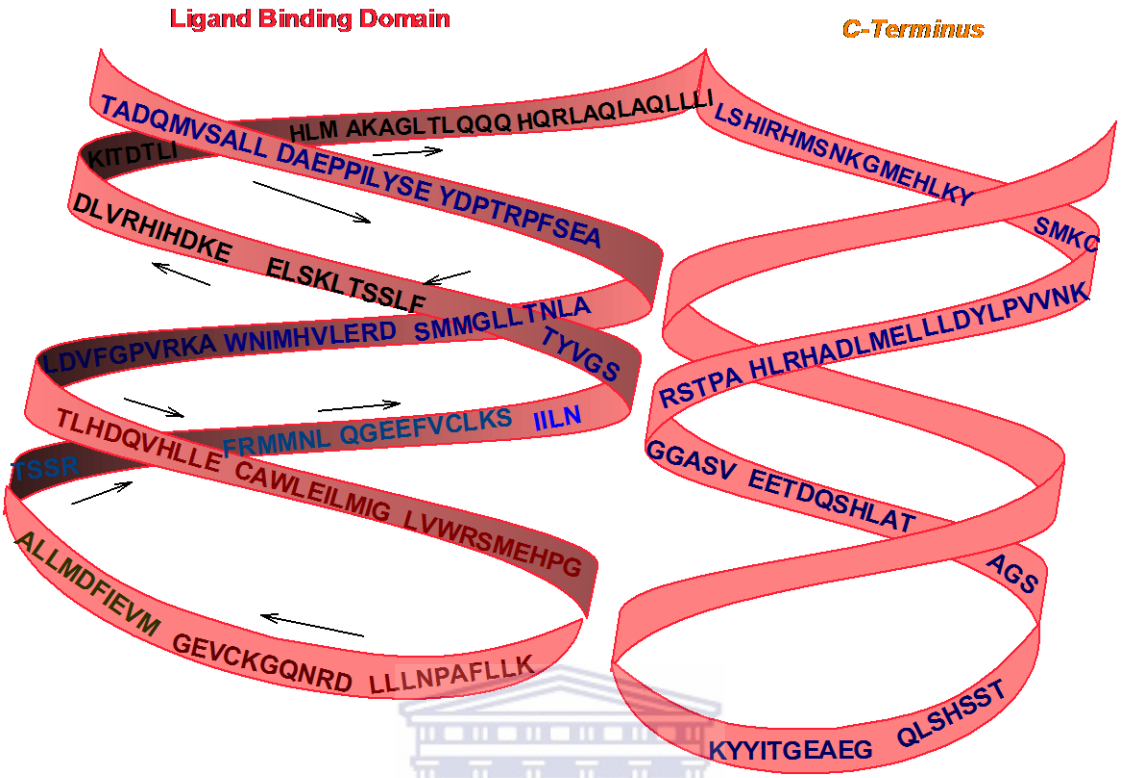

Figure 33: The proposed cartoon coil-coiled amino acid sequence of the ligand binding domain and N-terminus domain of ER-α.

The ligand binding domain and C-terminus domain of the ER-α are linked through the Alanine551-Proline552 amide linkage, identified in the amino acid sequence presented in Table 3. At the C-terminus domain of the ER-α, the initiator sequence was associated with amino acids; PTSR, terminating with the valine-600th amino acid associated with a free carboxylic R-functional group.

2.3. Optical and chemical properties of the estrogen receptor alpha (ER-α).

Ultra-violet visible (UV-Vis) and fluorescence spectroscopies were employed to examine the photo-electronic properties of the ER-α. Fourier transform infrared (FTIR) spectroscopy studies were executed to examine the chemical reactivity of the ER-α associated with its conserved functional groups present in the ER-α amino acid sequence.

Chemicals

A 95 % purified human recombinant estrogen receptor alpha (ER-α) biomolecule of 59 kDa molecular weight, used in these studies was purchased from *Abcam* through *Biocom Biotech* of South Africa. The ER-α was reported to be expressed in *E. Coli* and reported to consist of four distinct domains; the amine-terminus, the DNA binding domain, the ligand binding domain and the carboxyl-terminus. The following post-translation modifications on the ER-α were reported: phosphorylation, glycosylation, ubiquitination, demethylation at the Arginine-260, and palmitoylation. The purified recombinant human ER-α was preserved in a storage buffer solution of constituents: 20 % glycerol, 50 mM tris-acetate buffer of pH 7.4, 1 mM ethyl diamine tetra-acetic acid (EDTA), dissolved in 0.1 M phosphate buffer solution of pH = 7.4. The 0.1 M phosphate buffer solutions of pH 7.4 were prepared from sodium dihydrogen phosphate, disodium hydrogen phosphate in double distilled water, filtered by Ris Millipore ™ filtering system. The 1.7 µM stock solutions of the ER-α were prepared by 100 times dilutions of one µL of the ER-α with 0.1 M phosphate buffer solutions of pH 7.4.

Instrumentation

The Fourier transform infrared (FTIR) spectra were recorded on Perkin Elmer FT-IR spectrometer 100 (i.e. from California, USA) on NaCl pellets. The ultraviolet-visible (UV-Vis) absorption measurements of samples were done in quartz cuvettes on Nicolet Evolution 100 UV–Vis spectrophotometer (i.e. from Thermo Electron Corporation of Medison, USA). Fluorescence spectrometry measurements were done using Horiba JobinYvon fluorimeter (i.e. from Nano Log™ of Cedex, France).

2.3.1. Optical properties of the ER-α.

The absorption properties of the ER-α were primarily evaluated through UV-Vis spectroscopy studies. A 2 µM human recombinant ER-α stock solution was subjected to 10 times dilution. The 2 µL of the ER-α solution was then injected into a 1 mm path length; UV-Vis quartz cuvette and diluted to 1000 µL with 0.1 M phosphate buffer solution, with a pH of 7.4. For these studies the UV-Vis absorbance wavelength range between 200 nm to 800 nm was assessed. A spectrum of 0.2 nM ER-α is outlined in Figure 34.

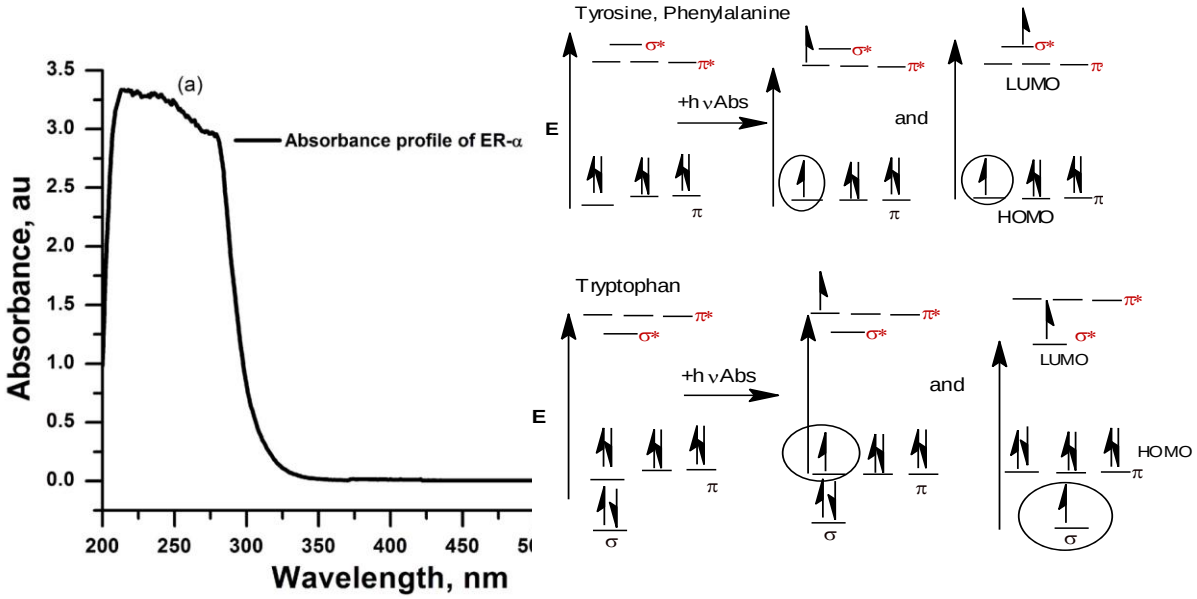

Figure 34: UV-Vis absorption spectrum of the ER-α in 0.1 M phosphate buffer solution of pH of 7.4.

A broad high energy absorbance maxima peak in the UV-Vis range between 200 nm and 375 nm with a maximum absorbance wavelength (λ_{max}) magnitude of 245.7 nm and an absorbance value of 3.227 au was observed. This absorbance was associated with the wavelength band edge (λ_{edge}) of 334.0 nm (i.e. E_g = 3.75 eV). The average absorbance maxima peak (AAMP) (i.e. at λ_{max} = 245.7 nm) estimated from the broad absorbance peak in the UV-Vis absorbance profile in Figure 34, was associated with the total absorbance area from the wavelength (λ) of 213.8 nm to the wavelength (λ) of 280.9 nm. The obtained broad absorbance UV-Vis profile was due to a spectral overlap of the absorbance of the photon energy by aromatic chromophores; phenylalanine (Phe), tryptophan (Trp), tyrosine (Tyn) (Schmid 2001, Walsh 2002), related to; $\sigma \rightarrow \pi^*$, $\pi \rightarrow \pi^*$, $n \rightarrow \pi^*$, $n \rightarrow \sigma^*$, $\sigma \rightarrow \sigma^*$ and $\pi \rightarrow \sigma^*$ electronic transitions. These absorbance maxima peaks distinctively occur at the UV-Vis absorption region between 200 nm to 300 nm. Nevertheless, the presence of histidine (His) amino acid residues in the amino acid sequence of the ER-α implied probability of the electronic transitions of the π-electrons of the R-functional group-imidazole rings. The electronic transitions associated with the imidazole ring of His are described through the chemical structures herein, presented in Figure 35.

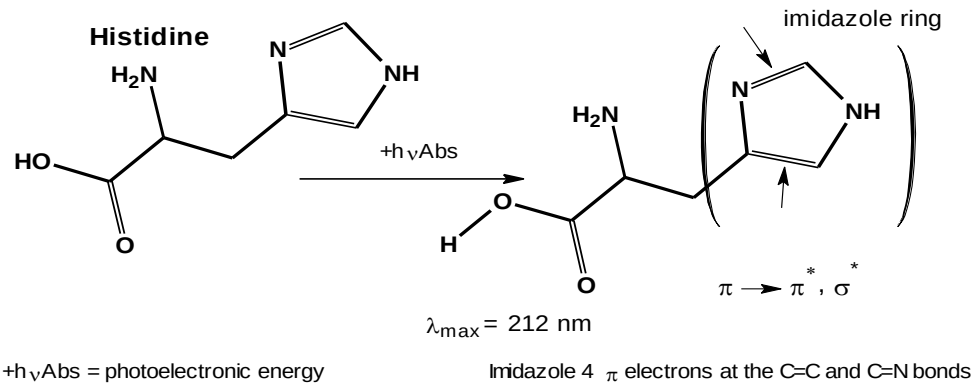

Figure 35: Electronic transition probabilities in a histidine (His) amino acid.

Imidazole rings of the His amino acid residues are highly reactive, adopting Zwitterion conformations at physiological pH conditions. Imidazole ring of the His amino acid is partially aromatic; with an extended 4π conjugated system, occupying the ground state energy level in a 4π electronic configuration, as indicated in a structure presented in Figure 35. Excitation of the electrons from the highest molecular orbital (HOMO) ground electronic state of the molecule results in the following transitions: $\pi \rightarrow \pi^*$ and $\pi \rightarrow \sigma^*$ at the C=C and C=N π-bonds. The His amino acid, UV-Vis absorption energies are reported to be observed at maxima wavelength; λ_{max} of 212 nm (Saidel, Goldfarb et al. 1952). Furthermore, the $\pi \rightarrow \pi^*$ electronic transitions are commonly observed at the absorbance wavelength range between 220 nm to 300 nm and slightly at higher wavelength regions for the longer extended conjugated systems. Relatively, the distinct resonance chemical structures of the: Tyr, Trp, and Phe aromatic-amino acids are further described through Figure 36, relative to the electronic transitions (i.e. that were studied in Figure 34) related to their conjugated pi-electron configurations of their R-functional groups.

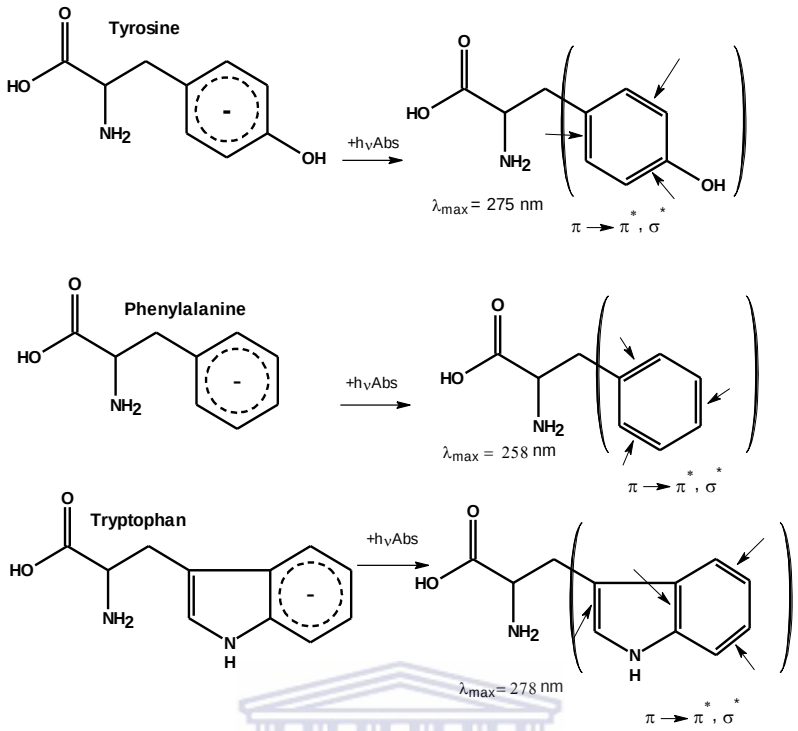

Figure 36: The UV-Vis active, π-electronic systems of: tyrosine (Tyr), phenylalanine (Phe) and tryptophan (Trp) amino acids, present in the amino acid sequence of the ER-α.

The amino acid residues of; Tyr, Phe are associated with the conjugated phenyl rings, with 6π electrons, while the Trp is associated with an indole ring, with an 8π-electron configuration. The absorption of photon energy at the π-electrons of the described chromophores; from the ground state {i.e. highest occupied molecular orbital (HOMO)} to the excited electronic state {i.e. lowest unoccupied molecular orbital (LUMO)}, results into the photo-electronic transitions; π→π*, π→σ* and n →π* on the R-linked aromatic functional groups. These electronic transitions were previously described in the Figure 34. The percentage occurrence of Phe, Tyr, Trp, and His amino acids in the ER-α were evaluated through the pre-described amino acid sequence of the receptor reported in Table 3 of section 2.2.

Percentage Occurrence of phenylalanine (Phe) in the ER-α $\approx \frac{15}{600} \approx 2.5\ \%$

Percentage Occurrence of tyrosine (Tyr) in the ER-α $\approx \frac{5}{600} \approx 3.8\ \%$

Percentage Occurrence of tryptophan (Trp) in the ER-α $\approx \frac{5}{600} \approx 0.83\ \%$

% Occurrence of histidine His in the ER-α $\approx \frac{22}{600} \approx 3.67$ %

The total photons absorbed were evaluated through the expression highlighted in Equation 2 using the intergraded area of the absorbance energy profile presented in Figure 34.

$$\int_{218.9}^{280.9} \boldsymbol{f(Abs)} = \int_{218.9}^{280.9} \frac{\boldsymbol{hc}}{\boldsymbol{\lambda_{max}}} = (\boldsymbol{ln\,\lambda_{max2} - ln\,\lambda_{max1}})$$

Equation 2

In the herein equation, Equation 2, *h* is 4.136 x 10^{-15} eV. s and represents the Planks constant, *c* has a magnitude of 2.999 x 10^{-8} m.s^{-1}, it presents the speed of light passing through the chromophore, and λ_{max} is the maxima absorbance wavelength in nm. The integrated total area of absorbance of the ER-α is presented in the next figure; Figure 37.

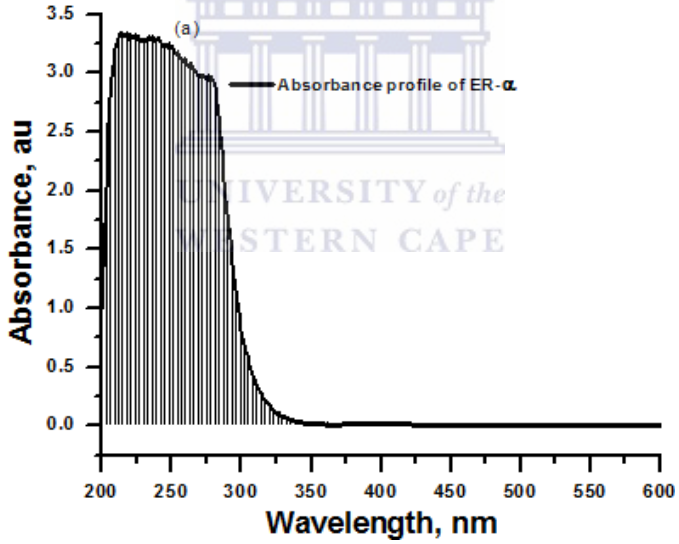

Figure 37: The total integrated area of the ER-α's absorbance characteristic.

The total number of photons absorbed were determined to be 296.26 au. The ER-α biomolecules are also distinguished by their UV-Vis active; amide or peptide bonds {i.e. R-C=N(C=O)} and disulphide bridges {i.e. the covalent disulphide bridges (i.e. S-S)}. The S-S bridges in the protein biomolecules are associated with the n→ σ* electronic transitions associated with sulfhydryl group lone pair of electrons, commonly observed at the average maxima wavelengths (λ_{max}) of approximately 250 nm (Teresa, Petersen et al. 2002). The S-S bridges-related electronic transitions

of the studied ER-α were also suggested be an outcome of the broad cross-transitional overlap maxima peak at λ_{max} of 245.7 nm, observed in the UV-Vis spectra of the ER-α presented in Figure 34. The distinct $\pi \rightarrow \pi^*$ electronic transitions associated with different amino acid R-function groups in the UV-Vis spectrometry studies of the ER-α were nevertheless complicated by the conjugated chromophores absorbing at congruent UV-Vis wavelength region.

2.3.2. The optical-fluorescence properties of the ER-α.

The optical properties of the ER-α were further examined through the fluorescence spectroscopy studies. The fluorescence spectra were recorded at two regions from a wavelength region between 495 nm to 600 nm and a low energy wavelength region between 650 nm to 750 nm. An excitation wavelength of 375 nm was propagated in a 1 mm quarts cuvettes containing 0.2 nM ER-α suspended in a 0.1 M phosphate buffer solution with a pH of 7.4. The ER-α optical properties were evaluated through parallel studies of the ER-α's absorption properties and fluorescence properties, the spectra are presented in Figure 38 (**A)** and Figure 38 (**B)** at various wavelength regions respectively.

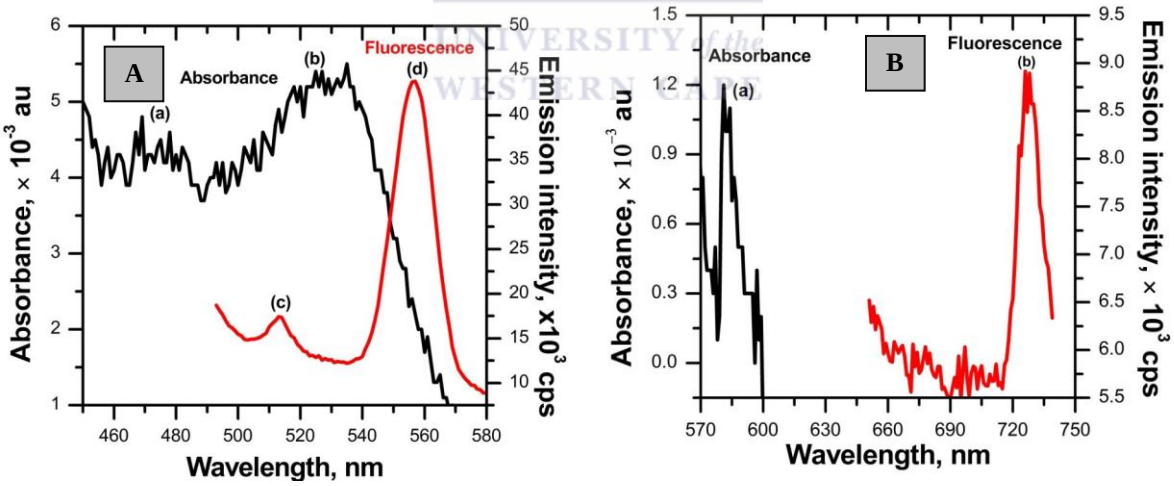

Figure 38: (A) The UV-Vis and fluorescence spectra of the ER-α at the visible region, **(B)** the visible to near infrared (NIR) region.

In the fluorescence spectrum of the ER-α presented in Figure 38 (**A),** two maxima emission peaks (λ_{em}) were evaluated at λ_{em} of 513 nm{(i.e. (c)} and λ_{em} of 557 nm {i.e. (b)} of Figure 38 (**A)** respectively). Protein molecules are associated with high fluorescence efficiency, these are

ascertained to be as a result of the fluorescence active conjugated π-electron systems, associated with the $\pi^* \rightarrow \pi$ electronic transitions of the different amino acid residues. The related characteristic electronic UV-Vis absorbance transitions were described in the UV-Vis spectroscopy studies of the ER-α described in the previous section of this chapter; in section 2.3.2. However, it was observed that in the fluorescence spectroscopy studies of the ER-α, these described electronic transition were distinguishable and occurred at distinct fluorescence emission ranges. The fluorescence active: tyrosine (Try), tryptophan (Trp), phenylalanine (Phe), histidine (His) and aspartic acid (Asp), emit at the emission maximas {i.e. $\lambda_{em\text{-}max}$ (s)} of; 303 nm, 348 nm, 282 nm, 360 nm and 475 nm, respectively (Teale and Weber 1957, Iwunze 2007, Kong, Yao et al. 2011). The electronic transition peak that was observed at the near infrared (NIR) emission region of the spectra in presented in Figure 38 (**B)** (i.e. at the $\lambda_{em\text{-}max}$ of 729 nm) was further associated with emission properties of other chromospheres present at the ER-α amino acid sequence. The fluorescence properties of the ER-α were further described through determining the quantum efficiency and the total number of photons emitted through integrating the given fluorescence emission spectrum of the ER-α herein, presented in Figure 39.

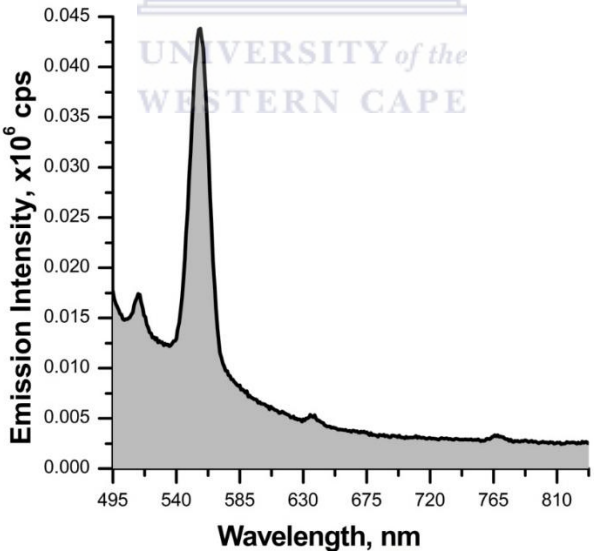

Figure 39: The integrated emission profile of the ER-α.

In the presented emission profile in Figure 39, the fluorescence emission area is proportional to the total number of photons emitted, correlated through the expression described by Equation 3.

$$Emision\ surface\ area = \int_{492.75}^{846.6} f(\lambda_{em-max})$$

Equation 3

In the equation, the initial and final wavelengths represent the fluorescence wavelengths between $\lambda_{=0}$ and $\lambda_{t=t}$ respectively, t represents the spectral acquisition time. The total amount of photons emitted was evaluated to be 17361652 au. The quantum efficiency (ϕ) of the ER-α (i.e. $\phi_{ER-\alpha}$) was evaluated using the absolute method given by next equation; Equation 4

$$\varphi_{ER-\alpha} = \frac{Em_{ER-\alpha}\, Abs_{Ref}}{Abs\ \ Em_{Ref}} \frac{n_{ER-\alpha}^2}{n_{Ref}^2} \Phi_{Ref}$$

Equation 4

In Equation 4, the parameters; $\varphi_{ER-\alpha}$ and φ_{Ref} are the quantum efficiencies of the estrogen receptor alpha (ER-α) and the reference materials respectively, *Abs* and *Em* notations are the absorbance and emissions integrated areas respectively. The n_{Ref} and $n_{ER-\alpha}$ are the refractive indexes of the reference material and the ER-α respectively. The quantum efficiency of the ER-α was determined to be 0.02, the tryptophan was used as the standard reference material its quantum yield is reported to be 0.13 in aqueous medium (Chen 1967).

2.3.3. The estrogen receptor alpha (ER-α) chemical properties.

The infrared spectroscopy (IR) studies give details about the mode of bond vibration and rotation adopted by the functional groups of: molecules, compounds, radicals, anions and cationic moieties. In addition, it can be a provident chemical analysis tool for identification of the bonding nature in molecules and compounds, in due of the present covalent linkages, that give rise to infrared vibration bands of; primary, secondary and tertiary bond structures as opposed to ionically bonded states. In consequence, it can potentially determine the distinct vibrational stretching frequencies and rotation modes of functional groups at different regions of the IR spectrum. The estrogen receptor alpha (ER-α) chemical bond properties were evaluated using Fourier transform infrared spectroscopy (FTIR) to examine the molecular level bonding modes of the various functional

groups present at the ER-α's polypeptide amino acid sequence. An FTIR stretching frequency window region between 1250 $cm^{-1}$and 4000 cm^{-1} was evaluated; to determine the functional groups present in the ER-α, analysed on NaCl beads. The spectrum of the liquescent 0.1 µL of 0.2 nM ER-α is presented in Figure 40.

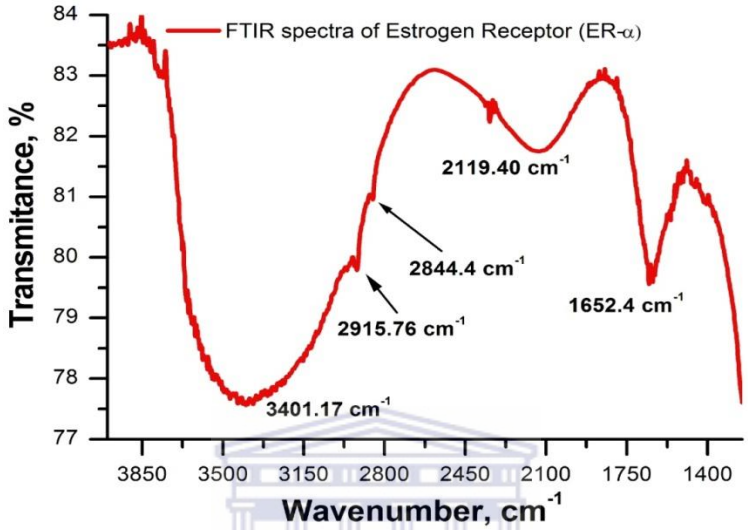

Figure 40: The FTIR spectrum of the ER-α.

In the FTIR spectrum presented in Figure 40, the IR bond properties of the ER-α were recognized; five distinct high transmittance percentage peaks at: 3401 cm^{-1}, 2915.76cm^{-1}, 2844.4 cm^{-1}, 2119.40 cm^{-1}, and 1652.4 cm^{-1} were obtained and associated with the amino acid residue's functional groups present at the conserved regions of the ER-α. The vibrational stretching frequencies observed in infrared spectrum of the ER-α were assigned to different function groups and presented in Table 4.

Table 4: Assignment of the FTIR vibrational transition bands, observed in the ER-α-spectrum.

Vibrating bond	**Stretching Frequency (cm^{-1})**	**% Transmittance**
A V(OH), (of carboxylic acid group)	3401	77.62
V(=CH), V(CH_2)	2915, 2844.14 (Doublet)	79.81, 80.95
C=N	2119.40	81.76
1. V(C=C) (Coates 2000) 2. V(C=O) (i.e. amide bonds) *(Strug, Utzat et al. 2012)* 3. V(i.e. disulphide bridges) *(Tetenbaum and Miller 2001)*	1652.47	79.65

The ER-α is associated with distinct amino acid residues that possess different reactivities and chemical behaviours. The ER-α aromatic amino acids; Tyr, Trp and Phe are associated with aromatic phenyl and indole rings respectively, with the infrared active alkyl and alkene bonds; the C-H, N-H, C=C, and C=N. The class-2 sulphur containing α-amino acids; cysteine (Cys) and methionine (Met) form disulphide bridges that are observed in the receptors or protein tertiary conformational structures, through their sulphide derivative-functional groups. The disulphide bridges (i.e. S-S covalent linkages) are usually quantified at wavelength regions below 1000 cm^{-1} (Li, Yamane et al. 2002, Biswas, Waring et al. 2007). The class-3 hydroxyl-amino acids; serine (Ser) and threonine (Thr) have (O-H) groups associated with the stretching frequencies; ν(0-H) that were observed at 3401 cm^{-1}. The other amino acids that possess the (O-H) functional groups;

in addition are the aspartic acid (Asp) and glutamic acid (Glu) residues of the ER-α are associated with R-linked carboxyl-functional groups that give rise to both the C=O and O-H stretching frequencies which are relatively infrared active.

Chapter 3 Quantum dot semiconducting nanomaterials

Quantum dots were used as intermediate semiconducting assemblies during the development of the estrogen receptor-α based biosensors. Bio-compatibility of the quantum dots can be observed through modification of their surfaces with biological-active functional groups such as: conjugated aromatic functional groups, amines, hydroxyls, carboxylic acids and mercapto-derived molecules, that are susceptible to cross-interaction with the liable chemical groups of receptors, proteins, enzymes and DNA biomolecules (Ding, Jones et al. 2003, Gill, Zayats et al. 2008, Li 2008). Estrogen receptor alpha (ER-α) biomolecules comprise of a number of amino acids associated with the amino acid sequences of the peptide bond linked amino acids; with occurrence of a frequent number of functional groups which are described in section 1.1.1 of Chapter 1. In this work, the quantum dots synthesized, were capped with 3-mercaptopropionic acid and mercaptosuccinic acids respectively. The bio-susceptible carboxylic acid terminuses (i.e. COOH groups) present at the capping agent chains of the 3-mercaptopropionic acid and mercaptosuccinic acid molecules respectively, initiate amidation reactions between the carboxyl acids of these 3-mercapto-carboxyl derived acids and the NH_2-funtional groups present in the ER-α amino acid sequence structure. Highly electroactive 3-mercaptopropionic acid capped quantum dots reconstituted the surface-electrochemical activity of the estrogen receptor-α based biosensors and great structural integrity of the ER-α bio-receptor molecules on the electrode surfaces. This chapter is designated to evaluate the theoretical aspects, physical, chemical, and electrochemical properties related to quantum dot nanomaterials developed in this study.

3.1. Contextualized research on quantum dots.

Quantum dots are nanomaterial recognized by their average particle sizes (APS) between (2-10) nm, with distinctive high crystalline surfaces due to their small particle sizes, close to 1 Angstrom (Å). A quantum dot bandgap can be controlled at molecular level, with access to the electronic confinement energy states in a sequence that is systematically consistence with their physical, electronic and chemical characteristics (Bailey and Nie 2003, Sun, Vasudev et al. 2009). Size-control of the quantum dot nanomaterials can be achieved through, control of the chemical composition and the reaction conditions such as the nucleation temperature, control over surfactant precursors and the stoichiometry during the quantum dots crystal growth processes (Li, Pradhan

et al. 2004). Colloidal synthesis of a quantum dot nanomaterials involves three precursor materials: a surfactant, a metal and a metalloid or an electron donor material (Nose, Omata et al. 2009). Quantum dots are highly crystalline semiconductors and sometimes referred to as: p-n, n, and p (i.e. positive-negative charged, negatively charged and positively charged, respectively) type semiconductors. Quantum dots continue to possess intrinsic properties due to their tuneable band gap-energies and the feasibility to surface modify them with various capping agents for their desired properties or applications (Pushpendra and Kedar 2009, Singh, Kang et al. 2009). This enormously expands their applicability in a variety of application-fields such as: optical devices development, used as microcircuit integrated materials, to improve the storage/memory capacity. Recently these quantum dot semiconductors nanocrystals have shown promissory progress in being used during the development of thin display devices for improvement of properties in existing light emitting diode devices (i.e. to improve features such as; brightness and fluorescence) (Suo, Su et al. 2010, Yang and Chang 2010). Studies on quantum dots nanomaterials with respect to their feasibility in optical device development have showed progress in being employed as substitute materials for the existing light emitting diodes due to their excellent quantum efficiencies. This is due to their; excellent photo-activity, high quanta energy brilliance and excellent magnetic properties extending their effective applications to domains such as; in data storage domains (Odoi, Hammer et al. 2006, Moreels, Kockaert et al. 2008, Munro, Bardecker et al. 2008, Stouwdam and Janssen 2008, Marques, Monte et al. 2009, Yang and Chang 2010). Electronic properties possessed by the quantum dots are related to their small electron semiconducting energy band gaps in the scale of less than 3.5 eV. Semiconductors differ from metals due to their probability to absorb electromagnetic radiation. The next figure, Figure 41, illustrates the absorption of photons in a metal and a semiconductor material (Read 1980).

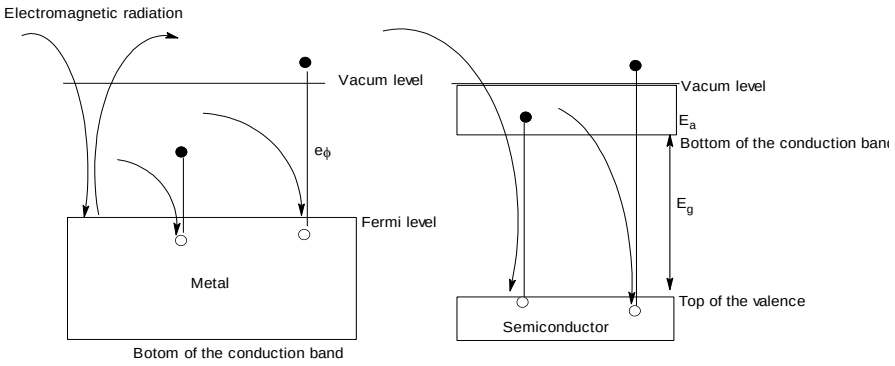

Figure 41: The conduction of the electromagnetic radiation in a metal and a semiconductor.

The conduction of electrons is dependent on the photon energy through the Fermi-Dirac distribution expression given in the equation, Equation 5;

$$dN(E)\alpha \frac{E^{1/2}dE}{e^{(E-E_f)/kT}+1}$$

Equation 5

The $E + dE$ expression gives the total energy of electrons at the conduction band of a metal. In Equation 5, the parameter E_f is the Fermi energy, k is the Boltzmann's constant and T is the temperature. The expulsion of the electron in a metal to the energy level above the vacuum can be possible when $hv > e\phi$ (i.e. hv is the applied electromagnetic radiation). The electron then will be excited just slightly below the Fermi level in the conduction band leaving a hole. In a semiconductor, however the electron must cross the E_g (i.e. band gap) and have enough activation energy (i.e. E_a) in order to reach the vacuum level or the energy above it; this implies that electromagnetic photon energy (i.e. hv) must be greater than $E_g + E_a$. An energy band gap configuration between the electronic energy states in a semiconductor-quantum dot is illustrated in Figure 42.

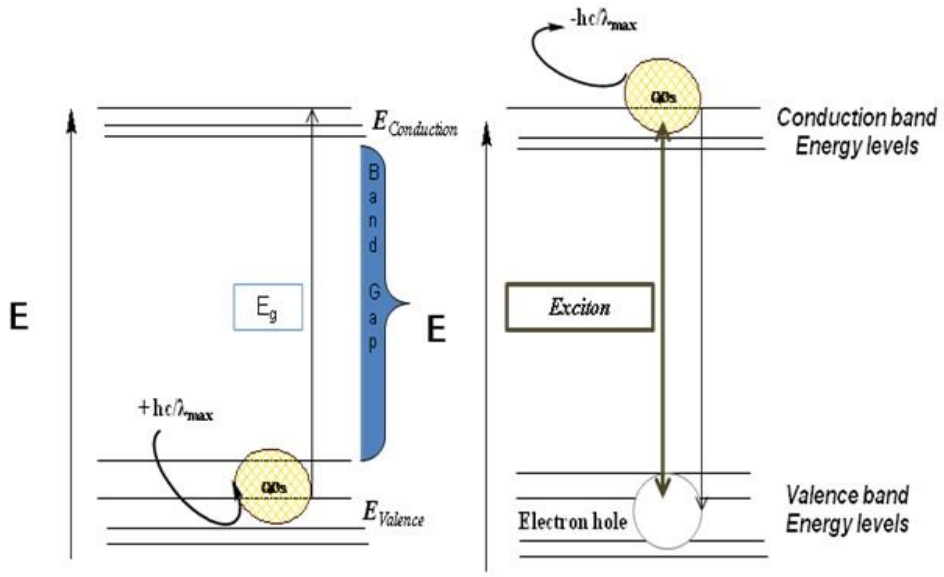

Figure 42: The confined state of a quantum dot semiconductor between the conduction and the valence bands.

A single quantum dot is excited ion the same manner as any another type of semiconductor crystal, by absorbing minimal amount of the excitation energy, inducing excitation of electrons between the two quantum state energy levels; from the ground state energy level within a valance band ($E_{Valence}$) to the exited state energy level {i.e. in the conduction band ($E_{Conduction}$)} (Sun, Vasudev et al. 2009). The excited state of a quantum dot molecule is metastable, therefore the quantum dot exciton spontaneously loses dynamism and transposes to lower energy because of the excited crystal instability, thus these ground state-excited state energy transitions are usually followed by the release of high photon energy photoluminescence or fluorescence radiation. A band gap energy (E_g) of a nanocrystal material is an intermediate energy gap between two quantum energy states configuration of; a $E_{Valance}$ band and a $E_{Conduction}$ band, that can be identified in scheme diagram presented in Figure 42. The ground state energy level (i.e. $E_{Valence}$) is a consequence of an electron donor (n- donor) electronic energy level associated with the quantum dot exciton. In contrast, the excited state energy level (i.e. $E_{Conduction}$ band) possesses electro-positivity associated with the quantum dot energy electronic energy states that are liable to accepting electrons (i.e. p-acceptors, where p denotes the positive charge). In consequence, the energy band gaps in quantum dots are created by electron-hole pairs called the excitons. Energy separation (i.e. donor-acceptor pair recombination energy; E_{DAP}) between an electron and a hole can be estimated through the

expression that is defined in Equation 6, where the electronic energy band gaps of the quantum dots, the donor material and acceptor materials (i.e E_g and E_D and E_A respectively) are related to the E_{DAP} by the expression given, Equation 6 (Nose, Omata et al. 2009).

$$E_{DAP} = \frac{E_g - E_D - E_A}{\varepsilon r}$$

Equation 6

The donor-acceptor recombination energy gap is represented by the parameter; E_{DAP}, E_g is the bulk energy band gap, E_D and E_A represent the band gap of donor and acceptor respectively, ε denotes the dielectric constant of a bulk material and r is the DPA separation radius. The relative dielectric constants are determined by the charge density relationship accounted to the charge flux density of; positive and negative charges; of the positive acceptor and negative donor materials respectively. In the presence of the applied voltage, the permittivity can be determined in relative to electromagnetic field between two charged particles with the charge separation distance (i.e. r) and a dielectric constant; ε, in an expression presented in Equation 7.

$$\sigma_\varepsilon = \frac{\varepsilon V}{r}$$

Equation 7

In the equation; σ_ε is the charge density and V is the applied voltage. The nanometre sized quantum dots exhibit unique properties such as; the electrical conductivity, magnetism (Mattram 1990, Yu, Chang et al. 2006), in addition to the excellent optimum luminescence properties that contribute to their excellent electrical properties. This research was proposed to combine the later described; electronic properties and biocompatibility observed in the quantum dot nanomaterials as alternative functional bio-materials used during the development of the estrogen receptor –α based biosensor. The research related to these nanomaterials have extended to their applicability in the herein, prescribed fields of biology; in bio-labelling (Shi, Rosenzweig et al. 2007, Walling and Novak 2009), biosensing (Gill, Zayats et al. 2008, Li 2008, Chan, Valencia et al. 2010, Ndangili, Arotiba et al. 2010). The quantum dots are being used as mediating site-specific laser probing materials in the bio-tagging industry, on implication of their high fluorescent efficiencies. In the

fields of therapeutics, they play a significant role in being used in drug-site specific target probes, on account of their high potential adequacy to surface encapsulation combined with their highly luminescent properties. Bio-material applications related to the quantum dots critically entails a low therapeutics index and quantum dots to adopt surface properties such as hydrophilic or/and hydrophobic surfaces. Consequently, surface modification via; ligation, surface passivity, and direct embedment of the quantum dot surfaces with the molecules; amino, hydroxyl, carboxylic-derived molecules, polymers, cells and other functional molecules, on their exterior chemical susceptible surfaces result in the pre-required surface characteristics, for their biological applications. Recently, the quantum dots have been reconnoitred successfully, and integrated with polymers; for application in photo-electronics and other relative biological applications (Oedzene and Karagozler 1999, Chen, Kuo et al. 2009).

3.1.1. Quantum dot growth approaches

Semiconducting material research is elaborate in many branches of sciences such as: in physics, engineering, material sciences, chemistry, and biology. High quality semiconducting single atom silicon and germanium quantum dots have been intensively researched for application in various domains of physics and material science (Alkhatib and Nayfeh 2013, Little, Karatutlu et al. 2014), since their discovery in the past century. Promptly, this invention initiated research on and the invention of several other single atom quantum dot systems and alloyed quantum dot super-lattices (Bailey and Nie 2003, Yang and Chang 2010, Soltani, Elham et al. 2012). Research on multi-layered growth assemblies of the quantum dots on pure semiconducting substrates have successfully shown their feasibility in development of complex high performance microelectronic, optical, semiconductor and sensing devices (Bailey and Nie 2003, Gill, Zayats et al. 2008, Anderson, Shircliff et al. 2010, Hildebrandt 2011). Properties such as small surface area, electric conductance, electric resistance, tuneable photoluminescence properties, and ability to control the size of quantum dots have accordingly made these nanomaterials popular in the prescribed fields of application. In contrast to the other growth approaches to producing the quantum dot nanocrystals researched up to present, the colloidal synthesis arises to distinctive; particle sizes, crystal configurations, atomic packing order, piezoelectricity, electronic resonance and photon energy state of the quantum dots nanomaterials (Yu, Chang et al. 2006, Baker and V. Kamat 2010). Superficial confinement regime, optical properties, molecular dynamism, electrochemical

properties, particle sizes, crystal and particle configuration of the quantum dots are corroborated through the herein described modulus operandi. The absorbance and photoluminescence spectroscopy, voltammetry, electronic microscopy (i.e. scanning electron microscopy (SEM) and transmission electron microscopy (TEM)), selected area diffraction microscopy (SAD), atomic force microscopy (AFM), etc., were reconnoitred to determine several properties exhibited by quantum dot nanomaterials, developed in the scope of this research.

3.1.1.1. Colloidal growth approach to quantum dot nanomaterials.

Colloidal nucleation of quantum dots is a prevalent growth technology of producing highly water-soluble or solution-phase quantum dot nanomaterials in chemistry. In this regarded methodology; ionic induced homogenous quantum dot films result into high quality crystalline quantum dots nanomaterials in solution, however defects such as; non-uniformity and formation of phase defects may arise, affecting; the surface density, optical efficiency and strain distribution (Leifeld, Hartmann et al. 1999, Li , Wang et al. 2007). Nevertheless, control over the parameters such as; the growth rate, stoichiometry have been successfully attested to be applicable in limitation of the imposed adverse defects in quantum dot nanomaterials (Liu, Wang et al. 2007, Wang, Cha et al. 2007). Colloidal grown quantum dots have found applications in diverse material-development fields, on account of improvement of the microelectronic devices such as: microelectronic sensors, infrared optical detectors, and electro-optical devices (Sun, Vasudev et al. 2009). A three-component system consisting of: the metal, an electron donor component and a capping agent describes the colloidal synthesis of binary atomic quantum dots. For bio-application of the quantum dots, an essential biocompatible encapsulating epi-layer assembled onto the quantum dot surfaces subside the toxicity levels and extends the bio-applicability of the quantum dots and in addition improves their chemical potential (Zhang, Zhou et al. 2003, Korlann, Riley et al. 2005). Nevertheless control over the composition and precursor ratio of; the metal precursor and the capping agent can alter different configurations of the quantum dot nanocrystals (Wang, Wang et al. 2002, Gill, Zayats et al. 2008, Hickey, Waurisch et al. 2008). At the establishment of this research, novel classical chemical bonding model was introduced on account of creating, quantum dots with distinct surface configurations through a systematically optimized and well established; molecular-electronic energy state and confinement regime in tin selenide quantum dots, capped with two different capping agents. Selenide based quantum dots of tin selenide (SnSe) capped with

mercaptopropionic acid and mercaptosuccinic acids were produced. A proposition of the colloidal growth process of the quantum dots explored in the scope of this work is presented; in section 3.2, that elaborates the development strategy of the tin selenide based quantum dots using stoichiometry.

3.2. Stoichiometry optimization; for the colloidal growth of the tin selenide based-quantum dots.

A growth procedure to the 3-mercaptopropionic acid capped; tin selenide quantum dots {i.e. SnSe (3-MPA)} quantum dots is described. The approximation of the discreet energy levels involved during the growth process of the SnSe quantum dots was determined through the described approximation expression; Equation 8.

$$E_n = \frac{hcR_\infty Z^2{}_{eff}}{n^2}$$

Equation 8

In Equation 8; E_n *r*epresents the energy level, $h = 4.1357 \times 10^{-15}$ eV. s; represents the Plank's constant, $c = 2.9972 \times 10^8$ ms^{-1}; is the speed of light, R_∞ is the Rydberg constant (i.e. $1.0973 \times 10^7 \mathrm{m}^{-1}$), Z_{eff} represents the effective nuclear charge and *n* is the nuclear number. The energy level estimation-expression described in Equation 8 was used to evaluate the electronic energy levels in; $SnCl_2.H_2O$, the 3-mercaptopropionic acid (3-MPA), $SnSe(3\text{-}MPA)_y$ quantum dots, and the Se, presented in Figure 43.

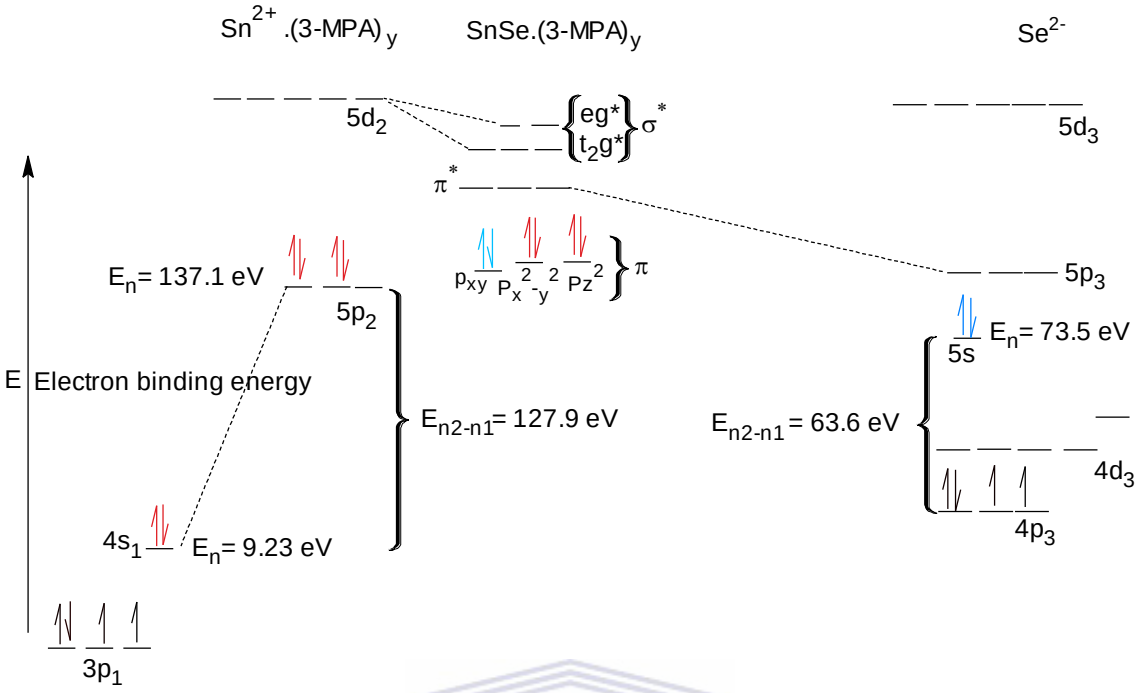

Figure 43: The electronic energy states of the tin selenide quantum dots, capped with 3-mercaptopropionic acid.

The confined energy states of the tin and selenide energy levels for each orbital involved during bonding between the Sn, Se and 3-mercaptopropionic acids were estimated with respect to;4s, 4p, 5s and 5p, the energy levels involved during molecular bonding. These values were reported in electron volts to be (9.2, 9.9, 73.5 and 137.1) eV, respectively for the prescribed orbitals shown in Figure 43.

3.2.1. Chemical synthesis and physical properties of the 3-mercaptopropionic acid capped tin selenide quantum dots {i.e. SnSe (3-MPA)}.

A capping moiety on the quantum dot outer interface enhances its biocompatibility, a superior benefit to applications of the quantum dots in biological systems; from bio-sensing, bio-imaging, and bio-tagging, have been extensively studied at various fields of chemistry and biological sciences. The biocompatibility properties of the quantum dots nanomaterials rely on the existence of either; a polar amine (i.e. NH_2), a polar carboxylic acid groups (i.e. COOH), or polar phosphate groups (i.e. PO_4^{3-}) on the quantum dot surfaces that can be polarized by either phosphate buffered matrix, polar water solvent matrix and other buffer solvents. These carboxylic acid capped

quantum dot surfaces can be cross-linked through condensation reactions, followed by hydrolysis reactions with the amine terminus tagged-biomolecules for the application of the quantum dots as biomaterials. The inorganic tin selenide quantum dots capped with 3-mercaptopropionic acid and mercaptosuccinic acids showed vibrational stretching frequencies at transmittance percentages below 30 % in the finger print region of the Fourier transform infrared (FTIR) spectroscopy studies, associated with the chemical rotation modes of the metal-metalloid semiconducting inorganic layer on the SnSe quantum dot surfaces.

Chemicals

Sodium boroydride of 99 % purity grade was used as the reducing agent for the selenium (Se) group (IV) metalloid, 3-mercaptopropionic and mercaptosuccinic acids were used as the capping matrix materials for the quantum dot surfaces and, the tin chloride dehydrate ($SnCl_2.2H_2O$) of 99 % purity grade was used as the metal precursor. All the quantum dot synthesis integral components were dissolved in Ris^{TM} automat purified distilled water. Chemicals used in this section of the study were of analytical grade and purchased from Sigma Aldrich, except $SnCl_2.2H_2O$ that was purchased from Riedel-de Haen. Sodium dihydrogen phosphate, disodium hydrogen phosphate that were used to prepare the buffer solutions were purchased from Sigma Aldrich. A 0.1 M phosphate buffer solutions (PBS) of pH 7.4 were prepared from sodium dihydrogen phosphate, disodium hydrogen phosphate in double distilled water filtered by Ris Millipore ^{TM} filtering system.

Instrumentation

Transmission electron microscopy (TEM) analysis of the materials, dispersed on a copper coated TEM grid were done using a Tecnai G2 F20X-Twin MAT 200 kV Field emission transmission electron microscope (i.e. from Eindhoven, The Netherlands). The atomic force microscopy (AFM) images were recorded on a Veeco Nanoman V atomic force microscope (i.e. from Veeco of Barbara, USA). Ultraviolet-visible (UV-Vis) absorption measurements of samples were done on quartz cuvettes in Nicolet Evolution 100 UV–Vis spectrophotometer (i.e. from Thermo Electron Corporation of Medison, USA). Fluorescence spectrometry measurements were done using Horiba JobinYvon fluorimeter (i.e. from Nano Log^{TM} of Cedex, France). All the electrochemical experiments were carried out using a BAS 100W cell integrated and automated electrochemical

work station {i.e. from Bioanalytical Systems Incorporated (BASi), West Lafayette, USA}. A 10 mL electrochemical cell with a conventional three electrode set up was used. The electrodes used for the electrochemical analysis were: (1) the gold working electrode with a geometric area of 0.0201 cm^2 and (2) a Ag/AgCl (3 M NaCl) used as a reference electrode both purchased from BASi. A third electrode (i.e. 3^{rd}) was the platinum wire that was employed as a counter electrode and was purchased from Sigma Aldrich. Alumina micro-polish powders of different particle sizes ranging from (i.e. 0.05 to 1) μm and 12" micro-cloths (i.e. purchased from Buehler of Illinois, USA) were used for polishing the working electrode surfaces.

3.2.1.1. Room temperature colloidal synthesis of tin selenide quantum dots; capped with 3-mercaptopropionic acid {i.e. SnSe(3-MPA)}.

Synthesis of the 3-mercaptopropionic acid capped tin selenide quantum dots was achieved through a similar procedure reported by authors; (Wang, Zhang et al. 2008, Ndangili, Jijana et al. 2011, Nxusani, Ndangili et al. 2012). In a separate reaction flasks; 2.65 $\times 10^{-5}$ moles of $SnCl_2.2H_2O$ (i.e. a metal precursor) was reacted via an ion-complexation reaction with 1.87 $\times 10^{-2}$ M 3-mercaptopropionic acid (i.e. a capping agent), in deionised water (i.e. a solvent) under the N_2 gas atmosphere at a pH of 11 for 2 h. In the second reaction flask a solution of 2.65 $\times 10^{-5}$ M NaHSe (i.e. semiconducting metalloid, electron donar precursor) was prepared by the reduction of 0.02 g of Se with 0.01 g of $NaBH_4$ in de-ionised water, under N_2 for 2 h. The equimolar NaHSe was slowly introduced onto the $SnCl_2.(MPA)_x$ reaction flask to initiate the growth and nucleation of the 3-mercaptopropionic acid capped, tin selenide quantum dots {i.e. SnSe(3-MPA)}. This reaction proceeded to completion for further 2 h. To digest the nucleation process of the SnSe(3-MPA) quantum dots, the solution was transferred to temperatures of approximately 4 °C and below for 10 minutes. The colloidal reaction protocol applied in the growth process of the water-soluble SnSe(3-MPA) quantum dots yielded quantum dots with high solubility in water, in addition, the synthesized quantum dots were highly crystalliferous. The quantum dot solution was stored at 4 °C and temperatures below to ensure prolonged feasibility and stability of the quantum dot nanocrystals. The quantum dot solutions were stable for 10 days at the predefined storage conditions. The alloyed SnSe mercaptopropionic acid capped quantum dots also produced in the scope of this research were synthesized through the same procedure, nevertheless a molar ratio of the; metal: secondary metal: metalloid: capping used was (1:1:2.5) respectively. The physical and

chemical properties of the terbium alloyed tin selenide quantum dots {i.e. Tb-SnSe(3-MPA)} were presented in the appendix section in Chapter 8.

3.2.1.2. Physical and chemical properties of the 3-mercaptopropionic acid capped tin selenide quantum dots {i.e. SnSe(3-MPA)}.

The quantum dot nanomaterial's particle size and physical surface properties were evaluated through the electron microscopy studies {i.e. using the transmission electron microscopy (TEM) and atomic force microscopy (AFM)}. The chemical reactivity and the biocompatibility of the SnSe(3-MPA) quantum dots films were verified through the FTIR characterization. The photo-electronic properties of the SnSe(3-MPA) films were evaluated using the ultraviolet to visible (UV-Vis) photo-spectrometry and fluorescence spectroscopy.

3.2.1.2.1. Particle shape, size and crystal configuration of the SnSe(3-MPA) quantum dots.

A 2 µL liquid droplet of the SnSe(3-MPA) quantum dot nanocrystals was deposited on a 2 mm diameter; spherical transmission electron microscopy (TEM) copper grid, all the TEM images were recorded at room temperature and are presented in Figure 44 (**A**) and Figure 44 (**B**).

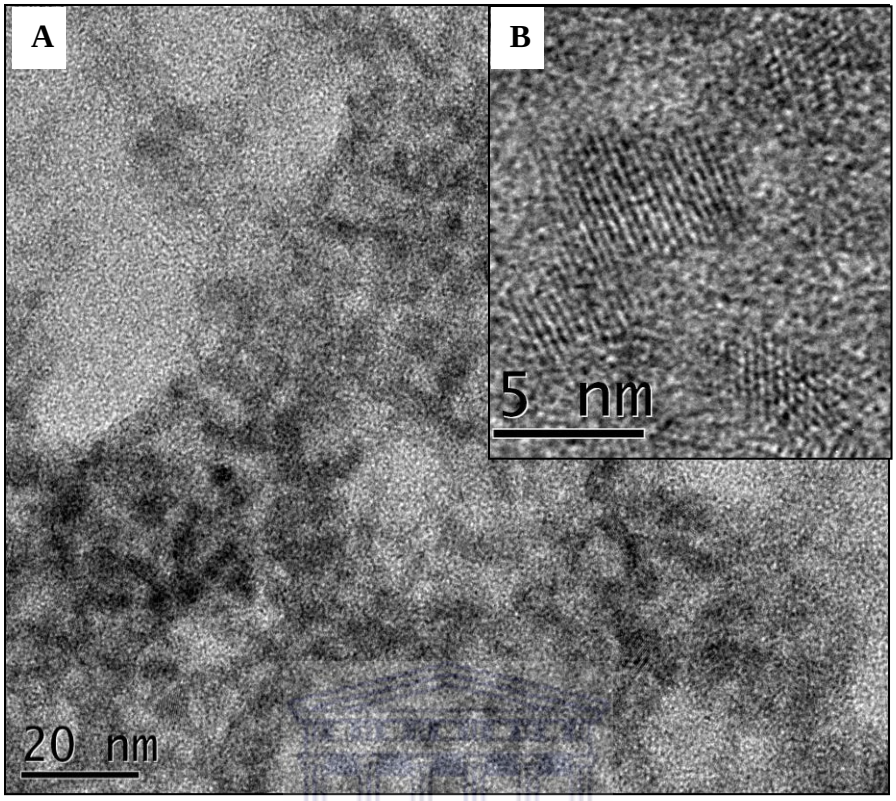

Figure 44: (**A**) The transmission electron microscopy (TEM) image of the SnSe(3-MPA) quantum dots at a projected 20 nm resolution and (**B**) the TEM image of the SnSe(3-MPA) quantum dots at a 5 nm resolution.

The TEM studies revealed spherical nanocrystals with particle size diameters in a nanometre scale range of less than 10 nm. The average particle size (APS) diameters of the SnSe (3-MPA) quantum dots evaluated using TEM was 4.6 ± 0.6 nm (i.e. this value was reported with its standard deviation). The SnSe(3-MPA) quantum dots particle size diameters, corresponded to the quantum dot-nanomaterials in an electronic confined state, with particle size radii close to Bohr atomic radius of 10 Å. Successive to the particle size evaluation of the SnSe(3-MPA) quantum dots, the crystal configuration, shape and crystallographic mapping of the quantum dots were corroborated through the selected area diffraction (SAD) microscopy. An SAD mapping of a single SnSe(3-MPA) crystal is presented in Figure 45, and was used to evaluate the crystallographic lattice symmetry in the proposed quantum dot nanocrystals. The quantum dot nanocrystals were mapped at the projected nanoscale SAD resolution of 5nm.

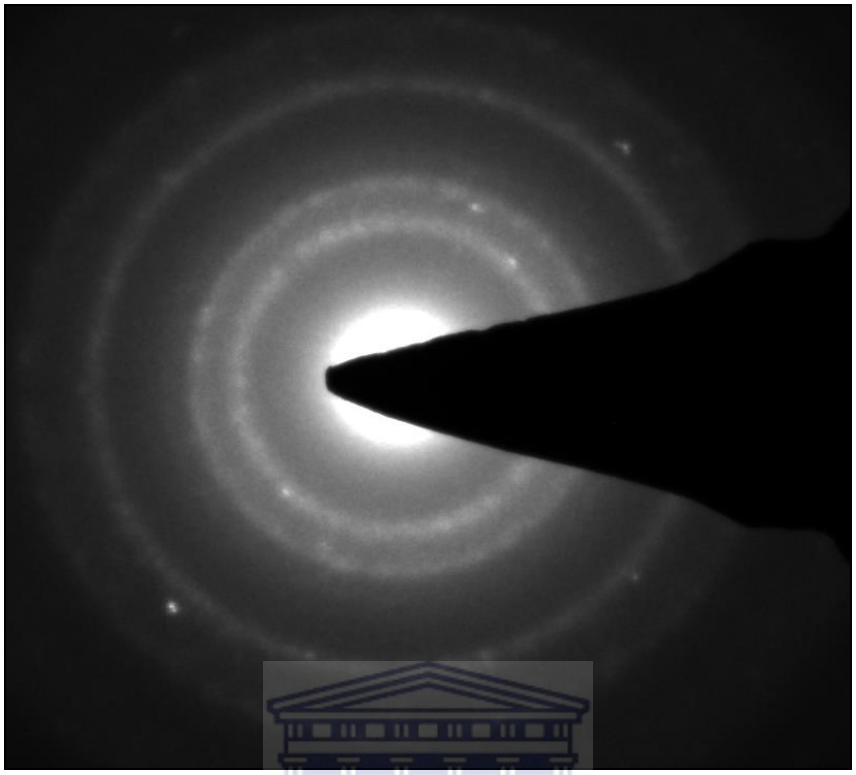

Figure 45: The selected area diffraction (SAD) image of a single crystal; SnSe(3-MPA) quantum dot at a projected 5 nm resolution.

The SAD crystallographic pattern of the SnSe(3-MPA) quantum dots revealed a ring crystal with a d-spacing of 0.8 nm with the electron condensed transmitted core and relatively crystalline diffraction pattern (Norako, Greaney et al. 2012). The crystal diffraction pattern observed at a single Bragg's angle of diffraction in the SnSe(3-MPA) quantum dots was related to a close packing polycrystalline (ccp) ordered lattice configuration, determined using the reference indexing conveyed by; (Lin 2014). The electron diffraction pattern of a single crystalline SnSe(3-MPA) quantum dot was then distinguished by performing the near field TEM studies presented in Figure 46.

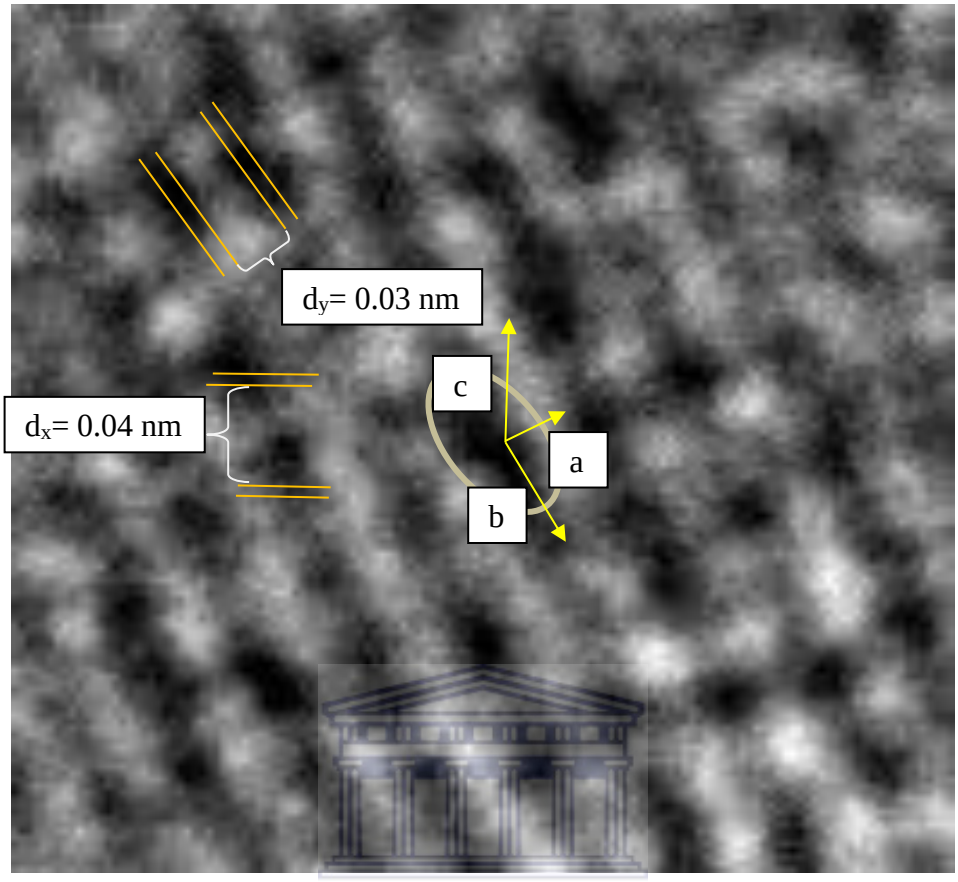

Figure 46: The transmission electron microscopy (TEM) image of a single crystal SnSe(3-MPA) quantum dot at a resolution of 5 nm.

The diffraction patterns evaluated at the single Bragg's angle of diffraction determined from a fringe pattern in TEM configuration of the SnSe(3-MPA) quantum dots, in Figure 46 were related to a close packing ring face-centred orthorhombic polycrystalline ordered atoms (Bjorge, 2007). The lattice arrangement of the atoms on the defined face-centred closely packed polycrystalline SnSe(3-MPA) quantum dot crystal-structures were determined by the reciprocal lattice vectors from the direct space TEM lattice patterns. The d-lattice spacing was evaluated through the herein, defined equation; Equation 9.

$$d = \frac{2\pi}{\lceil g_{lmn} \rceil}$$

Equation 9

The *d* (i.e. atomic spacing) value of 0.03 nm was evaluated, g_{lmn} is the volume of a single unit cell of the SnSe(3-MPA) quantum dot crystals and was determinable from the reciprocal lattice plane vectors (i.e. a, b and c) outlined in Figure 45, characterized by the reciprocal unit cell volume (g_{lmn}) of 0.26 pm^3.

3.2.1.2.2. Surface topography studies of the SnSe(3-MPA) quantum dots, characterized through atomic force microscopy (AFM).

The tin selenide, 3-mercaptopropionic acid capped quantum dot-nanocrystal's surface topography-properties were evaluated using the atomic force microscopic (AFM). The analysis of the SnSe(3-MPA) films deposited on a silicon substrate were studied at the vacuum, AFM detector and the surface topography formation of the quantum dot films was mapped, and is presented in Figure 47 and Figure 48.

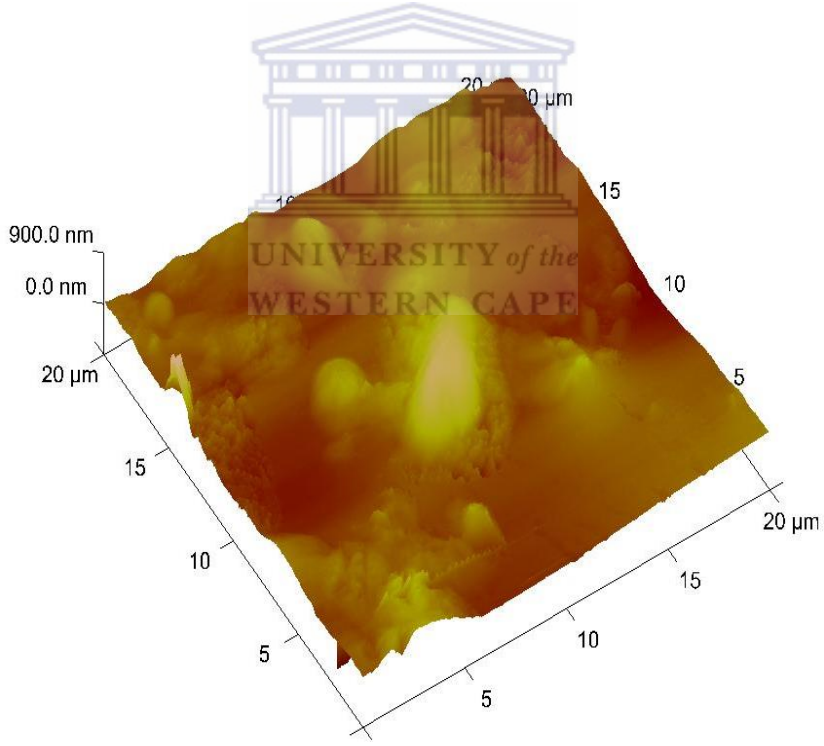

Figure 47: The atomic force microscopy (AFM), topographic mapping of the SnSe(3-MPA) quantum dot nanocrystals deposited on the silicon substrate.

In the atomic force microscopy AFM image outlined in Figure 47, a surface topographic map of the SnSe(3-MPA) nanocrystals is distinguished by distinct smooth surface of highly crystalline

and electron condensed quantum dot films with, minimal surface-coverage defects. The bi-phasic layer observed in the surface formation on the SnSe(3-MPA) nanocrystals (i.e. distinguished by the deviations in the electron confined surface depth) was suggested to be caused by different polarities; of the quantum dot capping, 3-mercaptopropionic acid and the semiconducting SnSe quantum dot inorganic core. In order to evaluate; the surface roughness and film depth, the cross-sectional AFM surface topography of the SnSe(3-MPA) quantum dot crystals was mapped and is presented in Figure 48 (**A**) with spectral interface profiles that are presented in Figure 48 (**B**) and Figure 48 (**C**).

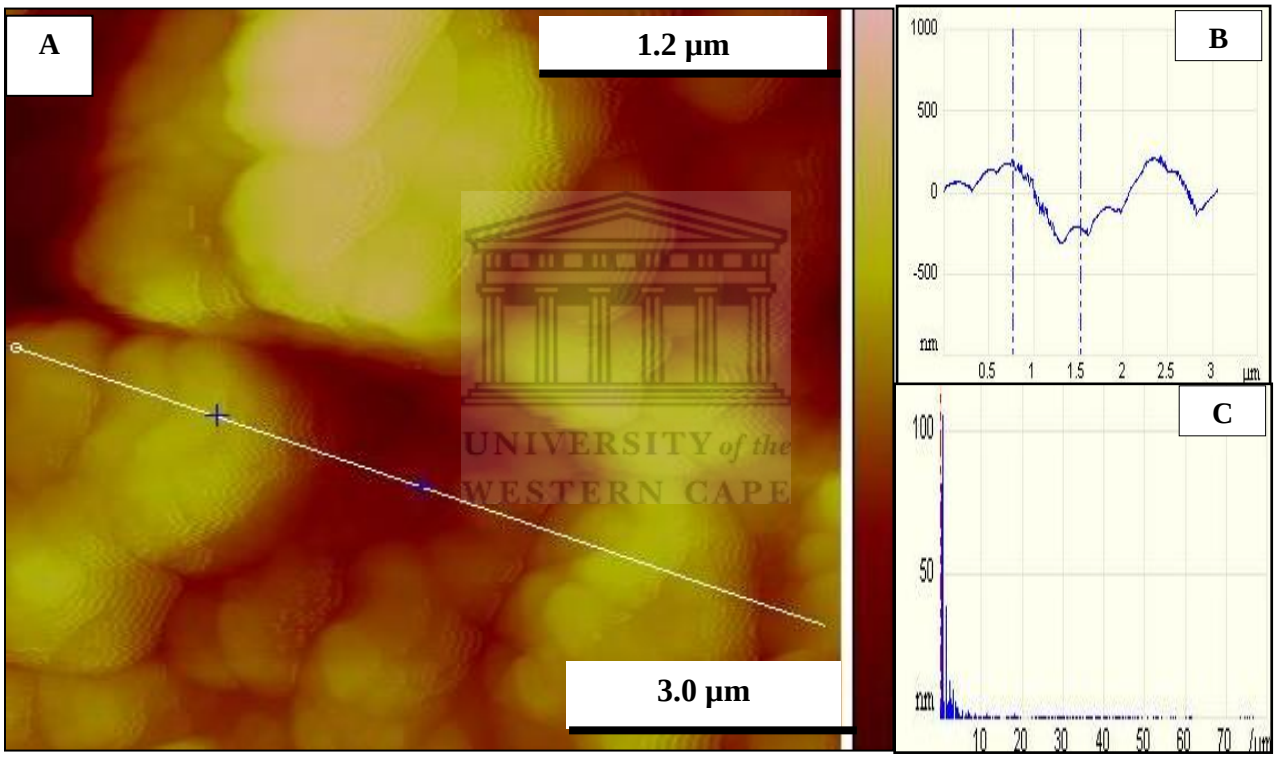

Figure 48: (**A**) The cross-sectional AFM surface mapping of the SnSe(3-MPA) quantum dot films on a silicon substrate, (**B**) the AFM surface depth profile of the SnSe(3-MPA) quantum dots and (**C**) the surface roughness measurements.

In the cross-section AFM image presented in Figure 48 (**B**), the surface roughness was determined at the reflective angle of -27°. The surface roughness studies of the SnSe(3-MPA) quantum dot films indicated slightly rough surfaces, with a mean surface roughness average (R_a) of 169 nm. The average surface roughness of materials or modified surfaces is related to their adhesion properties (Kuma and Rao 2012). In Equation 10, surface roughness is highly reciprocal to the

surface adhesion characteristics of the materials through, the adhesion force (i.e. *F*) expression outlined in the given equation; Equation 10 (Oliveira, 2012).

$$F = 2\pi\omega R\left[\frac{R_q}{R + R_q} + \left(\frac{h_c}{h_c + R_q}\right)^2\right]$$

Equation 10

In Equation 10, the parameter; F is the measure of the contributing total forces including Van De Waals forces contributed by the atomic covalent bonds of the SnSe(3-MPA) quantum dot nuclei, the R_q parameter indicates the root mean square roughness (RMS), ω is the separation distance frequency and indicates the correlation of the surface roughness with the frequency, and h_c is the tip-sample separation distance. The surface roughness is highly collaborated to a high probability of the electrochemical intercalation behaviour exhibited by compounds, molecules or materials that affects their chemical reactivity and behaviour.

3.2.1.3. Optical properties of the SnSe(3-MPA) quantum dots.

The absorbance properties of the SnSe(3-MPA) quantum dots were evaluated on liquescent-quantum dot films, synthesised by a procedure, described in section 3.2.1.1 and subjected to 10 times dilution on 1 cm length quarts cuvettes, these studies were carried out at room temperatures. The ultraviolet-visible (UV-Vis) spectroscopic studies were evaluated at the absorbance wavelength window between; 200 nm to 350 nm, for evaluation of the absorbance properties of the SnSe(3-MPA) quantum dots and are presented in Figure 49, at different molar concentrations of the capping agent; 3-mercaptopropionic acid.

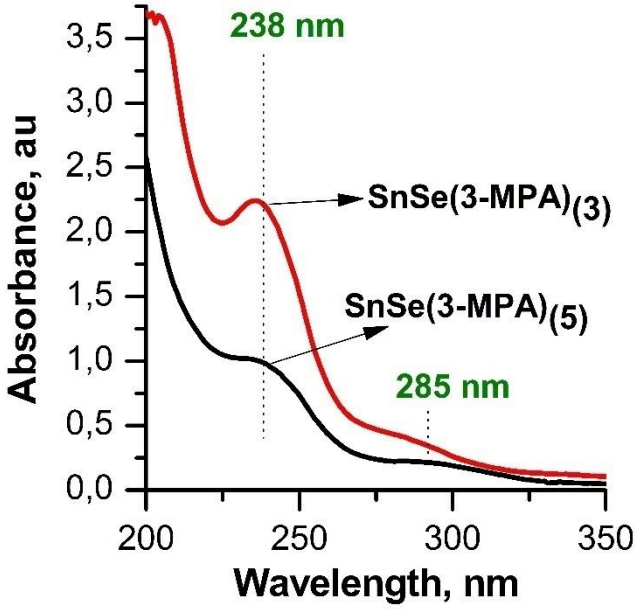

Figure 49: The UV-Vis spectrum of the SnSe(3-MPA) quantum dots at different molar ratios of the 3-mercaptopropionic acid capping.

The UV-Vis absorbance profile of the SnSe(3-MPA) quantum dots revealed maxima wavelength peaks at the λ_{max} magnitudes of; 238 nm and 285 nm, highlighted in Figure 49. The regulation of the molar ratio between the metal precursor and the 3-mercaptopropionic acid capping agent, from 1:3 (i.e. presented by a red spectra) to 1:5 (i.e. black spectra), during the synthesis of the SnSe(3-MPA) quantum dots resulted to a decrease in the absorbance of the UV-Vis wavelength of the quantum dots from 2.24 to 0.98. Nevertheless, no notable electronic transition deviations in the absorption wavelengths were observed, this was an implication of the quantum dots nucleation incongruities caused by the high saturation level of the capping agent molecules on the quantum dot surfaces. The band-edges of the quantum dot nanomaterials predominately occur at the visible region of the absorbance spectra between 250 nm and 700 nm, and can be associated with the nanoparticle size radius-correlation equation, presented by Equation 11.

$$E_g^{bulk} - E_g^{nanoparticle} = \frac{h^2}{8r^2}\left(\frac{1}{m_e^*} + \frac{1}{m_h^*}\right)$$

Equation 11

The parameters; E_g^{bulk} and $E_g^{nanoparticle}$ are the band gaps of the bulk and nanoparticles solutions respectively. Plank's constant is presented by the notation; *h*, *r* is the particle radius (Kovalenko, Bodnarchuk et al. 2004). A direct band gap of 1.856 eV was obtained for the proposed; SnSe(3-MPA) quantum dots nanomaterials, evaluated at the absorbance band edge. The direct band gap of the SnSe(3-MPA) quantum dots was determined to be within the band gap range of the semiconductor materials {i.e. 0 eV ≤ E_g ≤ 4 eV (Strehlow and Cook 1973)} . The direct band gap energy structure of the confined electronic energy states (i.e. the valance band and conduction bands) of the SnSe(3-MPA) quantum dots is presented in Figure 50.

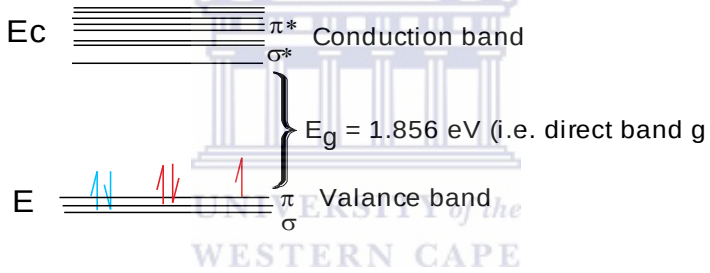

Figure 50: Configuration of the energy band gap of the SnSe(3-MPA) quantum dots.

The photon energy indirect band gap in SnSe(3-MPA) quantum dots was estimated from Tauc's relation equation (Scott D., Andrew E. et al. 2005, Kumar and Singh 2009, Yang and Chang 2010, Shen, Que et al. 2011) presented in Equation 12. The absorbance co-efficient (i.e. α) and the photon energy (i.e. $h\upsilon$) of materials are related to the indirect band gap energy (i.e. E_g) by the relationship highlighted in the next expression; Equation 12;

$$\alpha h\upsilon = c(h\upsilon - E_g)^{1/2}$$

Equation 12

In Equation 12, *h* is the Planks constant, *c* is the speed of light, υ is the frequency of the absorbed photons. A photon energy; indirect band gap estimation profile of the SnSe(3-MPA) quantum dots is presented in Figure 51.

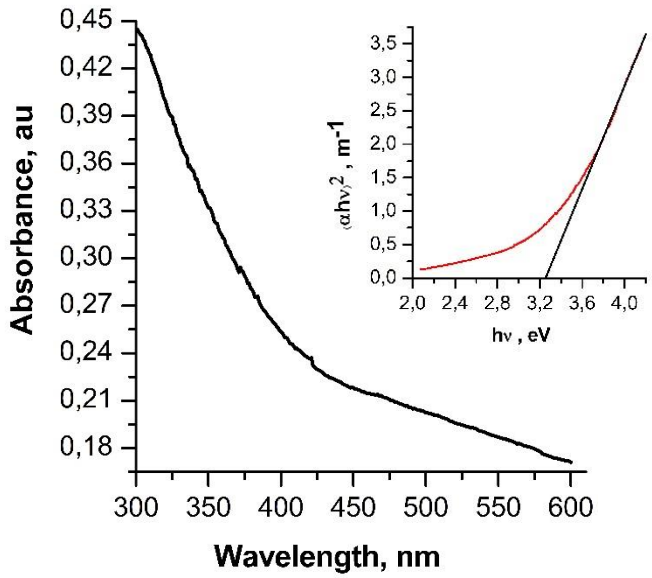

Figure 51: The indirect band gap estimation of the SnSe(3-MPA) quantum dots**.**

The indirect band gap of the SnSe(3-MPA) quantum dots was approximated to be 3.254 eV, an apparent semi-conducting character of the proposed quantum dot nanocrystals. The relative photo-electronic properties of the SnSe(3-MPA) quantum dots were consequently corroborated using fluorescence spectroscopy. For fluorescence spectroscopy studies; the thin films of SnSe(3-MPA) quantum dots were subjected to 10 times dilution {i.e. using 2µL SnSe(3-MPA) stock solution}, and the emission properties of the proposed quantum dot nanomaterials were evaluated on liquescent materials using quartz cuvettes with a path width of 1 cm. The SnSe(3-MPA) quantum dots were excited at a band edge wavelength (i.e. λ_{ex}) of 382 nm and the fluorescence spectroscopy data were recorded at the broad spectral wavelength range between 390 nm and 500 nm. The fluorescence profile of the SnSe(3-MPA) quantum dots is presented in Figure 52 (**A**), with the relative absorbance profile. The electronic transitions associated with the fluorescence properties of the SnSe(3-MPA) quantum dots were further corroborated in Figure 52 (**B**).

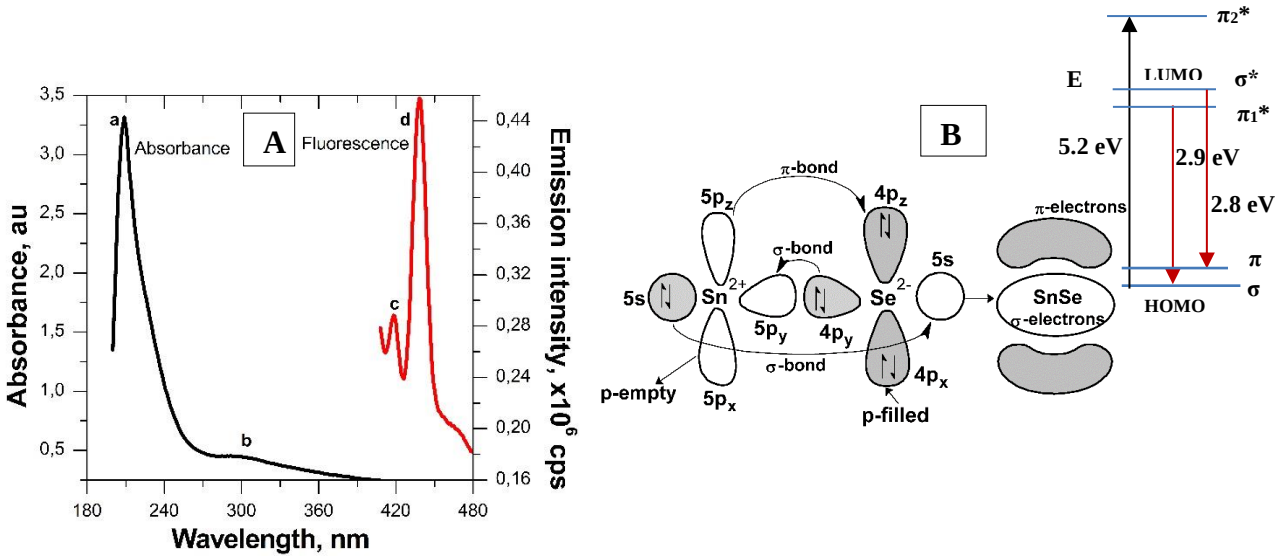

Figure 52: (A) The absorbance and fluorescence spectra of the SnSe(3-MPA) quantum dots and, (**B**) the relative electronic transitions in SnSe(3-MPA) quantum dots.

High energy maximum emission peaks (i.e. $\lambda_{emission}$) were observed at wavelengths; 425 nm and 449 nm {i.e. labelled a = 2.9 eV and b = 2.8 eV, respectively in Figure 52 (**A**)}. The absorbance/emission properties observed in the SnSe(3-MPA) quantum dot fluorescence profiles were related to the electronic transitions in Figure 52 (**B**). The black arrow in Figure 52 (**B**) indicates the electronic transition, due to the excitation of an exciton at the HOMO (i.e. either at the σ-electron or the π-electron at the ground state), to the LUMO (i.e. conduction band at the π_2^*-underlying non-bonding orbitals). This transition is however associated with the absorption of 5.2 eV, photon energy by the SnSe(3-MPA) quantum dots. In contrast the electronic energy transitions associated with the emission of fluorescence were observed, with low band gap energies of; 2.8 eV and 2.9 eV respectively {i.e. these electronic transitions were indicated by red arrows in Figure 52 (**B**)} . The summary of the fluorescence properties exhibited by the SnSe(3-MPA) quantum dot excitons are corroborated in Table 5 .

Table 5: The absorbance and the corresponding emission electronic transitions in SnSe(3-MPA) quantum dots.

Absorbance energy electronic transition	Related emission energy electronic transitions
$\pi \rightarrow \pi_2^*$, $E_{V\text{-}C}$ = 5.2 eV ($E_{v\text{-}c}$;describes the energy barrier between the valance band and the conduction band)	$\pi_1^* \rightarrow \sigma$, $E_{C\text{-}B}$= 2.9 eV
	$\sigma^* \rightarrow \pi$, $E_{C\text{-}B}$= 2.8 eV

A perceptible inter-system crossing was suggested, supported by an inordinate decrease in the electronic energy band gap of the absorbance and the relative emission photon energies from 5.2 eV to 2.8 eV respectively by a value of 2.3 eV. Comparatively, a difference in the absorbance and emission wavelengths observed in the SnSe(3-MPA) quantum dots (i.e. $\lambda_{absorbance\ max} - \lambda_{emission\ max}$) was estimated to be 149 nm, indicating a bathochromic shift. This was approximately four times greater than a bathochromic shift of 37 nm estimated from reciprocal excitation and emission wavelengths (i.e. $\lambda_{excitation\ max} - \lambda_{emission\ max}$) of the quantum dot-exciton; associated with the excitation maxima ($\lambda_{excitation\ max}$) value of 285 nm and the first emission peak ($\lambda_{emission}$) with the magnitude of 426 nm. These values were estimated from the excitation and emission profiles presented in next figure; Figure 53 (**B**). The fluorescence excitation and emission properties of the SnSe(3-MPA) quantum dots were evaluated at the fluorescence wavelength region between 280 nm to 640 nm, the spectra are illustrated in Figure 53 (**A**) and the related electronic transitions are presented in Figure 53 (**B**).

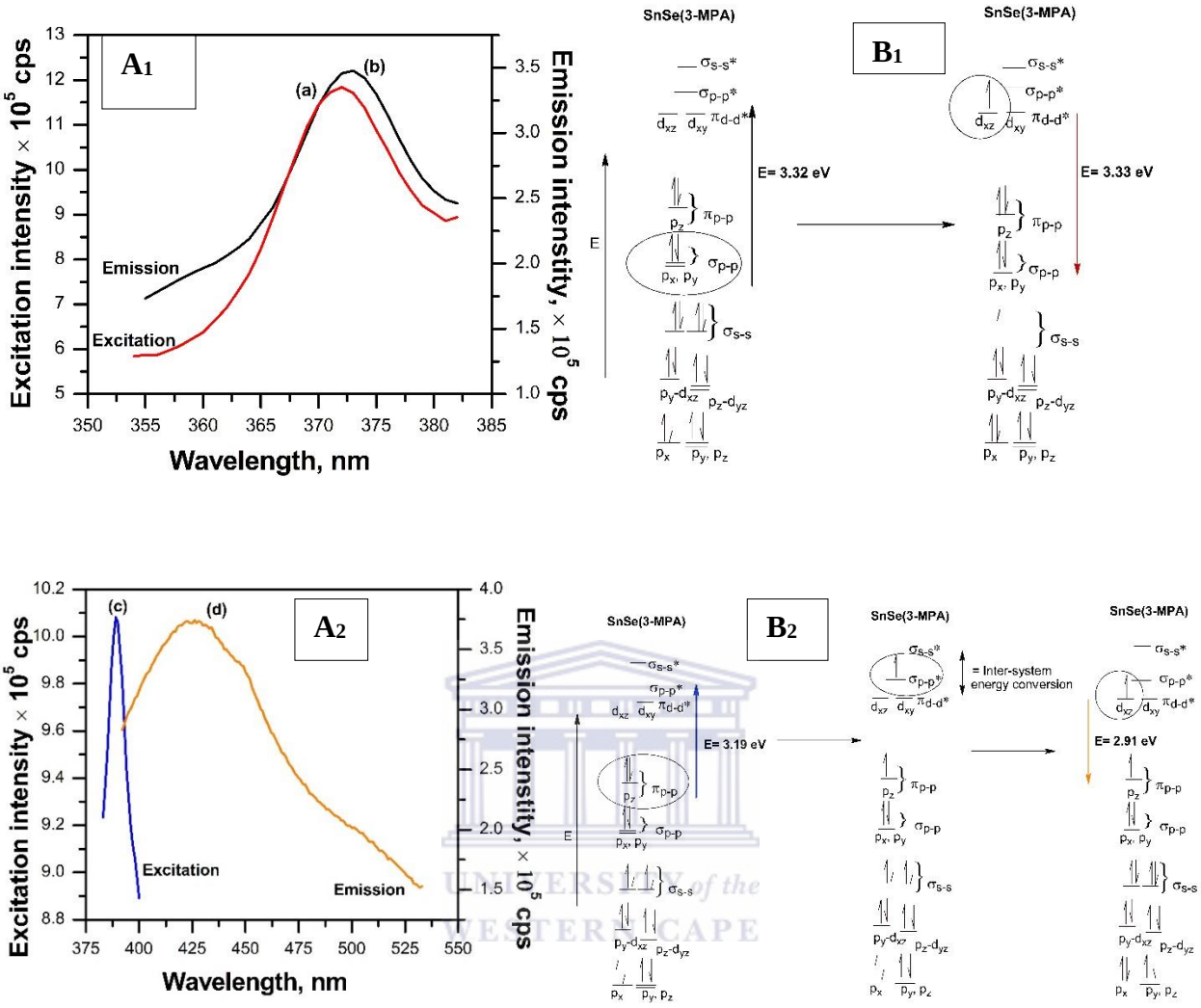

Figure 53: (A_1 & A_2) The fluorescence spectra of the SnSe(3-MPA) quantum dot films and (**B_1 & B_2)** the related excitation and emission electronic transitions.

The fluorescence spectra of the SnSe(3-MPA) quantum dots revealed high intensity maximum emission peaks at a wavelength range between 340 nm and 700 nm; associated with the emission brightness intensities between 4×10^5 cps and 20×10^5 cps. The electron transitions observed in the spectra of the SnSe(3-MPA) quantum dots were described through the electronic transition diagrams presented in Figure 53 (**B**) (i.e. Figure 53 $\mathbf{B}_1$ and Figure 53 $\mathbf{B}_2$). The peak at; (a) (i.e. 3.32 eV) and (c) (i.e. 3.3 eV) were a resultant of the $\sigma_{p\text{-}p} \rightarrow \pi_{d\text{-}d}^*$ and $\pi_{p\text{-}p} \rightarrow \sigma_{p\text{-}p}^*$ electronic transitions respectively, between the pi and the sigma bonding orbitals of the SnSe(3-MPA) quantum dots, highlighted in Figure 53 (**B**). The emission peaks that are observed at; (b) and (d) in the spectra

presented in Figure 53 (**A**), are the emission energy peaks corresponding to the electronic transitions; $\pi_{d\text{-}d}^{*} \rightarrow \sigma_{p\text{-}p}$ and $\pi_{d\text{-}d}^{*} \rightarrow \pi_{p\text{-}p}$ associated with emission photon energies of 3.3 eV and 2.91 eV respectively. The fluorescence spectroscopy properties of the SnSe(3MPA) quantum dots were further explicated using the time correlation fluorescence spectroscopy, a decay profile of the SnSe(3-MPA) quantum dot films was recorded to evaluate the life time of the absorbed photons in the excited state of the SnSe(3-MPA) quantum dots. Emission decay profiles of the SnSe(3-MPA) quantum dots are described, through the time-dependent fluorescence spectra presented in Figure 54.

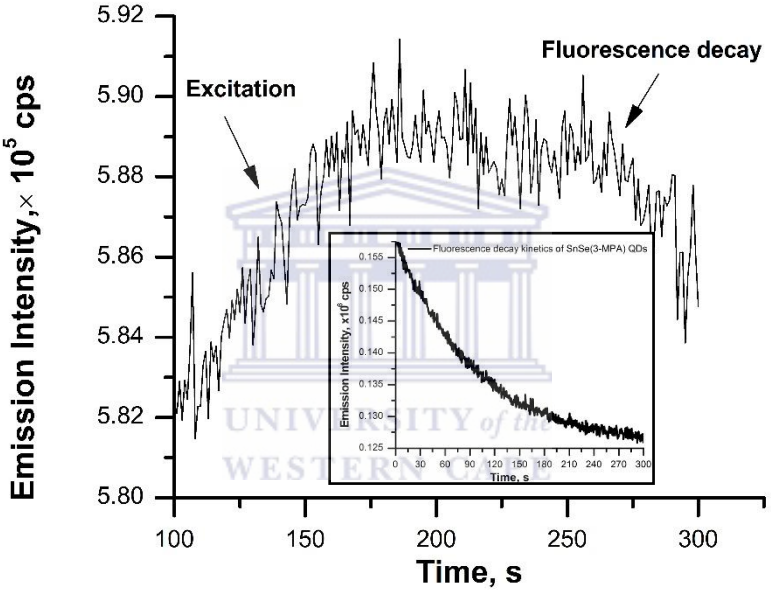

Figure 54: The fluorescence vs time decay curve of the SnSe(3-MPA) quantum dots.

A decay profile of the SnSe(3-MPA) quantum dots revealed the degradation of the fluorescence energy intensity from 157000 cps (i.e. at t =0 s) to 127000 cps (i.e. at t= 200 s). The fluorescence excited state life-time was evaluated with reference to the proposed exponential decay expression highlighted in Equation 13, where the indirect fluorescent life-time (i.e. τ_f) with the magnitude of 150 s, of the excited state of the SnSe(3-MPA) quantum dots was determined.

$$\lim_{t\to 0}\frac{\Delta d(fluoresence\ intensity)}{\Delta dt} = f(t)= 3.2\times10^{3}e^{-x/96.5}+ 1.25\times10^{5}$$

Equation 13

In the proposed equation *f(t)* is the function representing the obtained decay curve of the SnSe(3-MPA) quantum dots related to its time-depended emission life time properties {i.e. with reference to the decay curve in the insert of Figure 54) , t is the time in seconds. The quantum yield and quantum efficiency of the SnSe(3-MPA) quantum dots were evaluated using the absolute method (Nose, Omata et al. 2009) and determined to be 0.002 and 0.17 % respectively.

3.2.1.4. Chemical bond properties of the SnSe(3-MPA) quantum dots.

The SnSe(3-MPA) quantum dots structural properties were extrapolated using Fourier transform infrared spectroscopy (FTIR). The FTIR spectral data acquisition was evaluated between 300 cm^{-1} and 4000 cm^{-1} infrared frequencies. The FTIR spectra presented in Figure 55, denotes the chemical bond properties of the Sn^{2+}(3-MPA) complex precursor and the SnSe(3-MPA) quantum dot liquid samples on sodium chloride beads.

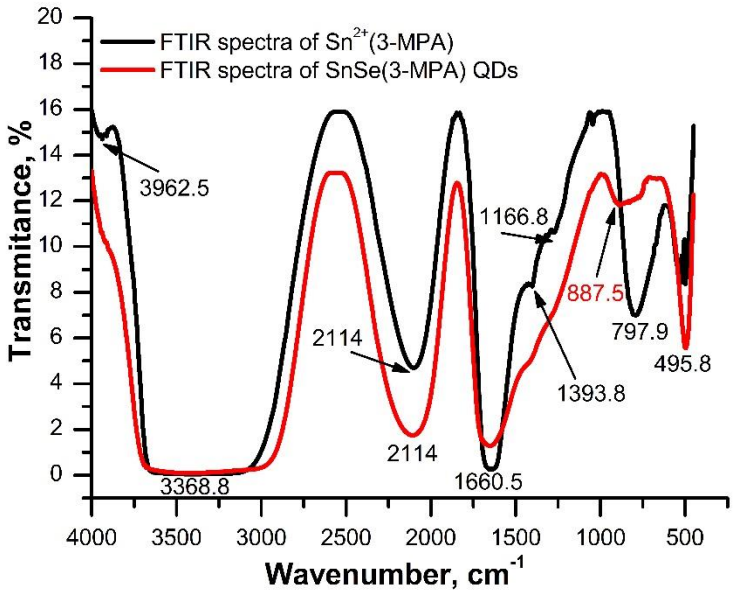

Figure 55: The FTIR spectrum of: Sn^{2+}(3-MPA) (**BLACK**) complex, and the SnSe(3-MPA) (**RED**) quantum dot films.

The infrared spectroscopic chemical bond properties of: (a) Sn^{2+}(3-MPA) and (b) SnSe(3-MPA) films respectively were further de-convoluted and summarised in the succeeding table,Table 6 illustrating the different stretching and bending modes of the herein prescribed materials.

Table 6: The FTIR vibrational transition bands in Sn^{2+}(3-MPA) complex and SnSe(3-MPA) quantum dot films.

Chemical bond stretches or bends	**Stretching Frequency (cm^{-1})**
1. ν(C-H)	3962.5
2. ν(O-H)	3368.8
3. ν (C-O)	2114.
4. ν (C=O)	1660.5
5. ν (C-H)	1393.8, (i.e. bending frequency mode at the C-H bonds of the 3-mercaptopropionic acid capping)
6. ν (C-O)	1166.7, Strong
7. **ν(Sn-Se)**	**887.5 (i.e. with T= 11%)**
8. ν(Sn-S)	797.9
9. ν(C-H)	495.8 (i.e. the bending frequency mode at the alky chain of the 3-mercaptoproinoic acid capping matrix).

Functional group transmission stretching frequencies evaluated in Table 6 were secondarily assigned to the structural bond properties of the SnSe(3-MPA) quantum dots and tin metal complex {i.e. Sn^{2+}(3-MPA)} used as a precursor material for the colloidal grown SnSe(3-MPA) quantum dot. The synthetic route to growth of the SnSe(3-MPA) involves an overall second order reaction, and is distinguished by; the stepwise substitution reaction followed by the complexation of the Sn-metal centre with the capping agent molecules prior the final nucleation and production of the SnSe(3-MPA) quantum dots. The chemical reactions involved during the growth of the SnSe(3-MPA) quantum dots are described, in Figure 56.

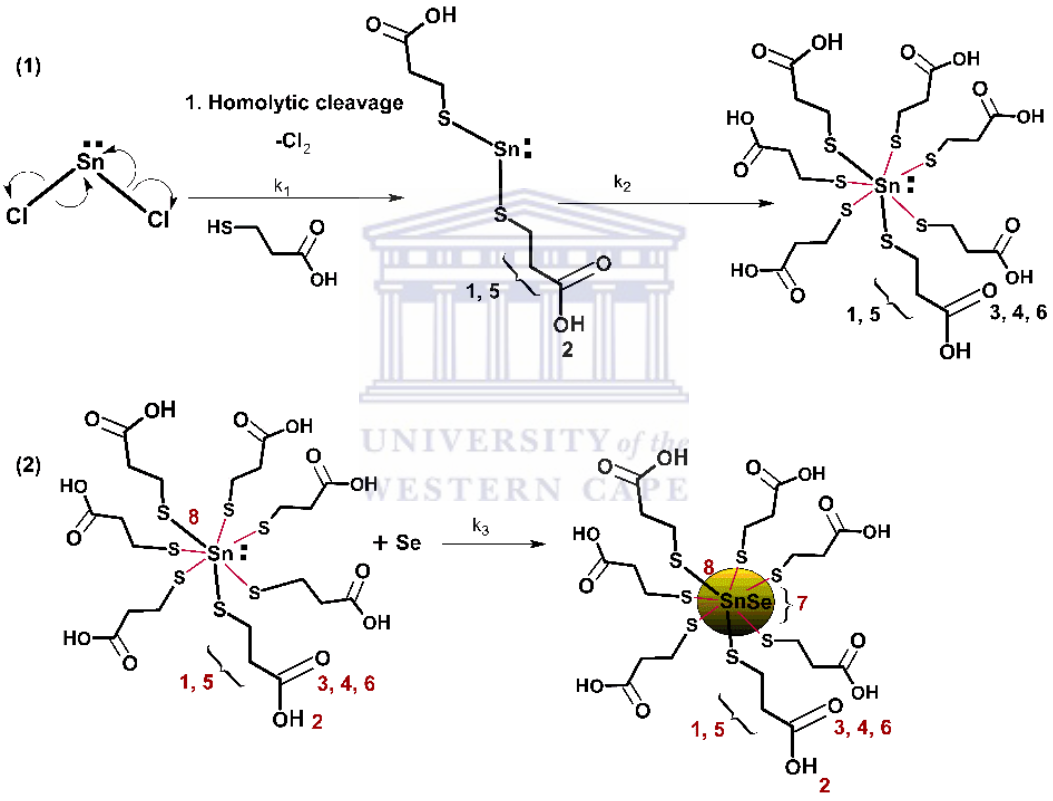

Figure 56: The reactions involved during the growth process of the SnSe(3-MPA) quantum dots**.**

The homolytic bond cleavage with the designated reaction rate constant (i.e. k_1) in Figure 56, after completion, is further followed by the dehalogenation reaction and the formation of the covalent linkages between the 3-mercaptopropionic acid molecules and highly reactive tin metal centre; acting as an electron acceptor. The resultant reaction then results into production of a Sn^{2+}(3-MPA) complex, characterised by the first order reaction rate constant k_2. The ionic intercalation of the selenium ions into the tin metal centre is characterised by the first-order reaction, with the reaction

rate constant; k_3. The final reaction during the colloidal growth of the quantum dot nanomaterials is the nucleation of the quantum dots nanocrystals. The numbering on the molecules in Figure 56 corresponds to the numbering system in the description of the infrared stretching frequencies; in Table 6. The stretching frequencies υ = 3962.5cm^{-1}, 3368.8cm^{-1}, 2114cm^{-1} and 1660.5 cm^{-1} assigned in Table 6 were related to the chemical bond properties of both the Sn^{2+}(3-MPA) complex and the SnSe(3-MPA) quantum dots nanomaterials. A decrease in the transmittance percentage from 7 % to 1.3 % with reference to the; υ(C-O) stretching frequency at 2114 cm^{-1} was observed in the spectra of the Sn^{2+}(3-MPA) complex and the SnSe(3-MPA) quantum dots respectively. A decrease in transmittance indicates a change in the plane of symmetry adopted by a molecule or a chemical bond, in this context, the rotation of the tin metal centre to a different plane of symmetry around the C-O bond in the presence of Se at the Sn centre was related to a very low transmittance index of the selenium (Se) metalloid. The transmittance percentage is related to the stretching frequencies by the next equation, Equation 14.

$$\% T = e^{-\varepsilon l c}$$

Equation 14

The percentage transmittance is defined by the percentage parameter (i.e. % T), ε is the molar absorptivity, l is the path length, and c is the concentration of the transmitting molecules. The conversions of the transmittance properties between the tin-inorganic core of the Sn^{2+}(3-MPA) complex and the SnSe(3-MPA) quantum dots were also observed at the fingerprint region of the FTIR spectrum of the two molecules at; 887.5 cm^{-1} and 797.9 cm^{-1}, related to the assigned stretching modes associated with the υ(Sn-Se) and υ(Sn-S) bonds respectively. An increase in the transmittance from 7 % to 11.5 % observed at υ(Sn-S); at 797.9 cm^{-1} was the implication of the highly electron conductive crystalline SnSe(3-MPA) quantum dots, with respect to their relative lattice configuration described in section 3.2.1.2.1. Conclusively, the disappearance of the infrared stretching frequencies around the alkyl, C-H frequency region in the spectra of the SnSe(3-MPA) quantum dots at 1393 cm^{-1} and 1166.8 cm^{-1} respectively was related to a defined single crystal lattice rotation mode adopted by the quantum dot nanomaterial with limited chemical bonds dynamism.

3.2.1.5. The surface electrochemical properties of the SnSe(3-MPA) quantum dots.

The surface electrochemical properties of the SnSe(3-MPA) quantum dots were evaluated directly onto the gold electrode surfaces. The surface concentration and dynamic kinetic properties of the SnSe(3-MPA) quantum dots were evaluated using static cyclic and square-wave voltammetry techniques. In cyclic voltammetry (CV), a static 0.1 M phosphate buffer solution of pH 7.4 was used as the supporting electrolyte. Figure 57, presents the cyclic voltammetry profiles of 95 µL/cm^2 SnSe(3-MPA) quantum dot films deposited on a planar gold disk electrode, with the surface area magnitude; 0.021 cm^2 at a fixed potential window between 850 mV to -800 mV, and varied scan rates between 5 mV/s and 70 mV/s.

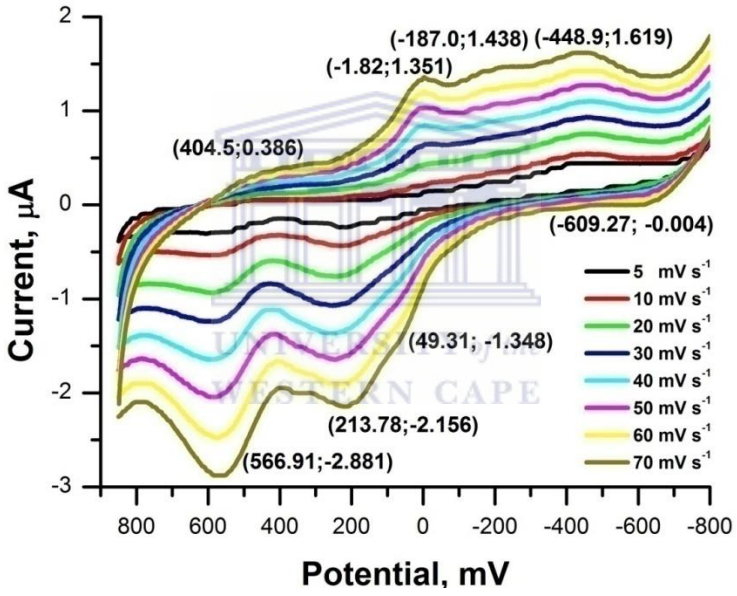

Figure 57: The cyclic voltammetry responses of the SnSe(3-MPA) quantum dots films on a gold electrode substrate at scan rates between 5 mV/s and 70 mV/s in 0.1 M phosphate buffer solution of pH 7.4 at 25 °C**.**

The cyclic voltammetry profiles of the SnSe(3-MPA) quantum dots revealed redox peak potentials at; {E_{pc} ≈ 404.5 mV, -187.0 mV, -448.9 mV and -444.23 mV} and {E_{pa} ≈ -609.3 mV, 49.31 mV, 213.78 mV and 566.91 mV} that were on account of distinct pertinent quadri-centred electroactive SnSe(3-MPA) quantum dots. The proposed different electroactive centres in the SnSe(3-MPA) quantum dots are shown in the illustration; Figure 57, relating the electron transfer properties of the films with their chemical potential.

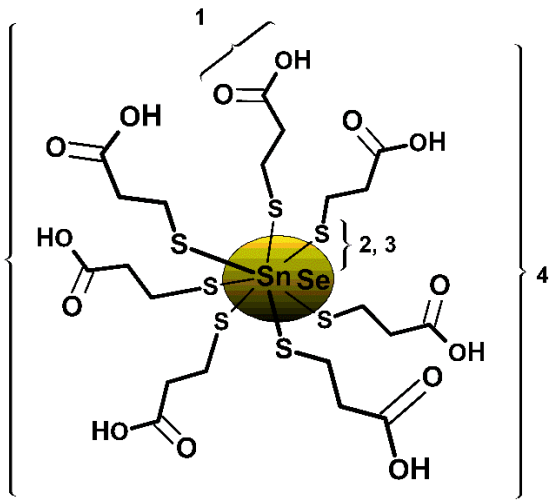

Figure 58: The electroactive functional groups in SnSe(3-MPA) quantum dots (i.e. labelled **1** to **4),** self-assembled on the gold electrode surface.

In Figure 58, illustrated by (**1**) is a liable electro-active carboxylic acid group at the terminus of the 3-mercaptopropionic acid capping on the SnSe(3-MPA) quantum dot surface. At the pH of approximately 7.0, the carboxylic acid groups readily dissociate in water to form redox liable conjugate bases. A liable acid deprotonation reaction of the carboxylic acids of the SnSe(3-MPA) quantum dots is presented in next equation; Equation 15.

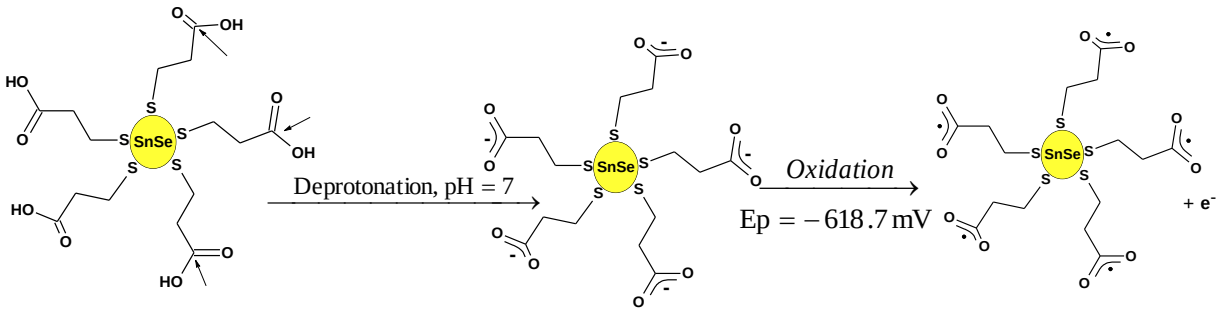

Equation 15

Oxidation of the liable carboxyl acid anionic bases through the electrode potential transferred at the quantum dot electroactive films; deposited on a gold substrate results into a loss of an electron at the anionic carboxylic acid groups as indicated in Equation 15. The electron transfer oxidation reaction at the formal potential; E_{pa} of -618.7 mV observed in the cyclic voltammetry profiles presented in Figure 57 was associated with the oxidation of the carboxylic acid groups of the 3-

mercaptopropionic acid capping on the tin selenide quantum dot surfaces. Furthermore, the 3-mercaptopropionic acid groups are associated with the presence of the deprotonated sulfhydryl group, highlighted bold on the given 3-mercaptopropionic acid structure (i.e. $^{-}$**S**CH_2CH_2COOH) and in Figure 59. The deprotonated-thiol group in the 3-mercapropionic acid is liable to oxidation due to the partial electronegative sulphur anion; its electron valence band is associated with the four pi electrons, and a sigma electron; described in the molecular orbital diagram presented in Figure 59**.**

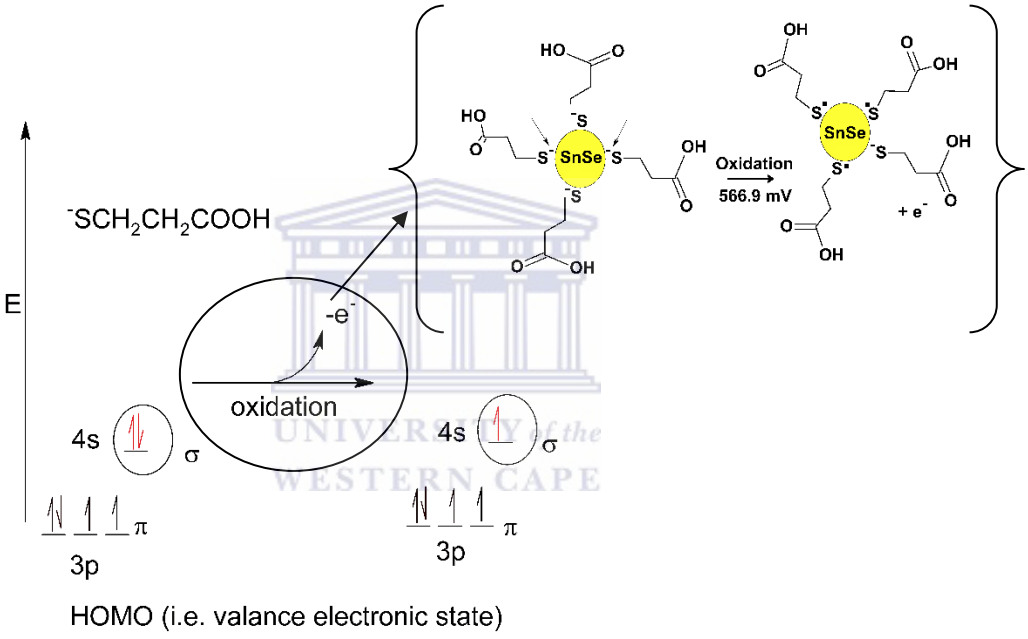

Figure 59: A valence orbital diagram of the deprotonated thiol group of the 3-mercaptopropionic acid capping of the SnSe(3-MPA) quantum dots.

The oxidation peaks observed at; E_p = 557 mV in the cyclic voltammetry profiles presented in Figure 57, were due to the oxidation of the thiol functional groups of the 3-mercaptopropionic acid capping (i.e. $^{-}$S-CH_2CH_2COOH) on the tin selenide quantum dots, through oxidation of the $^{-}$S groups to stable reactive sulphide radicals ($^{\bullet}$S). In semiconductor theory, indirect and direct semiconductors can be created by electron-pair system with free electron dynamism implying electrons freely oscillate and migrate between electronic levels in the effect of a radiated energy

(Smith, 2010). The completely reversible electron transfer reactions observed at; ΔE_p of 211.2 mV in the cyclic voltammetry profiles presented in Figure 57, were associated with the SnSe(3-MPA) quantum dot's exciton oxidation reactions; at E_{pa} = 213.8 mV, coupled to the reduction reactions at E_{pa} = -1.82 mV. These electrochemical transfer reactions were on account of the tin selenide quantum dot, electron rich cores associated with their valance band electronic state. Electrochemical properties of the SnSe(3-MPA) quantum dots were further evaluated through Oyster Young square-wave voltammetry (O-SWV) studies. In the O-SWV studies, the reductive and oxidative potential scans were applied at the potential windows from 800 mV to -800 mV and vice-versa for; the reductive and oxidative scans respectively and highlighted in Figure 60 (**A**) and Figure 60 (**B**) respectively, evaluated at the scan rates between 6 mV/s to 26 mV/s.

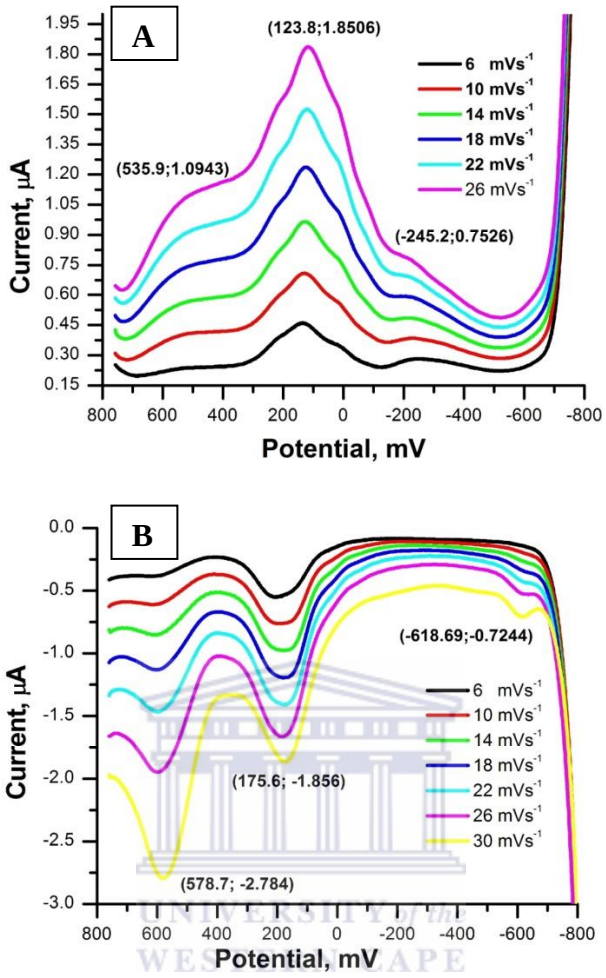

Figure 60: (**A**) The reductive, and (**B**) the oxidative Oyster-Young square-wave voltammetry studies of the SnSe(3-MPA) quantum dots on a gold electrode surface, at scan rates between 6 mV/s and 30 mV/s, in 0.1 M phosphate buffer solution of pH 7.4 at 25 °C.

The electrode formal potential ($E_p^{o'}$) at 123.8 ± 6 mV, observed in the reductive O-SWV studies presented in Figure 60 (**A**), associated with the current magnitude of 0.5 µA, evaluated at 10 mV/s, indicated high redox activity of the SnSe(3-MPA) quantum dot films. Relatively, this redox peak was observed at the formal potential, $E_p^{o'}$ of 173.5 ± 3 mV during the oxidative scan presented by O-SWV profiles of Figure 60 (**B**), (i.e. both values were reported with the standard deviation in the peak potentials). At the scan rates above 6 mV/s, the liable valence electronic state in the SnSe(3-MPA) quantum dots imposed redox activity associated with the oxidation of the $^{-}$S groups at $E_p^{o'}$= 535 ± 2 mV and $E_p^{o'}$ magnitude of 578.7 ± 2 mV for the reductive and oxidative O-SWV studies respectively. This was an indication of an electron hoping between the oscillating energy

valance states of the SnSe(3-MPA) quantum dots core and the energy valance state of the; $^{-}SCH_2CH_2COOH$ (i.e. 3-MPA) capping. The electronic valance energy states of the SnSe(3-MPA) quantum dots are elaborated in the molecular orbital diagram herein presented; in Figure 61.

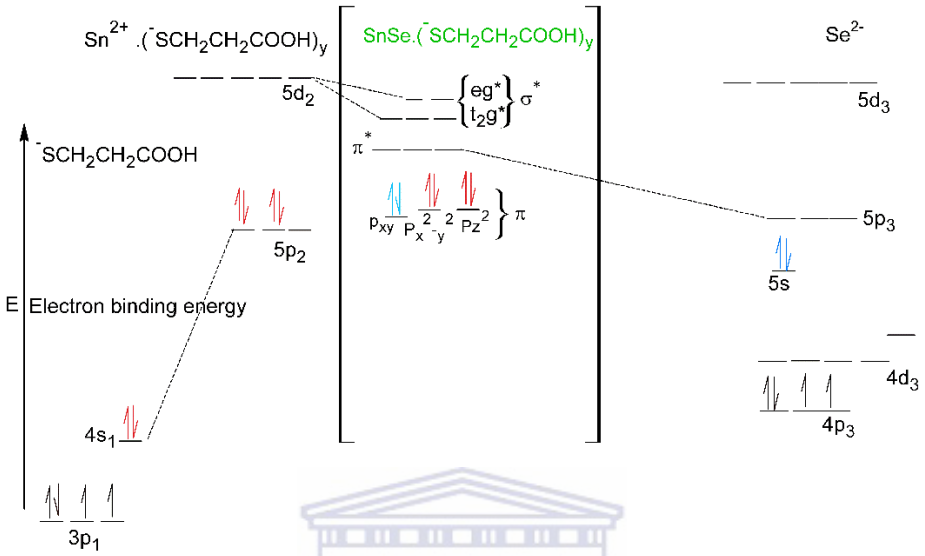

Figure 61: The molecular orbital expansion; illustrating the liable electron transfer valence of the SnSe(3-MPA) quantum dots.

In the O-SWV scan rate studies presented in Figure 60 (**B**), the distinct oxidation peak at $E_p{}^{o'}$ -618.7 mV, which was uniquely observed during the oxidative scan in was the resultant of the irreversible reduction of the carboxylic acid derivatives of the 3-mercaptopropionic acid capping on the SnSe(3-MPA) quantum dots. Furthermore the surface electrochemical kinetic properties of the directly surface adhered SnSe(3-MPA) quantum dots were determined. The surface adsorption equation describes the relation between the electron transfer velocities with the electrochemical current sensitivity on account of the surface adsorption properties by the conducting and semiconducting materials, of the reversible and the quasi-reversible electrochemical systems. Surface concentration (Γ) was evaluated through the herein outlined equation (Fotouhi, Fatollahzadeh et al. 2012).

$$i_p = \frac{n^2 F^2 A}{4RT} \Gamma v$$

Equation 16

In the surface concentration equation presented by Equation 16, the parameter; i_p represents the peak current magnitude, n is the number of electrons transferred in an electrochemical reaction. For a reversible system, the number of electrons can be estimated from the electrochemical peak potential difference; $\Delta E_p = \frac{60}{n} mV$ (i.e. where $\Delta E_p = E_{pc} - E_{pa}$, and the parameters; E_{pc} and E_{pa} represents the cathodic and anodic peak potentials respectively), F is the Faradays constant, A is the geometric area of an electroactive substrate or surface. The parameter R is the Universal gas constant, T represents the absolute temperature in Kelvins and v is the magnitude of the scan rates. The surface concentration (Γ) of adsorption can be estimated from the linear correlation coefficient and the slope of i_p vs v linear plots of both the reduction or the oxidation electrochemical reactions. The surface concentration dependence with the slope of the linear plot of; i_p vs v is herein presented in the next equation; Equation 17.

$$\Gamma = \frac{Slope}{nFA} RT$$

Equation 17

The electrochemical redox reaction at ΔE_p = 211.9 mV, evaluated from the cyclic voltammetry studies of the SnSe(3-MPA) quantum dot films was diagnosed to be a completely reversible surface adsorption-controlled redox electron transfer reaction, associated with the oxidation to reduction peak ratio (i.e. i_{pa}/i_{pc}) of 0.84. The SnSe(3-MPA) quantum dots were associated with the surface concentration (Γ) of 1.035×10^{-4} mol/cm^2. Nevertheless, a surface concentration Γ; of 1.46×10^{-4} mol/cm^2 was obtained at the potential difference; ΔE_p of -627.1 mV; associated with the oxidation of the carboxylic acid derivatives on the 3-mercaptopropionic acid molecules on the SnSe(3-MPA) quantum dot capping. The surface concentration values related to the oxidation of the carboxylic acids on the quantum dots, 3-MPA capping deviated with the magnitude of ± 0.011 µmol/cm^2 , compared to the surface concentration values that were obtained at the redox electron transfer at ΔE_p = 211.9 mV, associated with the SnSe(3-MPA) quantum dot core. This was related

to the larger electrochemical surface area of the semiconducting SnSe quantum dot-core compared to the electrochemical active surface area of the 3-mercaptopropionic acid capping on the quantum dot surface. Relatively, highly sensitive electron-transfer current responses of the quantum dot films was obtained when the SnSe(3-MPA) semiconducting quantum dot films were studied using Oyster-Young square-wave voltammetry (i.e. evaluated at the formal potential $E_p^{o'}$ of 123.5 mV associated with the redox electron transfer in the SnSe quantum dot core valence). A surface concentration; Γ of 3.43×10^{-4} mol/cm^{-2} was obtained, evaluated at i_p vs v, linear regression plots associated with the correlation coefficient $r^2 = 0.991 \pm 0.025$. Electrochemical properties of the SnSe(3-MPA) quantum dots were further classified by the kinetic function, diffusion co-efficient (D_o^*), determined from the Randle-Sevcik approximation (Neghmouche and Lanez 2013) highlighted in Equation 18.

$$i_p = 0.446nFAC^* \left[\frac{nFDv}{RT} \right]^{1/2}$$

Equation 18

In Equation 18, peak currents (i_p) represent the cathodic or anodic peak currents, (C^*) is concentration of the bulk solution (i.e. 0.1 mol/dm^3), n, F, A, R, T were defined in the previous surface concentration expression in Equation 16. The direct surface adsorbed, SnSe(3-MPA) quantum dots were associated with the diffusion co-efficient; (D_o^*) of 9.88×10^{-15} cm^2/s. The dynamic kinetic properties of the thin SnSe(3-MPA) quantum dot films were further characterized by Stokes-Einstein Sutherland expression relating the diffusion kinetic character of the quantum dot films with the dynamic viscosity of the films, expressed in the next equation; Equation 19 (Sharma and Yashonath 2007).

$$\eta^* = \frac{K_B T}{6\Pi r_{solute} D_0^*}$$

Equation 19

The parameter (K_B) defines Boltzmann's constant, (T) is the absolute temperature, and (r_{solute}) is the radius of the solute. The viscosity (η^*) of the electroactive SnSe(3-MPA) quantum dots

films modified on the gold surface was determined to be 4.59 x10^{-13} kg/ms. The SnSe(3-MPA) quantum dots electrochemical properties are summarized in the next table; Table 7.

Table 7: The electrochemical properties of the SnSe(3-MPA) quantum dots.

Potential difference, ΔE_p (in mV)	ΔE_p = 215.6 , $\Delta E_p/n > 100$ and the number of electrons was determined to be 3
Surface concentration, Γ (in mol/cm^2)	1.035 x10^{-5}
Diffusion Co-efficient, D_0 (in cm^2/s)	9.88 x10^{-15}
Dynamic Viscosity, η (in kg/ms)	4.59 x10^{-13}

Chapter 4 The development of the estrogen receptor alpha (ER-α) based biosensor for 17β-estradiol

This research project emerged through a notion of providing an advanced technology to already existing lab-on analysis techniques designated for determining concentration levels of an estrogenic endocrine disrupting compound (e-EDC); 17β-estradiol (E2), that would offer ultimately; specific, sensitive, and stable novel biosensor microchips to detect this compound at micro to nano-molarity concentration arrays. Estrogenic endocrine disrupting compounds had been attested to threshold the ecosystem through domestic wastewater discharges and river runoffs (Campbell, Boglin et al. 2006, Chen, Kuo et al. 2009). Although the endocrine system is replete with metabolic pathways associated with a series of glands and organs responding to the catabolism and detoxification of active drugs, biological contaminants and other active chemicals or compounds, the approximate level of their complete decomposition is vastly compromised. Thus, a percentage proportion of these estrogens are released unaltered and imposed into a secondary life cycle. In this research, the interdisciplinary chemical, physical, and analytical properties of the bio-receptor {i.e. estrogen receptor alpha (ER-α} and the intermediate quantum dot nanomaterials delivered a constructive role in the development of the 17β-estradiol biosensor microchips, these biomaterials' properties were fully described in Chapter 2 and Chapter 3 respectively. The development of the biosensor system critically involved electrochemical studies of the various reaction mechanisms associated with substrate-specific estrogen receptor alpha's (ER-α's) electrochemical affinity capabilities towards the target analyte; 17β-estradiol compound that are related to the concentration capacity of the 17β-estradiol present. Figure 62, shows the strategy to development of the ER-α/SnSe(3-MPA)/L-cysteine/AuE biosensors for 17β-estradiol.

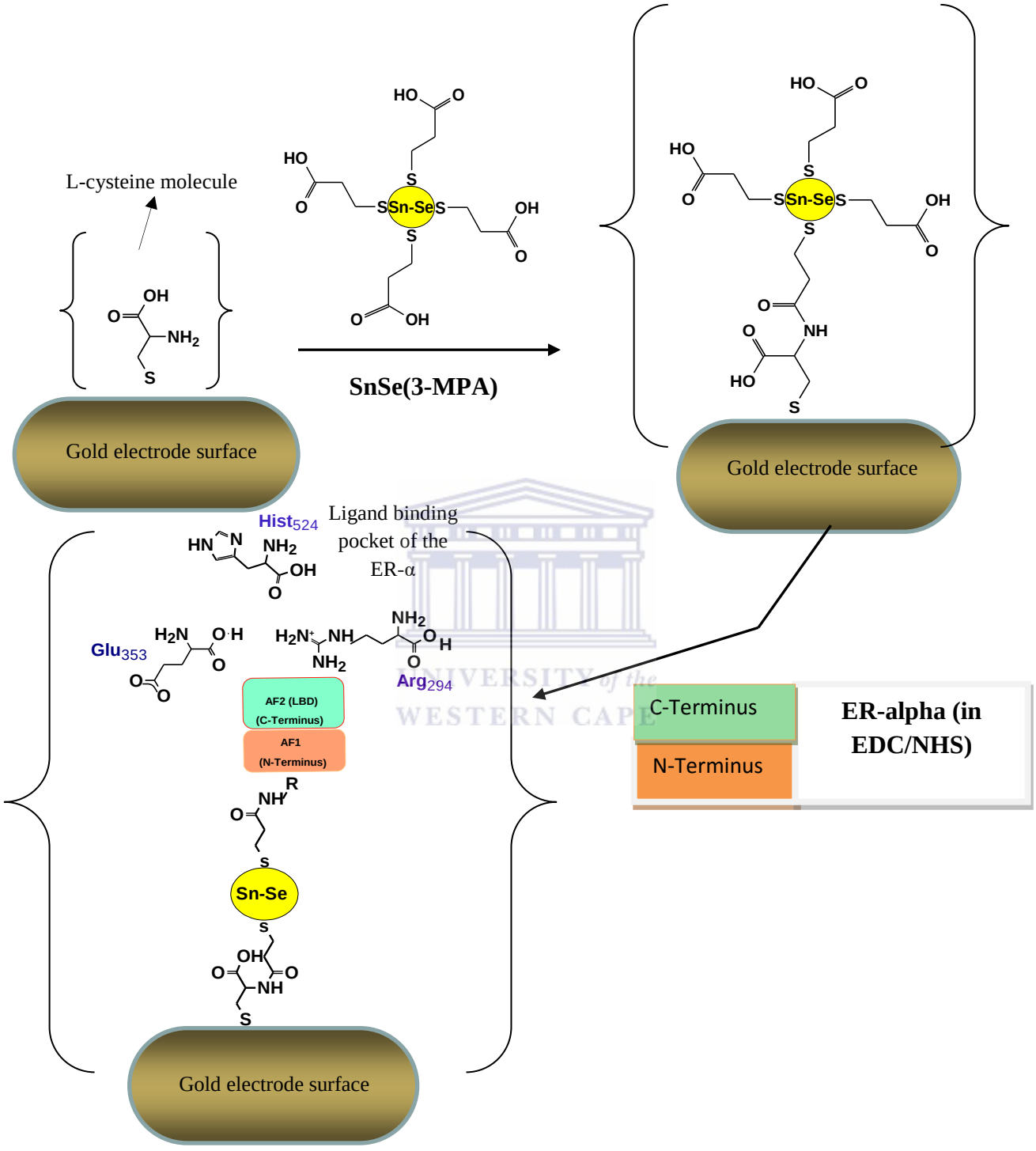

Figure 62: The surface configuration of the ER-α/SnSe(3-MPA)/L-cysteine/AuE biosensor electrode.

The next section, section 4.1 describes the electrochemical activity of the intermediate electroactive films present at the biosensor sensing surface towards the analyte; 17β-estradiol.

4.1. Electrochemical bio-reactivity of the different modified electrode surfaces.

The biosensing electrodes were prepared through surface modification of the gold electrodes with different materials or films used to enhance the electrochemical bio-reactivity of the gold electrode surfaces and to shield the bio-receptor {i.e. estrogen receptor alpha; ER-α} from the electrostatic degradation. The chemical potential, electrochemical reactivity and the dynamic kinetic properties of the intermediate electrode surfaces towards the 17β-estradiol were also reconnoitred and described in sections; 4.1.1 to 4.1.3.

Chemicals

All chemicals used in this study were of analytical grade and purchased from Sigma Aldrich and Fluka respectively. Absolute ethanol, sodium dihydrogen phosphate, disodium hydrogen phosphate, 17β-estradiol (E2), L-cysteine (L-Cys), cysteamine, N-hydroxysuccinimide (NHS), 1-ethyl-3-(3-dimethylaminopropyl) carbodiimide (EDC) and ethyl diaminetetraacetic acid (EDTA) were all purchased from Sigma Aldrich. A 50 % glycerol solution, tri-acetate buffer of pH 7.4 and absolute ethanol were purchased from Fluka. The 0.1 M phosphate buffer solutions (PBS) of pH 7.4 were prepared from sodium dihydrogen phosphate and disodium hydrogen phosphate in double distilled water filtered by Ris millipore ^{TM} filtering system. The 0.001 M 17β-estradiol standard solutions were prepared by dissolving, the 17β-estradiol in a mixture of 99 % absolute ethanol and purified distilled water in a 25 % to 75 % ratio respectively.

Instrumentation

All electrochemical experiments were carried out using a BAS 100W cell integrated and automated electrochemical work station {i.e. from Bioanalytical Systems Incorporated (BASi), West Lafayette, USA}. A 10 mL electrochemical cell with a conventional three electrode set up was used. The electrodes used for the electrochemical analysis were: (1) the gold working electrode with a geometric area of 0.0201 cm^2, and (2) the Ag/AgCl (3 M NaCl) electrode used as a reference electrode, purchased from BASi. A third electrode (i.e 3rd) was the platinum wire that was employed as a counter electrode and was purchased from Sigma Aldrich. Alumina micro-polish

powders of different particle sizes ranging from (i.e. 0.05 to 1) μm and 12" micro-cloths (i.e. purchased from Buehler of Illinois, USA) were used for polishing the working electrode surfaces.

4.1.1. Preparation of the L-cysteine monolayers onto the gold electrode surfaces.

The L-cysteine (L-Cys) thin films were prepared by submersing the gold electrode surfaces into 0.01 M L-cysteine solutions for 8 h under 0 % UV-light illumination (i.e. in the dark). The thiol derived molecules are usually employed to adhere micro molecules onto the electrode surfaces for bio-analysis and other modified surface application such as; wetting, corrosion protection and sensor development (Bulgariu and Bulgariu 2008, Zhuang, Hansen et al. 2009). The gold surfaces are susceptible to formation of the covalent thiol-linked L-cysteine monolayers, this is as a result of thiol (S-H) having great affinity for metal surfaces. A gold surface is suitable for covalent bonding with a thiol derivative; L-cysteine molecule due to a lone electron on its valence. The cyclic voltammerty profiles of the; bare and L-Cys functionalised gold electrode surfaces at a potential window between -800 mV to 600 mV and scan rates from 10 mV/s to 100 mV/s in a 0.1 M phosphate buffer solution of pH 7.4 are presented in Figure 63 (**A**) and Figure 63 (**B**), respectively.

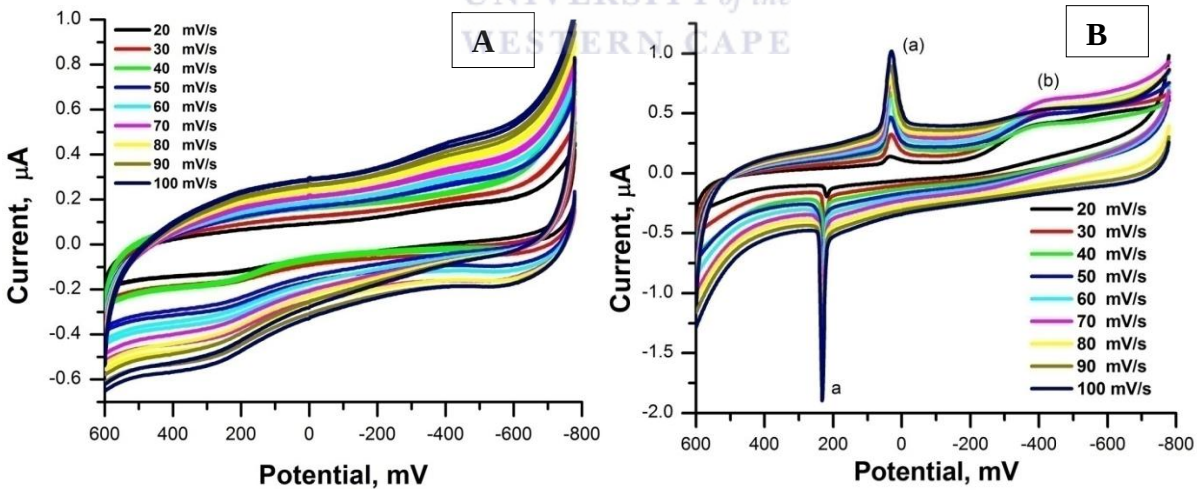

Figure 63: The cyclic voltammetry profiles of; (**A**) the bare gold electrode surface and (**B**) the L-cysteine modified gold electrode at scan rates between; 20 mV/s to 100 mV/s, in a 0.1 M phosphate buffer solution of pH 7.4 at 25 °C.

In the cyclic voltammetry studies of the bare gold electrode surfaces, no distinguished electrochemical redox electron transfer related peaks were notable, this indicated non-electron conducting character of the gold electrode surfaces at the predefined electrochemical potential window and phosphate buffer supporting electrolyte conditions. A deposited thin monolayer of L-Cys onto the gold electrode resulted into the formation of a redox electro-active monolayer onto the gold electrode surface, associated with two distinct redox electrochemical activities, at a reversible redox potential difference, ΔE_p of 201.01 mV {i.e. the redox electrochemical reaction; a/(a) in Figure 63 **(B)**}. An irreversible reduction electron transfer reaction was also noted at (b) of Figure 63 **(B)** at a reduction potential, E_{pc} of -423.2 mV. The L-cysteine consists of two distinct redox liable; amine and carboxylic centres, as outlined in a proposed chemical synapse in the next figure; Figure 64.

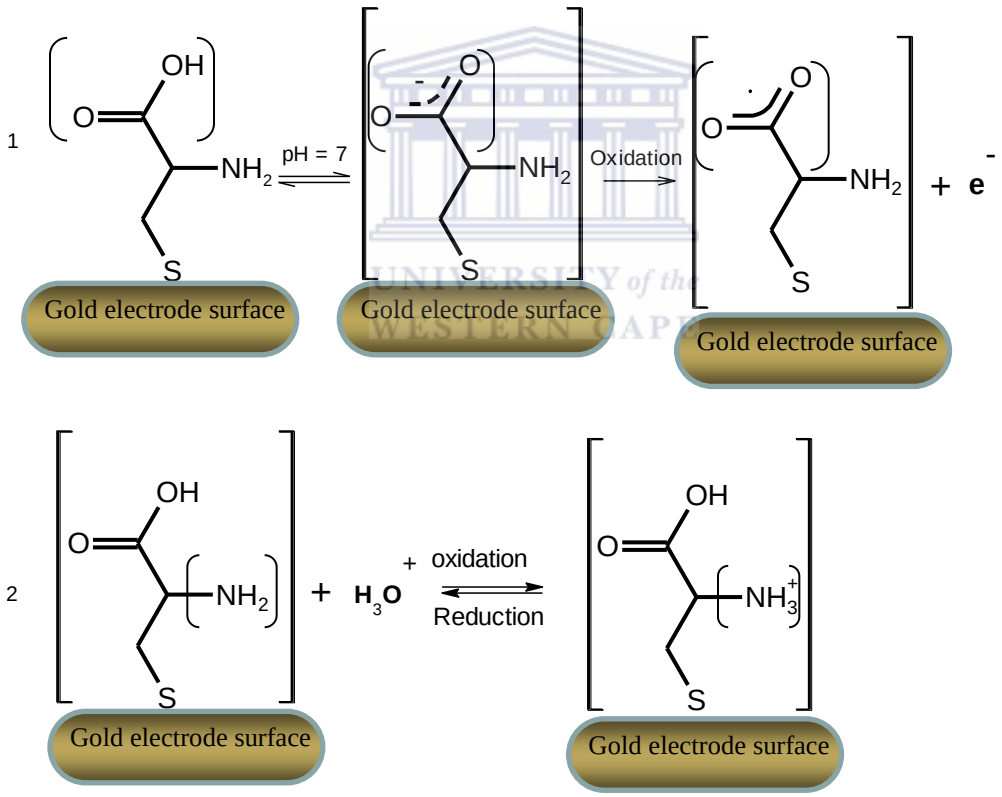

Figure 64: Chemical active functional groups in L-cysteine films deposited on a gold electrode surface.

The oxidation of the carboxylic acid group derivatives occur at potentials between the $E_p^{o'}$ = -600 ± 50 mV and were discussed in the section 3.2.1.5. The reduction of a carboxylic acid functional

group of the L-Cys self-assembled monolayer on the gold electrode surface involves a multi-step loss of an electron at a carboxyl-anion moiety, resulting into a free carboxylic acid radical highlighted in an electrode reaction **1** of Figure 64. In the proposed electron transfer reaction of the amine group of the L-Cys highlighted in reaction **2** of Figure 64, the amine functional group acts as an acid. It is liable to a reversible electron transfer conversion; from the secondary NH_2 to the primarily cationic NH_3^+ acid (i.e. the NH_2/NH_3^+ redox reaction) and was associated with the redox electron transfer reaction at, ΔE_p of 201 mV.

4.1.2. Preparation of the 3-mercaptopropionic acid capped tin selenide quantum dots functionalised L-cysteine modified gold electrode surfaces.

The L-cysteine/AuE functionalised gold electrode surfaces were immersed into solutions of 3-mercaptopropionic acid capped tin selenide quantum dots in the presence of 0.01 M 1-ethyl-3-(3-dimethylaminopropyl) carbodiimide (EDC) and 0.005 N-hydroxysuccinimide (NHS) reagents in the molar ratio of (1:2) at 25 °C to form the SnSe(3-MPA)/L-cysteine modified gold electrode surfaces. The quantum dots; L-cysteine functionalised surfaces were then washed more than two times in order to remove the unreacted residues of the unreacted SnSe(3-MPA) quantum dots onto the electrode surfaces. The susceptible condensation reaction coupled to dehydration reaction, between the amine groups (i.e. NH_2) of the L-cysteine and the carboxyl groups (i.e. COOH) of the capping on the SnSe(3-MPA) quantum dot resulted into the formation of a strong amide bond {i.e. R_1HN-C(CO)-R_2, where R_1 and R_2 represent the backbones of the L-cysteine and the SnSe(3-MPA(s) quantum dots, respectively}. This resulted into a fairly strong and stable linkage between the semiconducting quantum dot films and the L-cysteine modified gold electrode surfaces (Tengvall, Jansson et al. 2003, Eric and Mark 2009). A cyclic voltammetry electrode potential window between -800 mV and 600 mV at scan rates from 20 mV/s to 140 mV/s was studied in order to evaluate the surface electrochemical properties of the SnSe(3-MPA) quantum dot/L-cysteine modified gold electrode surfaces in 0.1 M phosphate buffer solution of pH 7.4. The cyclic voltammetry profiles are presented in Figure 65.

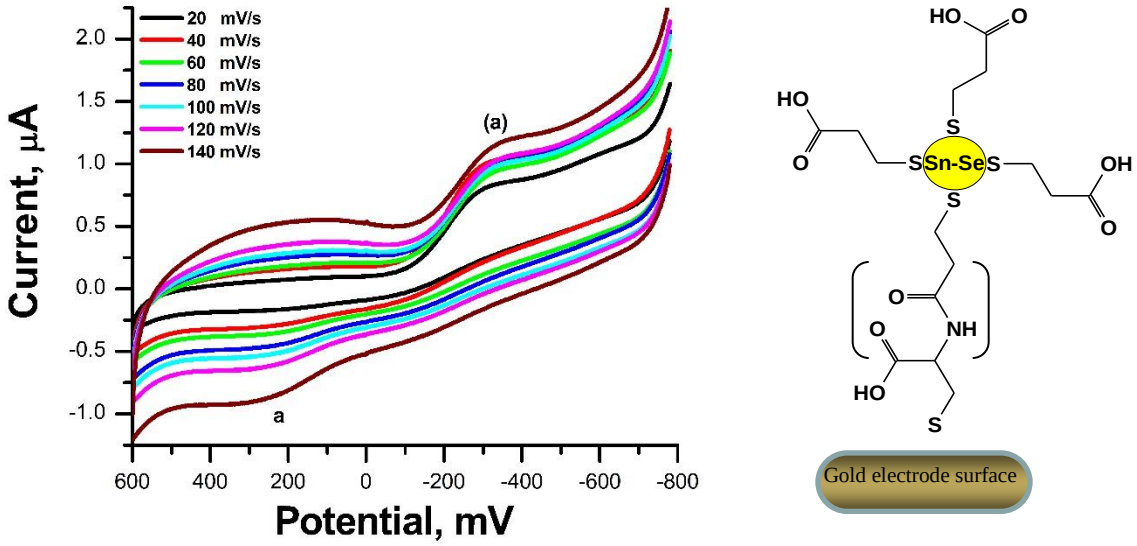

Figure 65: The cyclic voltammetry responses of the SnSe(3-MPA)/L-cysteine films immobilised onto the gold electrode surface.

Cyclic voltammetry profiles of the SnSe(3-MPA)/L-cysteine films immobilised on a gold electrode surface exhibited; oxidation peaks, E_{pa} (s) at 263 mV and a reduction peaks, E_{pc} (s) at -338 mV labelled **a** and **(a)** respectively, in Figure 65. The slight oxidation at **a** was associated with an amide bond oxidation {i.e. $[R_1HN\text{-}C(CO)\text{-}R_2]$ / $[R_1HN\text{-}C(CO)\text{-}R_2]^+$}. The absence of the redox electron transfer reaction at a potential difference; ΔE_p of 201 mV indicated restriction of a reversible amine conversion reaction (i.e. NH_2/NH_3^+) on the L-cysteine molecule, as it was observed in the case of cyclic voltammetry studies of the unmodified L-cysteine monolayers, described in section 4.1.1. The observed electrochemical behaviour was a consequence of inaccessibility of the free secondary amine groups of the L-cysteine molecule to initiate any electrochemical effect, due their involvement in the amidation reaction with the carboxylic groups of the SnSe(3MPA) quantum dots capping. The redox electron transfer reaction of the secondary amines observed in the cyclic voltamogrammes of the L-cysteine at the peak potential difference, ΔE_p of 201 mV, were further supported by performing the electrochemical scan rate studies of the cysteamine self-assembled monolayer at the same potential window. A cyteamine molecule consists of only, free amine groups but not carboxylic acid functional groups. The cyclic voltammetry responses of the cysteamine modified gold electrode surfaces at different scan rates were described in Figure 83 in the appendix section of this thesis. Comparison studies of the

surface electrochemical properties of different electrode materials are highlighted in a table presented at the end of this section.

4.1.3. Preparation of the ER-α/SnSe(3-MPA)/L-cysteine functionalised gold electrode surfaces (i.e. the estrogen receptor-α based biosensors for 17β-estradiol)

The estrogen receptor alpha (ER-α) was introduced onto the surface; SnSe(3-MPA)/L-cysteine/AuE pre-activated with EDC/NHS by drop injection of 0.1 µL ER-α solution (i.e. stabilized in the constituents of; 20 % glycerol, 50 mM tris-acetate buffer and 1 mM EDTA, at a pH 7.4). The ER-α was allowed to inter-link and adopt a stable structural conformation onto the functionalized electrode surface for 2 h at approximately 4 °C. This was associated with the activation of the electroactive functional groups present on the estrogen receptor alpha (ER-α), where distinct electrochemical redox reactions were observed. The surface activation of the ER-α/SnSe(3-MPA)/L-cysteine/AuE modified gold electrode at the predefined temperature, is presented through cyclic voltommogrames highlighted in the next figures; Figure 66 **(A)** and Figure 66 **(B)**.

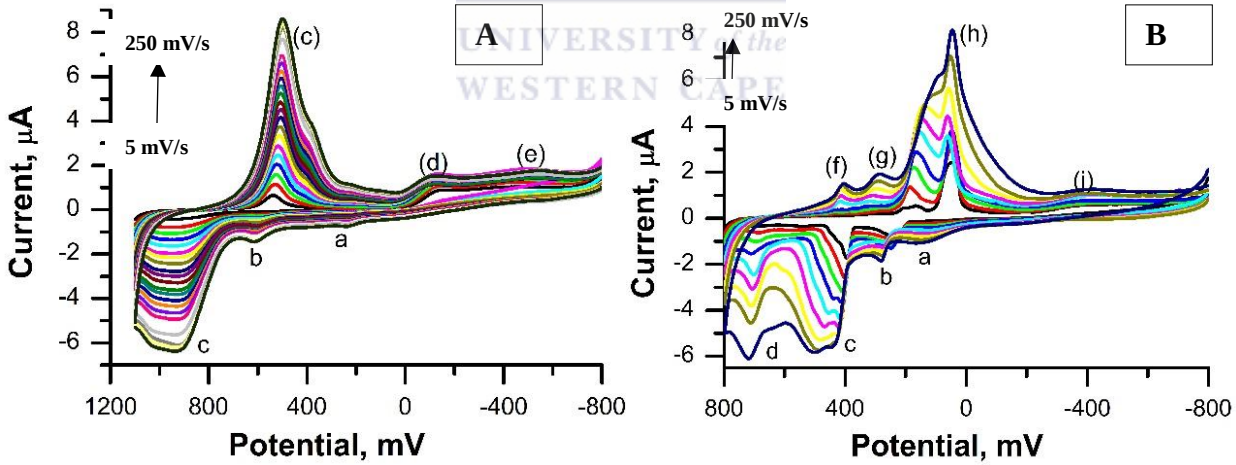

Figure 66: The cyclic voltammetry profiles of the biosensor; **(A)** before and **(B)** after subjecting the surfaces to 4 °C in 0.1 M phosphate buffer solution, of pH 7.4 at 25 °C.

The cyclic voltammetry studies in Figure 66, demonstrate the ER-α/SnSe(3-MPA)/L-cystein/AuE electrochemical surface analysis at different scan rates from 5 mV/s to 250 mV/s. The activation of the electroactive groups in the ER-α were observed at both the oxidation and reduction potentials. Distinct electrochemical oxidation reactions at; **a** (a/a^+), **b** (i.e. b/b^+) and **d** (i.e. d/d^+)

corresponding to the oxidation potential magnitudes, E_{pa} (s) of; 137 mV, 278 mV and 727 mV, respectively were observed {i.e. in Figure 66 (**B)**}. This was accompanied by a vast potential shift from 789 mV to 950 mV related to the full oxidisation of the phosphates at the gold electrode surfaces at the split peak labelled, **c** (i.e. c/c^{+}) in both Figure 66 **(A)** and Figure 66 **(B)**. The oxidation of the phosphate groups at the gold electrode surface are usually observed between (500 – 900) mV. The electrochemical activity of the ER-α/SnSe(3-MPA)/L-cysteine/AuE biosensor was then evaluated at the electrode potential window between -800 mV and 800 mV, at different scan rates from 20 mV/s to 120 mV/s in 0.1 M phosphate buffer of pH 7.4, the voltammetry profiles are presented in Figure 68.

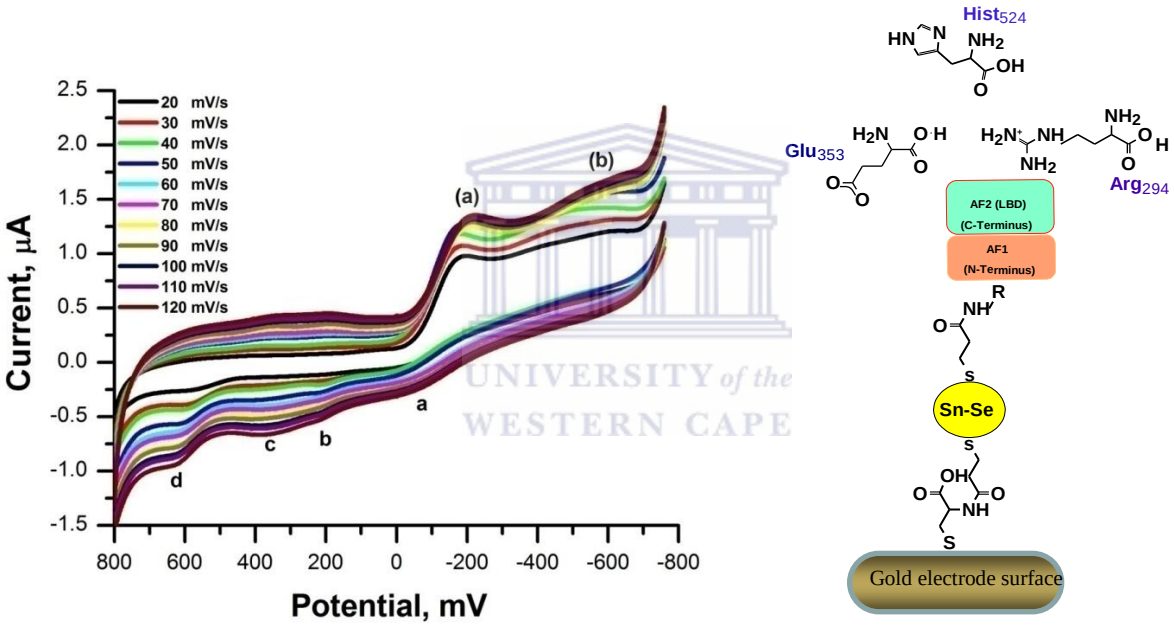

Figure 67: The cyclic voltammetry responses of the ER-α/SnSe(3-MPA)/L-cysteine films deposited on the gold electrode surface, in 0.1 M phosphate buffer solution of pH 7.4 at 25 °C.

The cyclic voltammetry profiles of the ER-α/SnSe(3-MPA)/L-cysteine/AuE biosensor revealed four oxidation peaks labelled; **a**, **b**, **c**, and **d**, in Figure 65 corresponding to the oxidation peak potentials; E_{pa} at approximately;-62.8 mV, 215.4 mV , 376.0 mV and 627.2 mV respectively. The reduction peak potentials were comparable observed at E_{pc} (s) of approximately; **(a)** -209 mV and **(b)** -582.6 mV. This was an implication of electro-active redox liable species in the ER-α/SnSe(3-

MPA)/L-cysteine/AuE biosensor surface. The EDC/NHS coupling and the immobilization of the amine-terminated ER-α biomolecule onto the carboxyl acid-terminated SnSe(3-MPA) quantum dots immobilised on the AuE/L-cysteine electrode is illustrated in Figure 68.

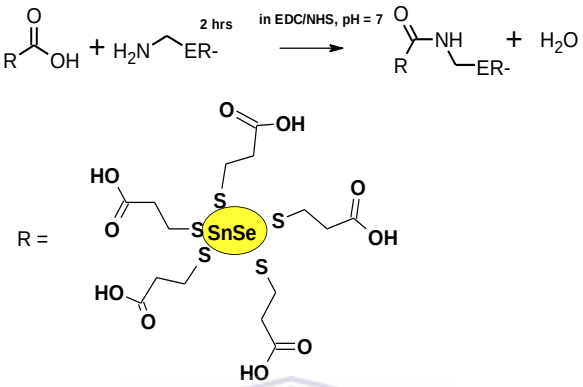

Figure 68: The EDC/NHS coupling reaction between the amine functional groups present in the ER-α; amino acid sequence structure and the carboxyl acid functional groups of the 3-mercaptopropionic acid capping on the SnSe(3-MPA) quantum dots.

The following table describes the different electrochemical properties of the different electrode materials and their electrochemical reactivity in the presence of the 17β-estradiol analyte.

Table 8: The 17β-estradiol's reactivity of different electrode surfaces.

Electrode surface components	**Surface concentration (mol/cm$^{2)}$**	**Dynamic linear range (µM)**	**Detection limit (M)**
Bare gold electrode surface (i.e. electrostatic reduction of the 17β-estradiol at E_{pc} of -440 mV)	-	0.6 - 0.6 (i.e. single concentration measurement)	-
L-cysteine/AuE (i.e. reversible catalytic conversion reaction at ΔE_p= 196 mV and un-specific reduction at E_{pc} -404 mV)	7.07×10^{-10}	0.6 - 0.6 (i.e. single concentration measurement)	-
SnSe(3-MPA)/L-cysteine/AuE (i.e. no electrochemical activity was observed)	1.55×10^{-9}	-	-
ER-α/SnSe(3-MPA)/L-cysteine/AuE (i.e. an oxidation reaction at E_{pa} = 198 mV and an irreversible reduction at E_{pc} = -695 mV)	1.76×10^{-10}	0.25 – 1.25	0.2

The method of detection used for the above reported studies was cyclic voltammetry. The voltammetry profiles representing the electrochemical detection of different 17β-estradiol concentrations using the bare and the L-cysteine modified gold electrode surfaces are reported Chapter 8, in the appendix section of this presented thesis.

4.1.3.1. The electrochemical properties of the estrogen receptor –α based biosensor for 17β-estradiol.

This chapter's section is designated to evaluate the electrochemical activity of the estrogen receptor-α based biosensor and its electron transport mechanisms through the Oyster-Young square-wave voltammetry (i.e. O-SWV) studies, a more sensitive potentiometric method (Bard and Faulkner 2001). Square-wave voltammetry is useful in studies involving micro to nano induced electrochemical signals as a result of slight-surface specific induced concentration changes or the electrolyte solution phase related to the presence of marginally electro-active materials. The surface kinetic properties and electrode activity of the ER-α/SnSe(3-MPA)/L-cysteine/AuE biosensor were evaluated through the Oyster-Young square-wave voltammetry studies at potential windows between -800 mV and 800 mV in 0.1 M phosphate buffer solutions of pH 7.4. Figure 69 **(A)** and Figure 69 **(B)**, represent the reduction and oxidation square-wave voltammetry studies, respectively of the ER-α/SnSe(3-MPA)/L-cysteine/AuE biosensor at different scan rates from 5 to 100 mV/s in 0.1 M phosphate buffer solution.

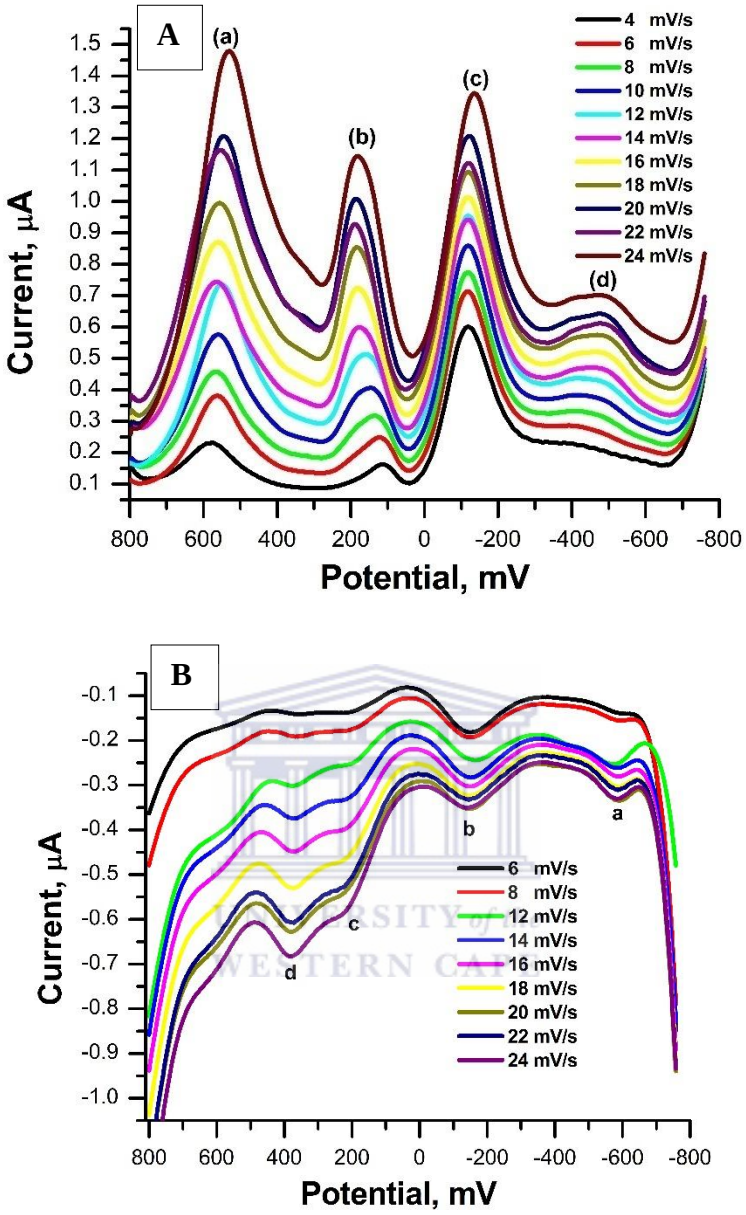

Figure 69: (A) The reduction and **(B)** the oxidation scan, O-square-wave voltammetry responses of the ER-α/SnSe(3-MPA) /L-cysteine films on a gold electrode substrate at scan rates between 4 mV/s and 24 mV/s in 0.1 M phosphate buffer solution of pH 7.4 at 25 °C.

Square-wave voltammetry studies of the ER-α/SnSe(3-MPA)/L-cysteine/AuE (i.e. estrogen receptor-α based biosensor) highlighted in Figure 69 **(A),** representing the reductive scan revealed, four distinct peaks at formal potentials; $E_p^{o'}$ (s) of: 527.9 mV, 181.603 mV, -135.7 mV and -477.97 mV at (a), (b), (c) and (d) respectively. These observed peaks corresponding to liable reducible

and oxidise-able species present at the biosensor surfaces at the electrode's diffusion layer in contact with the phosphate buffer solution. The redox activity in the reductive and oxidative scan were identical, wherein during an oxidative scan, four distinct peaks were evaluated at the formal potential magnitudes, $E_p^{o'}$ (s) of; 504.6 mV, 168.2 mV, -163.41 mV and -528.55 mV (i.e. in highlighted in Figure 69(**B)).** Relatively corresponding to the oxidation half reactions: **{(a)** (i.e. a/a^+), **b** (i.e. b/b^+), **c** (i.e. c/c^+) and **d** (i.e. d/d^+)}. These electron transfer reactions observed in the reductive and oxidative square-wave voltammetry profiles of the estrogen receptor-α based biosensors were not only on account of the high redox activity of the ER-α biomolecule immobilized on the biosensor surface. They were due to the amine conversion oxidation (i.e. NH_2/NH_3^+), the sulphide group oxidation {i.e. $^-$[**S**-R]/$^+$[S-R], where R is the quantum dot backbone}, the carboxylic acid electro-active group's oxidation, and the SnSe(3-MPA) quantum dots; intermediate biosensor component material's redox electron transfer reactions. A biosensor sensitivity of 0.4 µA/mV was evaluated through the oxidation formal potentials, $E_p^{o'}$ (s) at 210.0 mV, evaluated to be the stable oxidation peak that was associated with catalytic conversion of 17β-estradiol by the biosensor surface. Reductive and oxidative square-wave voltammetry studies were further employed to examine the substrate electrochemical activity of the estrogen receptor-α based biosensor towards the analyte 17β-estradiol in a 0.1 M phosphate buffer supporting electrolyte solution at pH 7.4. A potential window between 800 mV and -800 mV for these particular studies was interrogated at the scan rates between 4 mV/s to 26 mV/s, the reduction and oxidation, O-square wave voltammetry studies are highlighted in Figure 70 **(A)** and Figure 70 **(B)** respectively.

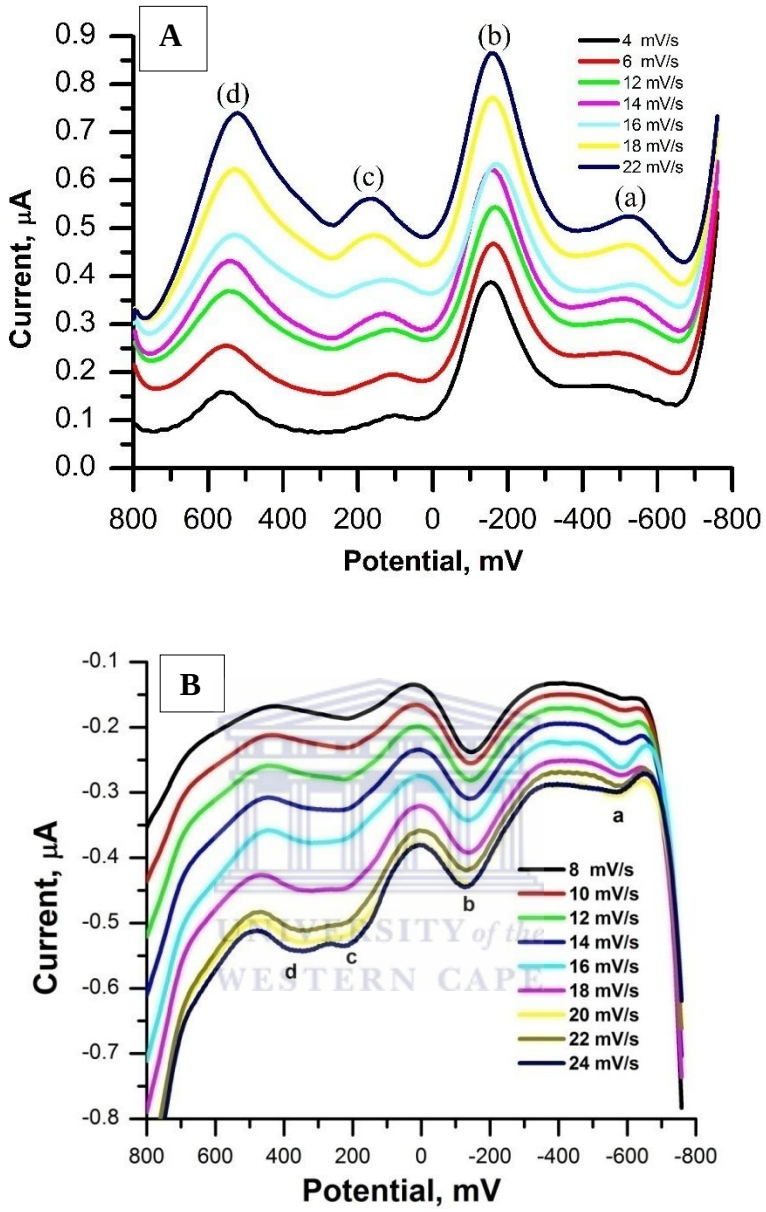

Figure 70: The (**A)** reduction and (**B**) oxidation O-square-wave voltammetry responses of the ER-α/SnSe(3-MPA)/L-cysteine films, on the gold electrode surface at scan rates between 4 mV/s and 26 mV/s in 0.1 M phosphate buffer solution of pH 7.4 at 25 °C and 2 nM 17β-estradiol solution.

The reduction and oxidation square-wave voltammetry profiles of the ER-α/SnSe(3-MPA)/L-cysteine films on the gold electrode surface in the presence of 2.0 nM 17β-estradiol revealed four formal potential peaks. The formal peaks, $E_p^{o'}$ (s) at; a. -578 ± 2 mV, b. -130 ± 2 mV, c. 220 mV and 370 ± 2 mV with peak currents magnitude proportional to an increase in the scan rates. The

redox transfer reactions obtained for the ER-α/SnSe(3-MPA)/L-cysteine/AuE surfaces, in the presence of 17β-estradiol were identical to the redox transfer reactions; **a**, **b**, **c**, (i.e. and can be clearly distinguished in the SVW voltammetry studies presented in Figure 71, at 30 mV/s). Nevertheless, the redox transfer reaction at **d**, completely dissociated after a spike concentration of 2 nM 17β-estradiol. Furthermore, when 2.0 nM of 17β-estradiol was introduced into the electrolyte 0.1 M phosphate buffer solution by spike injection, a distinguished electrochemical peak potential displacement was observed at **b** (i.e. b/b^{+}), where a formal potential redox peak, $E_p^{o'}$ at 181.60 mV was reductively displaced to a formal peak potential $E_p^{o'}$ of 68.2 mV, amplified in next figure, Figure 71.

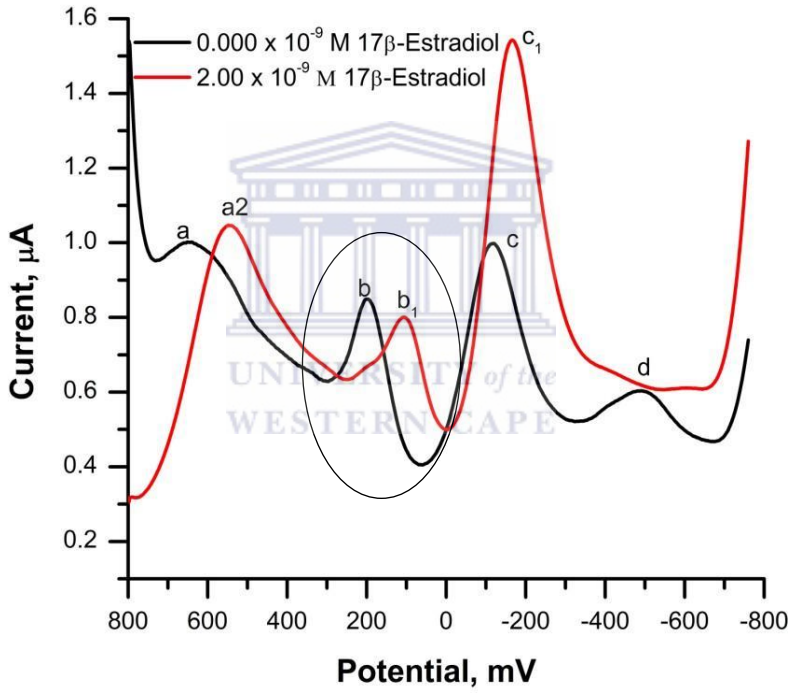

Figure 71: The reduction O-square-wave voltammetry responses of the ER-α/SnSe(3-MPA)/L-cysteine films on the gold electrode surface in the presence of; 0 nM (i.e. **BLACK** voltammogram**)** and 2 nM (i.e. **RED** voltammogram**)** concentrations of 17β-estradiol in 0.1 M phosphate buffer solution of pH 7.4 at a scan rates of 30 mV/s.

A decrease in the peak current response corresponding to a spike concentration of 2 nM of 17β-estradiol was observed at the peak labelled **a** (i.e. a/a^{+}), with a relative formal potential peak shift from 646 mV to a formal potential peak, $E_p^{o'}$ magnitude of 544 mV. Relatively, a reductive

potential shift was observed at **c (**i.e. c/c^{-}), where a decrease in the current magnitude by 0.6 µA folds was followed by a reductive formal potential shift from -120 mV to -166 mV. The sensitivity of the biosensor film estimated in the presence 2 nM of the 17β-estradiol analyte was determined to be 0.3 µA/mV implicating a loss of electrochemical activity of the ER-α immobilized on biosensor film upon association with the limited concentration capacity of the analyte, with a percentage loss of activity by 25 % evaluated at $E_p^{o'}$ = 198 mV. In addition, the presence of the 17β-estradiol concentrations imposed the biosensor to be less prone to oxidisation; this was implicated to the observed reductive-redox potential shifts associated with the electrochemical activity of the redox liable species present at the surface of the biosensor.

4.1.4. The electrochemical behaviour of the estrogen receptor-α based biosensors and their affinity towards 17β-estradiol explicated.

The binding mechanism of the 17β-estradiol to the estrogen receptor alpha (ER-α), present in the biosensor surface was considered in order to understand the electrochemical affinity of these two biomaterials. Estrogen receptor alpha (ER-α) binding capabilities to the 17β-estradiol however have been thoroughly considered to occur through hydrogen bonding of the amino acids; arginine (i.e. Arg 394), glutamic acid (ie. Glu 353) and histidine (i.e. His 524) present at the ligand binding domain sequence of the ER-α with the hydroxyl group functional groups of the 17β-estradiol at; carbon number 3 and carbon number 17 of this compound (Mueller-Fahrnow and Egner 1999). The amino acid sequence of the ligand binding domain of the ER-α is known to possess a high percentage of the chemical active R-functional groups (i.e. R is any functional group) associated with amino acid sequence residues described in the ER-α sequences revised by authors; (Gustafsson 1999, Jensen and Jordan 2003, Skafar and Koide 2006). Nevertheless, these functional groups are susceptible to finite chemical reactions. In addition, the functional groups associated with the amino acid residues present in the ER-α sequence show intrinsic high chemical activity due to their non-polar basic and acidic properties. The binding mechanism of the17β-estradiol with the ER-α biomolecule present at the ER-α/SnSe(3-MPA)/L-cysteine/AuE biosensor surface is outlined in Figure 72.

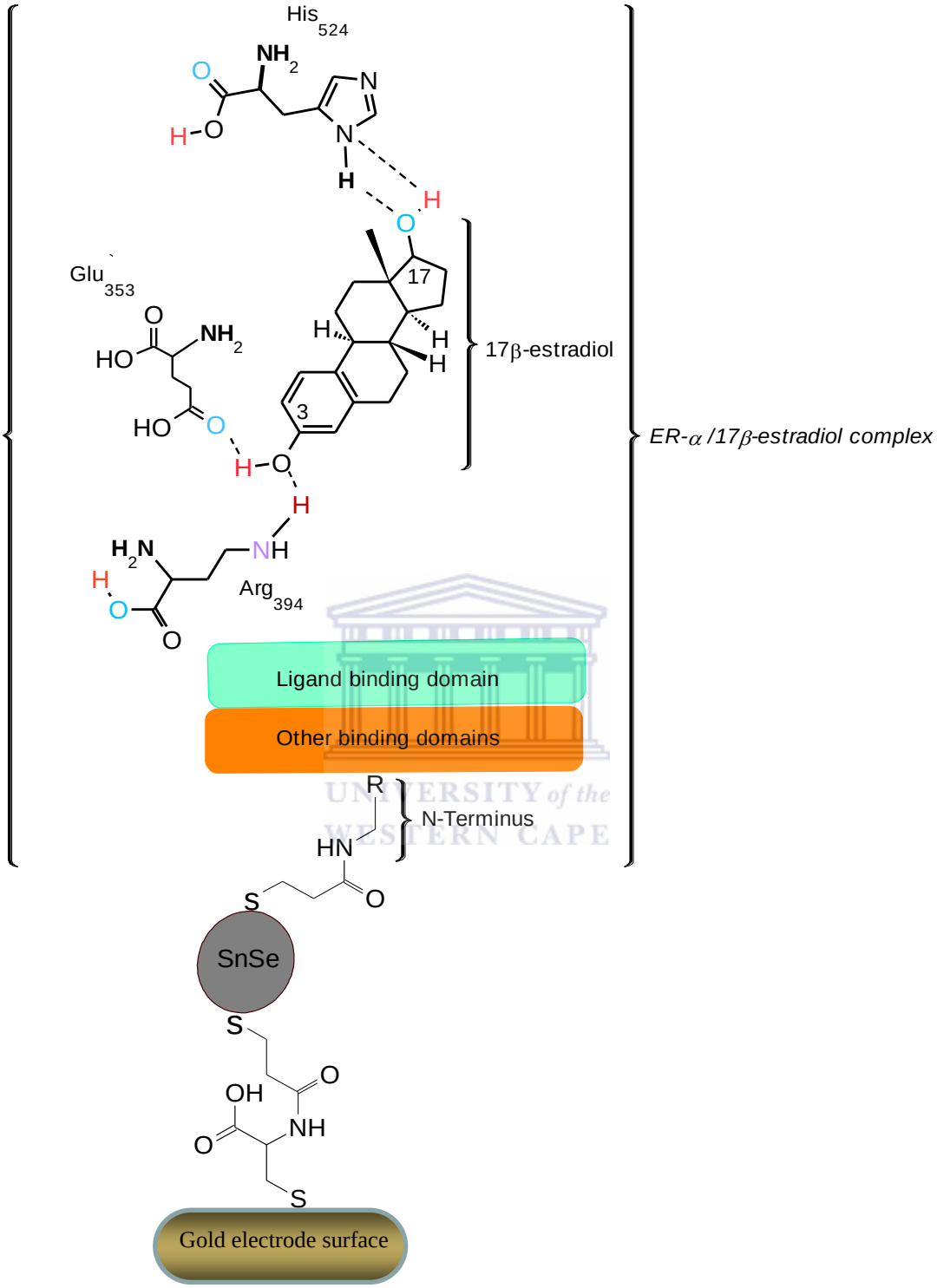

Figure 72: The association of the 17β-estradiol compound with the ER-α/SnSe(3-MPA)/L-cysteine/AuE biosensor electrode surface.

Histidine 524 (His_{524}) polarize the 17β-estradiol hydroxyl at carbon-17 by acting as a hydrogen acceptor at its carboxyl acid residue. In addition, the carbon-3 linked hydroxyl group of the 17β-estradiol compound is polarized through the covalent linkage with the amine functional group of the arginine394 (Arg_{394}) amino acid residue and the hydroxyl functional group of the glutamic acid number 354 (Glu_{354}). The chemical reactive amino acids participating during binding of the 17β-estradiol with the ER-α, that are as well present at the; ER-α/SnSe(3-MPA)/L-cysteine/AuE biosensor are herein categorised through their oxidation and reduction electrochemical capabilities and outlined in Figure 73 to Figure 75.

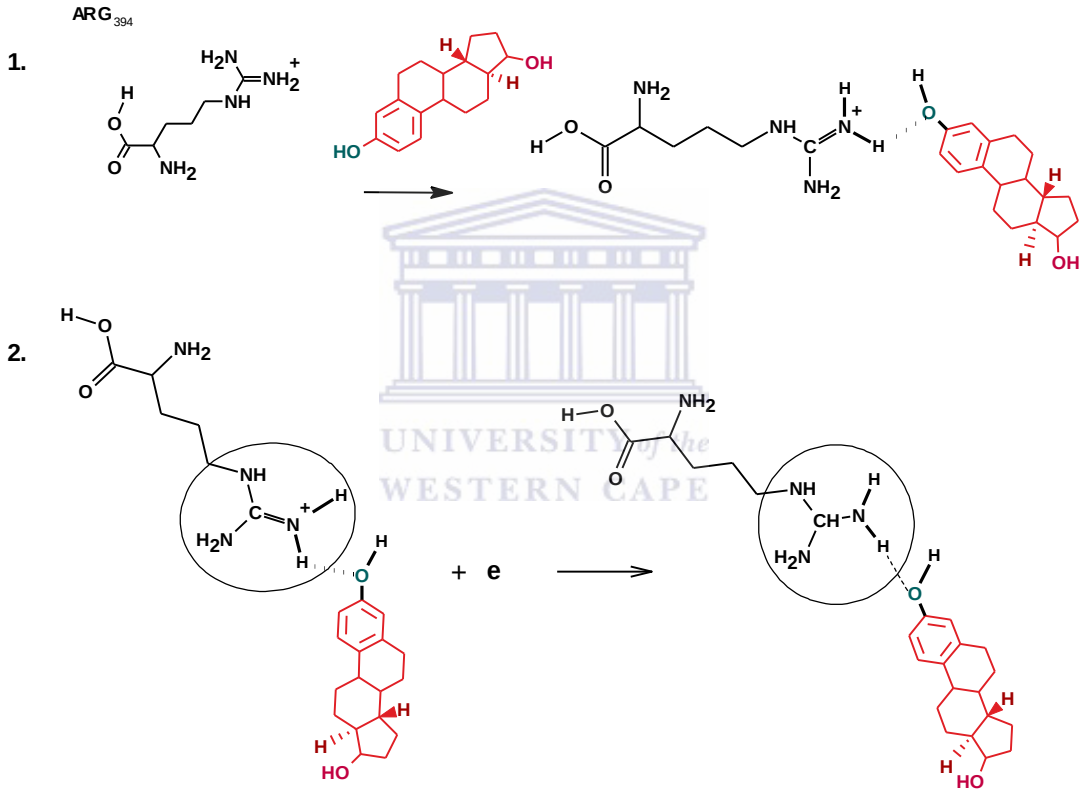

Figure 73: The electron-transfer reaction in an arginine 394 (Arg_{394}) amino acid of the ER-α, bound with the 17β-estradiol.

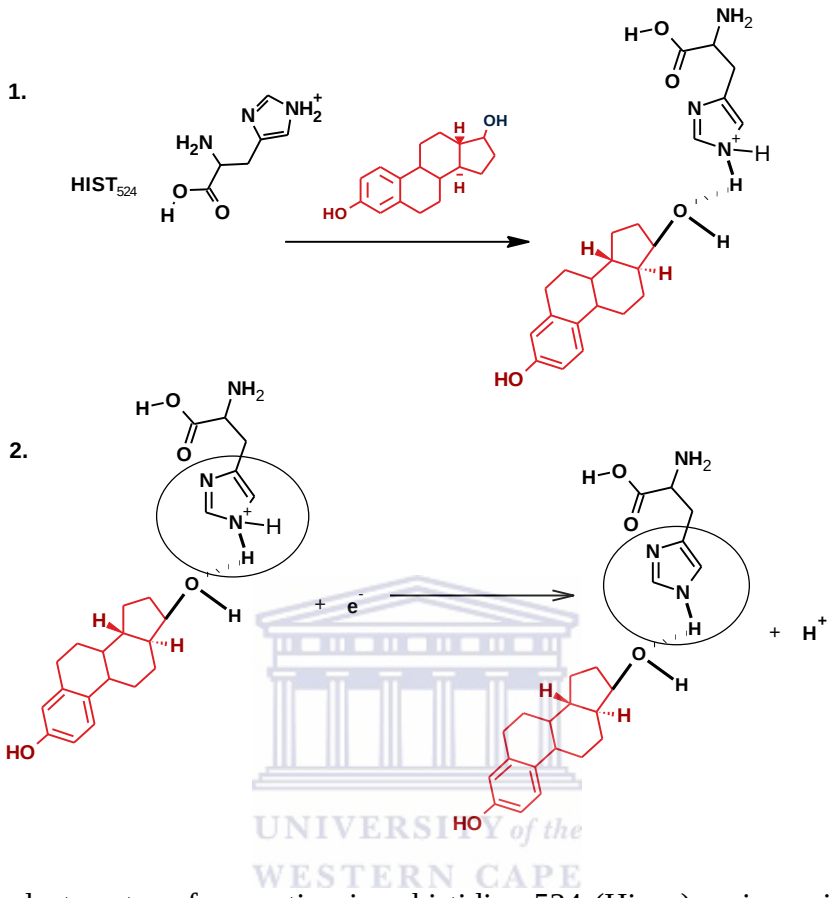

Figure 74: The electron-transfer reaction in a histidine 524 (His_{524}) amino acid of the ER-α bound with the 17β-estradiol.

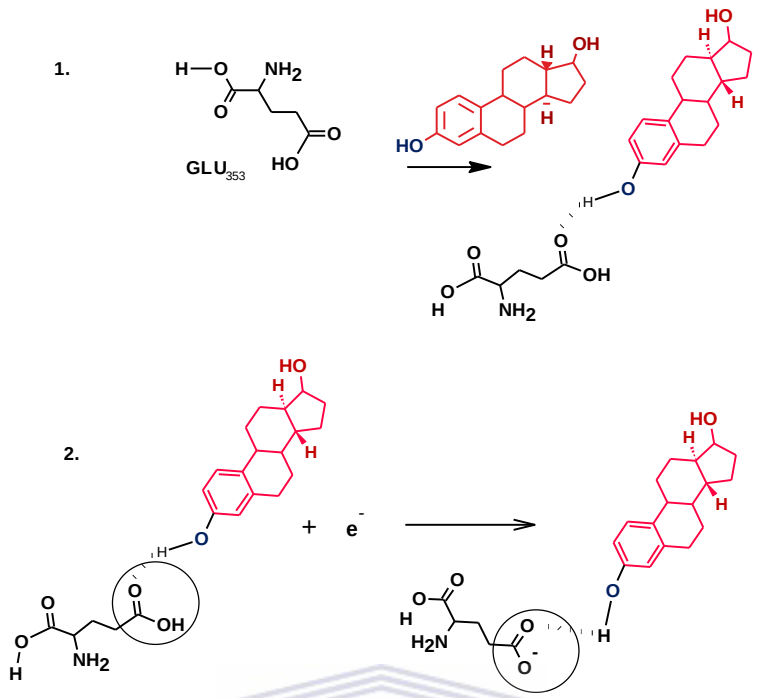

Figure 75: The electron-transfer reaction in a glutamic amino acid 353 (Glu_{353}) of the ER-α bound with 17β-estradiol.

4.1.5. Chemical properties of the estrogen receptor alpha (ER-α) related to its surface area, for binding with its ligand 17β-estradiol.

Proteins are known to bind efficiently to their native substrates, at the energy favourable specific binding sites (Moller and Amons 1985, Sugase, Dyson et al. 2007). The presence of a binding ligand at the protein's ligand binding site can imposes hydro-dynamism in the protein molecule due to possible; bond stretching, bond stabilization and conformation that in turn maximises its reactive surface and therefore, the reactivity of a protein is highly dependent on its surface area (Righetti 2005). In this regard, the protein-ligand interactions will rely critically on the concentrations of the binding substrates or ligands and the receptor binding site occupancy. The accessible surface area (A_s) of the ER-α recombinant protein was determined from its amino acid sequence, relative to its molecular weight, using the relation equation outlined in Equation 20 (Creighton 1993, Mishra 2010).

$$A_s = 6.3\ (M_r)^{0.73}$$

Equation 20

Estrogen receptor alpha (ER-α) was assumed to adopt a spherical helical conformation and the molecular weight of the receptor (M_r) was determined through chemical sequencing and compared with the specification supplied with the material when it was purchased. The surface area of the studied estrogen receptor alpha recombinant protein was evaluated to be 2.08×10^4 Å^2.

4.1.6. The electrochemical kinetic studies of the 17β-estradiol biosensor.

This section of the chapter examines the electrochemical kinetic dynamism of the developed biosensor at the formulated concentration arrays of the 17β-estradiol. The electrochemical activity of the biosensor films in the effect of molecular oxygen at different concentrations of 17β-estradiol is examined on implication that the activity and the stability of the protein biomolecules and receptors are vastly depend on the environmental conditions. The effect of molecular oxygen on the biosensor reactivity is studied at different solution mediums (i.e. under anaerobic and aerobic conditions, respectively) and reported in sections 4.1.6.1 and section 4.1.6.2, respectively.

4.1.6.1. The electrochemical kinetic performance of the ER-α /SnSe(3-MPA)/L-cysteine/AuE biosensor under anaerobic conditions.

The estrogen receptor-α based biosensor, electrochemical responses were evaluated at nano-molar concentration arrays of the 17β-estradiol analyte from 0 nM to 22.0 nM in a 0.1 M phosphate buffer solution of pH 7.4 at a scan rate of 30 mV/s and a potential window between 800 mV and -800 mV. The phosphate buffer solution was pre-degassed with a luminous flow of argon gas onto the buffer solution surface in order to preserve an oxygen-free electrolyte solution. The cyclic voltammetry responses of the biosensor corresponding to different concentrations of the 17β-estradiol analyte are presented in Figure 76 **(A)** and Figure 76 **(B)**.

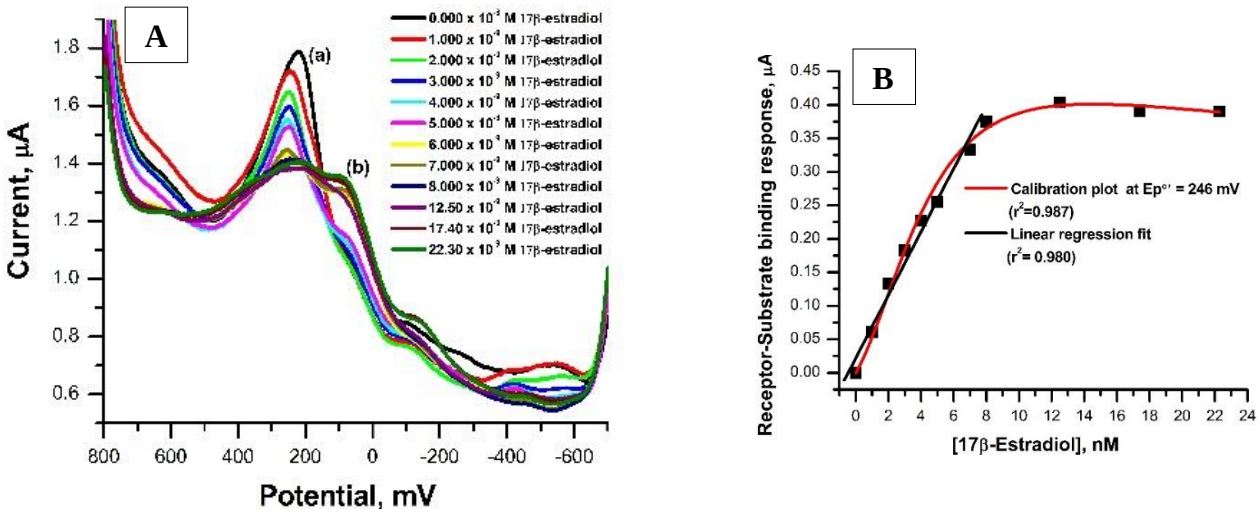

Figure 76: (**A**) The reduction O-square-wave voltammetry responses of the ER-α/SnSe(3-MPA)/L-cysteine/AuE biosensor corresponding to different concentrations of the 17β-estradiol, in 0.1 M phosphate buffer solution of pH 7.4 at 25 °C at a scan rate of 30 mV/s, under anaerobic conditions, and (**B**) the corresponding calibration plot.

The electrochemical activity of the biosensor in the presence and absence of the 17β-estradiol analyte was observed at a significant formal peak potential labelled **a** (i.e. a/a^{+}), corresponding to a formal potential magnitude; $E_p^{o'}$ of 246 mV. A decrease in the electrochemical response current signal succeeding to an increase in the 17β-estradiol concentrations in the buffer solution was observed for the 17β-estradiol concentrations from 1 nM to 17 nM. A fragment oxidation peak **b** (i.e. b/b^{+}) (i.e. at $E_p^{o'}$ = 88 mV) was observed after injection of 6 nM concentration of the 17β-estradiol solution. This was an implication of a secondary redox electrochemical conversion of the biosensor/17β-estradiol complex (i.e. the complex is formed after association of the 17β-estradiol with the ER-α present at the electroactive biosensor surface). The electrochemical kinetic responses of the designated biosensor were further simulated; by fitting the analytical calibration data with the statistical standard curves of the Origin 8 software and highlighted in Figure 76 **(B)**. The electrochemical response-concentration profiles obtained, showed high tolerance values when fitted with Gunnery exponential curve. The maxima effective-concentration (i_{max}) of 10.58 nM was evaluated for the ER-α/SnSe(3-MPA)/L-cysteine/AuE biosensor's electroactive surface, established from the maximum inhibition current response (B_{max}) value of 0.38 µA. The 50 % maximum inhibition concentration (IC_{50}) of the biosensor system was evaluated at 3.40 nM. A

statistical analysis and evaluation of the; detection limit (DL) and the dynamic linear range (DLR) of the biosensor, indicated a DL of 1.9 nM and the DLR from (0.184 - 7.25) nM.

4.1.6.2. The electrochemical kinetic performance of the ER-α /SnSe(3-MPA)/L-cysteine/AuE biosensor under aerobic conditions.

The biosensor implicated in the subject of this sub-chapter was developed through a procedure reported in section 4.1.3. The biosensor responses to different concentration arrays of the 17β-estradiol analyte were evaluated under the effect of molecular oxygen onto the phosphate buffer electrolyte solution. In this regard, a 0.1 M phosphate buffer solution was pre-degassed prior to the electrochemical studies, thereafter the molecular oxygen was allowed to freely rebound onto the buffer solution surface by removing a blanket argon gas on the buffer solution. The electrochemical parameters for these studies were consistent with the reported parameters in section 4.1.6.1. A scan rate of 30 mV/s, a potential window between 800 mV and -800 mV were employed; to study the electrochemical activity of the biosensor towards different concentrations of 17β-estradiol from 0 nM to 11 nM, under the effect of molecular oxygen in the 0.1 M phosphate buffer solution of pH 7.4. The O-square-wave voltammetry profiles of the biosensor under the predefined aerobic conditions is illustrated in Figure 77 (**A**).

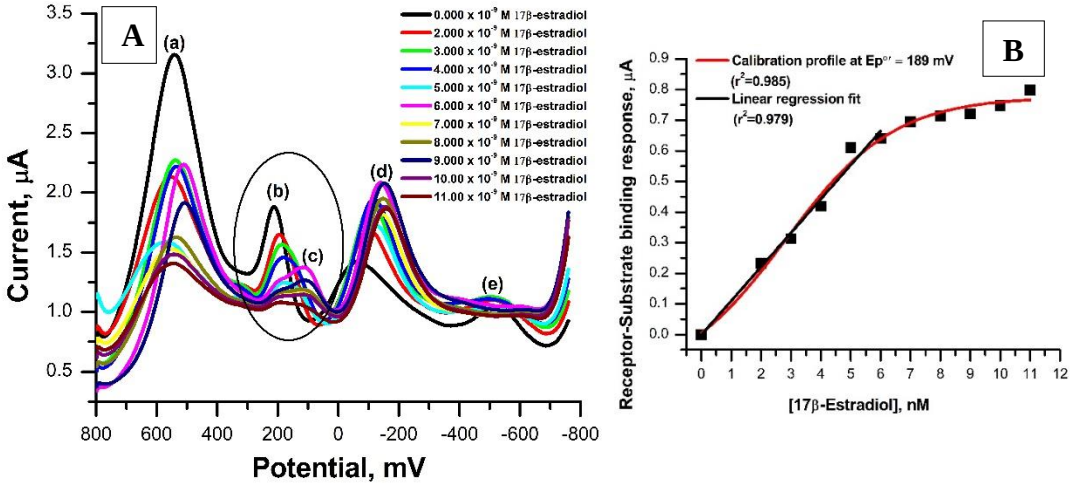

Figure 77: (A) The reduction O-square-wave voltammetry responses of the ER-α/SnSe(3-MPA)/L-cysteine/AuE biosensor corresponding to; 0.00 nM to 11 nM concentration of the 17β-estradiol, in a 0.1 M phosphate buffer solution of pH 7.4 at 25 °C at a scan rate of 30 mV/s, under aerobic conditions, and (**B**) the corresponding calibration plot of the biosensor.

The molecular oxygen present in the phosphate buffer solution during the revised studies of the ER-α/SnSe(3-MPA)/L-cysteine/AuE biosensor presented in Figure 77 **(A)**, showed distinct redox transfer reactions at **(a)**, **(d)** and **(e)** at zero concentration of the 17β-estradiol analyte at formal peak potential, $E_p^{o'}$ values of; 540 mV, -149 mV and 525 mV respectively. Nevertheless, successive increase of the 17β-estradiol concentrations influenced no catalytic electroactivity at the reported formal potentials due to un-specific interaction between the ER-α and the consecutive added 17β-estradiol in the electrolyte solution. Relatively the electrochemical effect corresponding to gradual increase in the 17β-estradiol concentration present in the phosphate buffer solution was observed at a formal peak potentials labelled **(b)** (i.e. at; $E_p^{o'}$ of 212 mV), reported to be related to the catalytic oxidation of the ER-α immobilized on the biosensor surface by the 17β-estradiol. Successive decrease in the current response from 1.88 µA at **(b)** (i.e. at zero concentration of 17β-estradiol) to a minimum current response value of 1.08 µA (i.e. at 11 nM of 17β-estradiol) for the biosensor, was observed. The loss of electrochemical activity of the biosensor was a resultant of accumulation of the 17β-estradiol analyte in the biosensor's diffusion layer that hinders its electron transfer potential. A total percentage loss of the electrochemical activity of the biosensor was reported to be 0.6 µA current folds after each successive addition of the 17β-estradiol

concentrations in the electrolyte solution. In addition a peak potential translocation was observed, with the successive increase in the 17β-estradiol concentrations from an; $E_p^{o'}$ value of 201 mV to a formal peak potential, $E_p^{o'}$at 186 mV determined at zero and11 nM 17β-estradiol concentrations respectively {i.e. at**(b)}**. A redox split peak, labelled **(c)** (i.e. at $E_p^{o'}$ = 110 mV) was observed in the presence of the 17β-estradiol concentrations above 5 nM, this was an implicated trans-electrochemical activity of the; 17β-estradiol activated ER-α surface, showing post-electrochemical activity at the relative formal potential $E_p^{o'}$ of 110 mV {i.e. at **(c)**}. Receptors, protein biomolecules, enzymes, ribonucleic acid molecules and cells are prone to reactive oxygen radical oxidative stresses (ROS), wherein a reactive oxygen molecule readily oxidizes, resulting into formation of a reactive radical that respectively binds with the metals and the reactive functional groups associated with the biomolecules (Walsh 2002, Vo-DinH 2010). This consequence is summarised through a chemical reaction presented in the next equation; Equation 21.

$$2O_2 + 4e^- + 4H^+ + R \rightarrow {}^{*-}OR + H_2O + O_2^-$$

Equation 21

In the predefined chemical reaction, *R* represents any biomolecule with a liable active site for oxygen binding. However oxidative stresses imposed on bio-molecules are highly reversible electrochemical reactions (Valko, Rhodes et al. 2006). In these studies, the oxidative stresses imposed on the ER-α biomolecule present on the biosensor surface were observed at formal potentials $E_p^{o'}$ between -149.0 ± 6 mV and distinguished by peak **(d)** (i.e. [ER-α(O)]/[ER-α(O)]$^+$) in Figure 77 **(A)**. The O-square-wave voltammetry response profiles of the implicated biosensors at different concentration of the 17β-estradiol were further interpreted through fitting the response currents and concentration values with a sigmoidal response curve shown in the analytical calibration profile presented in Figure 77 (**B**). A regression co-relation r^2 of 0.987 and the standard errors of the fitted parameters were reported to be less than 1 %. A dynamic linear range (DLR) of 3.95 nM to 6.09 nM and the detection limit of 1.75 nM were determined from the catalytic response profiles highlighted in Figure 77 (**B**) for the ER-α/SnSe(3-MPA)/L-cysteine biosensor studies, under aerobic conditions.

4.1.6.3. The electrochemical kinetic behaviour of the biosensor in the absence of L-cysteine films.

An intermediate thin monolayer film is a pre-requisite material during the development of biosensors on account of avoiding electrochemical stresses imposed on critically sensitive biomaterials. The L-cysteine molecule described in section 4.1.1, is associated with the electroactive functional groups present, that are responsible for capturing free electrons susceptible to electron transfer reactions, on post-modified films or materials. In these studies, the intermediate L-cysteine films, employed to stabilize the SnSe(3-MPA) quantum dot molecules on biosensor surface were isolated, on implication of their effective electron transfer redox activity at a formal potential, $E_p^{o'}$ of 211 mV. The biosensors comprised of thin films of the; ER-α/SnSe(3-MPA) immobilised on gold electrode surfaces. The O-square-wave voltammetry potential window between -800 mV and 600 mV at a scan rate of 30 mV/s was studied. Figure 78 (**A**) represents the ER-α/SnSe(3-MPA) film deposited on the gold electrode surface, responses to different concentration of the 17β-estradiol analyte between 0 nM to 25 nM.

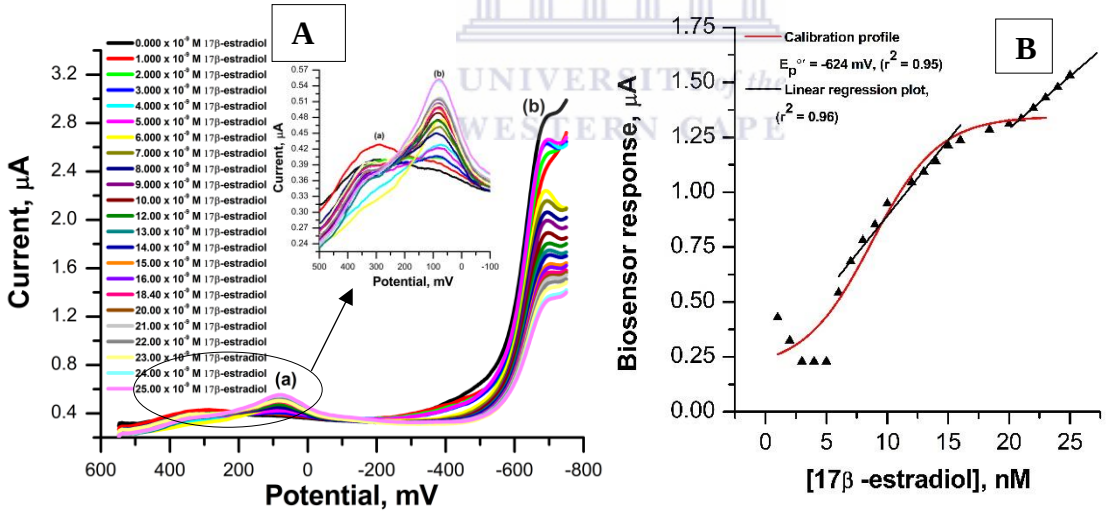

Figure 78: The (**A)** reduction O-square wave voltammetry responses of the ER-α/SnSe(3-MPA)/AuE biosensor electrode in 0.1 M phosphate buffer solution of pH 7.4 at 25 °C, at a scan rate of 30 mV/s, at different concentrations of 17β-estradiol, and (**B**) the corresponding calibration curve.

The response profiles of the ER-α/SnSe(3-MPA)/AuE electrodes prompted through the O-square-wave voltammetry, was distinguished by the two distinct oxidation peaks. These were observed at formal potentials; $E_p^{o'}$ of **(a) (**i.e. at 105 mV) and **(b)** (i.e. at 79 mV), and a reduction peak formal potential $E_p^{o'}$ at **(c)** (i.e. at -698 mV) in the O-square-wave voltammetry profiles presented in Figure 78 (**A**). Successive increase in the 17β-estradiol concentrations imposed an in-consistent increase of the electrochemical sensitivity generated at the oxidation formal potential, $E_p^{o'}$ at **(a)** (i.e. at 79 mV). Figure 78 **(A)** insert highlights; the redox peaks at **(a)** and **(b)** at the potential window between -100 mV to 800 mV. The distinct electrochemical redox transfer peak at **(a)** was distinguished to be a concentration independent non-catalytic electrochemical effect related to unspecific association of the 17β-estradiol analyte with the ER-α on the receptor-sensor surface. Increasing concentrations; from 1 nM to 4 nM of the 17β-estradiol analyte imposed successive increase in the ER-α/SnSe(3-MPA) electrode's sensitivity at formal potential **(b)** (i.e. $E_p^{o'}$ of -624 mV) indicating a 17β-estradiol concentration-dependent catalytic response of the ER-α immobilised on the ER-α/SnSe(3-MPA) sensing surface. The ER-α/SnSe(3-MPA) sensing film-responses towards different concentrations of the 17β-estradiol were further corroborated by fitting the sigmoidal response current vectors with the sigmoidal curve of Origin 8 software and shown in Figure 78 (**B**).A regression root mean square, r^2 of 0.859, associated with the standard statistic errors below 7 %, were reported for the fitted statistical sigmoidal curve. In the obtained calibration curve presented in Figure 78 (**B),** secondary catalytic concentration-dependent responses of the sensing films were observed at the concentrations of the17β-estradiol analyte greater than 20 nM. The sigmoidal characteristic behaviour of the ER-α/SnSe(3-MPA) films towards the 17β-estradiol was related to the affinity-binding mechanism of the ER-α to the 17β-estradiol. It suggests that, when a ligand binds to its native receptor biomolecule, it imposes a receptor to adopt a stable conformation and consecutively sustains activation prior to post protein-protein translation and transcription functions (Cheskis, Karathanasis et al. 1997, Stokes, Alston-Mills et al. 2004). The catalytic calibration curve illustrated in Figure 78 (**B**) was further used to evaluate the detection limit (DL) and the dynamic linear range (DLR) of the ER-α/SnSe(3-MPA)/AuE sensing films. The DLR of between 1.69 nM to 80 nM associated with the detection of 1.9 nM were determined. The L-cysteine film pre-modified on the electrode surface; before immobilization of the semiconducting SnSe(3-MPA) quantum dots on the biosensor surface, played a critical role in tuning of the sensing film sensitivity and specificity that is targeted at the formal potential, $E_p^{o'}$ of

212 ± 90 mV. Nevertheless, the electrochemical catalytic reactivity of the biosensor at the formal potential, $E_p^{o'}$ of -624 mV was found not to be dependent on the L-cysteine monolayer; intermediate supporting material on the biosensor surface. A distinct electrochemical activity was rather observed at this region corresponding to catalytic reduction of the electroactive amino acid group residues present at the ER-α by 17β-estradiol. Those were however slightly inactive and hindered when the L-cysteine was present at the biosensor electrode surface.

4.1.6.3.1. Time-dependent dynamic electrochemical responses of the ER-α/SnSe(3-MPA) films in the presence of 17β-estradiol.

The kinetic properties of the ER-α/SnSe(3-MPA)/AuE films were further evaluated through the dynamic single-potential amperometric studies. A formal potential $E_p^{\circ'}$ of -698 mV was applied at the acquisition time window between 0 s to 200 s. Figure 79, presents the amperometric response profiles of the ER-α/SnSe(3-MPA)/AuE films to different concentrations of the 17β-estradiol.

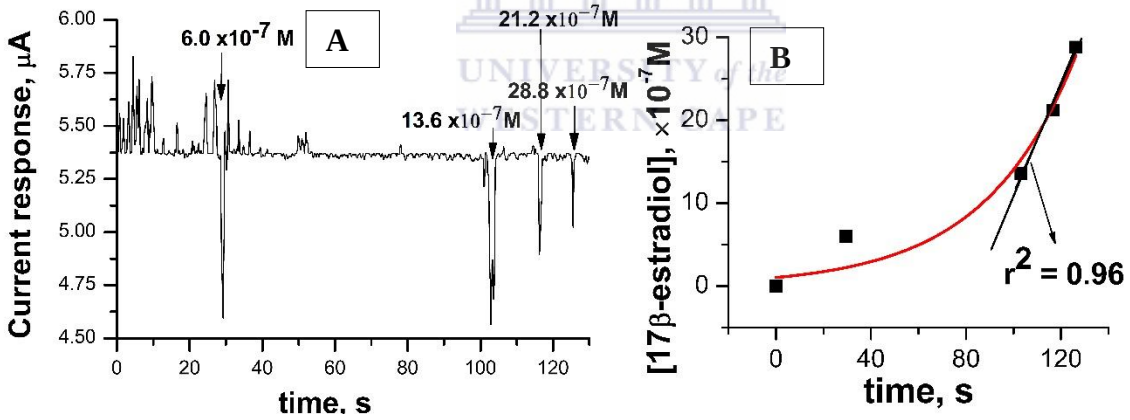

Figure 79: (**A**) Single potential dynamic time-based studies, and (**B**) the calibration profile corresponding to the ER-α/SnSe(3-MPA)/AuE surface responses in 0.1 M phosphate buffer solution at different concentrations of 17β-estradiol.

The amperometric studies highlighted in Figure 79 (**A**) revealed an elaborate fractional recovery of the biosensor surface during injection of the 17β-estradiol concentrations; between; 0.6 µM to 1.3 µM. A decrease in the ER-α/SnSe(3-MPA)/AuE current response activity by 1.05 current folds was observed, corresponding to: 0.6 µM to 2.8 µM concentrations of 17β-estradiol. The response

time ($t_{Response}$) of 1.2 s was evaluated at the kinetic response concentrations; between 1.36 µM to 2.8 µM. The ER-α's amperometric kinetic properties with respect to the 17β-estradiol were further described through the complex formation, expression relating the estrogen receptor-α concentrations with the 17β-estradiol (E2) concentrations, evaluated at equilibrium. The kinetic approximation of the reaction rates are described through equations; Equation 22 to Equation 23 (Charles R. Sanders , Walsh 1979, Babine and Bender 1997, DeGraw, Keiser et al. 2010);

$$[\mathrm{ER}-\alpha]+[\mathrm{E2}] \underset{k_{-1}}{\overset{k_1}{\rightleftharpoons}} [\mathrm{ER}-\alpha:\mathrm{E2}],$$

Equation 22

$$\text{Rate of dissoiciat ion} = \frac{\Delta[ER-\alpha][E2]}{\Delta t},$$

Equation 23

The parameters; k_1 and k_{-1} in Equation 22, describe the association and dissociation rate constants respectively, *[E2]* describes the concentration of the 17β-estradiol, *[ER-α]* represents the concentration of the estrogen receptor-α, and *[ER-α:E2]* is the concentration of the receptor-ligand complex. The total concentration of the complex $[ER\text{-}\alpha: E2]_{total}$ after binding with its associated ligand is evaluated through relating the evaluated total concentrations of the estrogen receptor alpha and the 17β-estradiol analyte through the expressions presented in Equation 24.

$$[ER-\alpha:E2] = E2_{total}-E2, at\ t=0, [ER-\alpha:E2] \approx 0\ or\ [ER-\alpha:E2]=[ER-\alpha]_{total}-[ER-\alpha]$$

Equation 24

The dissociation rate (k_d) associated with the estrogen receptor-α based biosensor was 0.76×10^{-7} M/s. A systematic electron transfer mechanism of the ER-α on the biosensor surface was then derived for the developed electrochemical systems and presented in Figure 80.

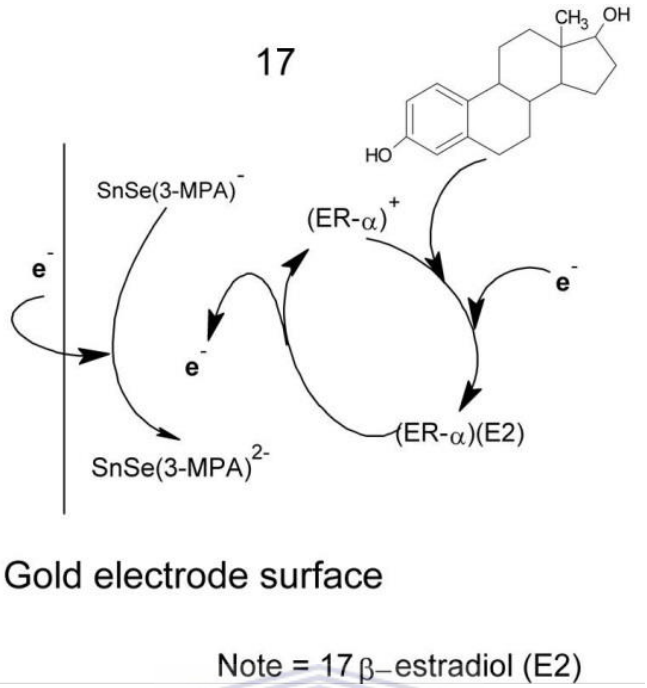

Figure 80: The electron transfer mechanism of the AuE/SnSe(3-MPA)/ER-α surface in the presence of the analyte; 17β-estradiol.

The proposed electron transfer mechanism in Figure 80 describes the association of the 17β-estradiol with the ER-α, present at the diffusion layer the biosensor electrode surface. The 17β-estradiol analyte electrostatically associates itself with the liable amino acids residues at the ligand binding domain of the ER-α (i.e. histidine, arginine acid and glutamic acid) to initiate hydrogen bonding. The histidine and arginine are positively charged, the glutamic acid is negatively charged, however, after hydrogen bonding occurs between the ER-α and the 17β-estradiol, these amino acids are polarised thus the receptor at its ligand binding site becomes neutrally charged (i.e. the binding of the 17β-estradiol catalytically reduces the ER-α). Oxidation of the ER-α, however can induce electron transfer reactions at the negatively or neutrally charged susceptible amino acids, due to the residues' basic and polar properties. All statistic data re-evaluation, interrogated in this herein presented work were done using the ANOVA tests on the data set of Origin 7 and Origin 8 software, including determination of the regression correlation co-efficient and the scientific error percentages.

Chapter 5 Fluorescence detection of the 17β-estradiol using the ER-α/SnSe(3-MPA) films

Fluorescence spectroscopy analysis was used to evaluate the photo-electrochemical properties of the estrogen receptor –α based biosensor and to evaluate the mode of affinity between the estrogen receptor alpha (ER-α) and the analyte; 17β-estradiol. Binding of the 17β-estradiol to the ER-α is suggested to activate the receptor at its ligand binding domain (Babine and Bender 1997, Jensen and Jordan 2003, Garidou, Laffont et al. 2004, Skafar and Koide 2006, Yoon, Choi et al. 2010). The fluorescence spectroscopy studies of the estrogen receptor alpha (ER-α) evaluated in section 2.3.2 were distinguished with high fluorescence efficiency due to the $\pi^* \rightarrow \pi$ and $\pi^* \rightarrow \sigma$ electronic transitions derived from the aromatic amino acids: histidine, tyrosine, tryptophan and phenylalanine. The ER-α/SnSe(3-MPA) films were produced through a procedure shown in section 5.1.

5.1. Fluorescence properties of the intermediate biosensor materials

A solution of the 3-mercaptopropionic acid capped tin selenide quantum dot was chemically integrated with the ER-α in the molar ratio of (2:1), in the presence of 0.01 M 1-ethyl-3-(3-dimethylaminopropyl) carbodiimide (EDC) and 0.005 N-hydroxysuccinimide (NHS) in a 2:1 ratio, respectively. For the fluorescence studies, the prepared films were diluted with 0.1 M phosphate buffer solution of pH 7.4. Primarily, the distinct fluorescence properties of the intermediate biosensor materials were evaluated in 0.1 M phosphate buffer solution of pH, 7.4 {i.e. (**1**) SnSe(3-MPA)-QDs/ER-α (**2**) SnSe(3-MPA) and (**3**) ER-α films}. Figure 81, outlines the fluorescence spectra of the different materials at a fluorescence emission range between 400 nm to 750 nm, excitation at a wavelength of 385 nm.

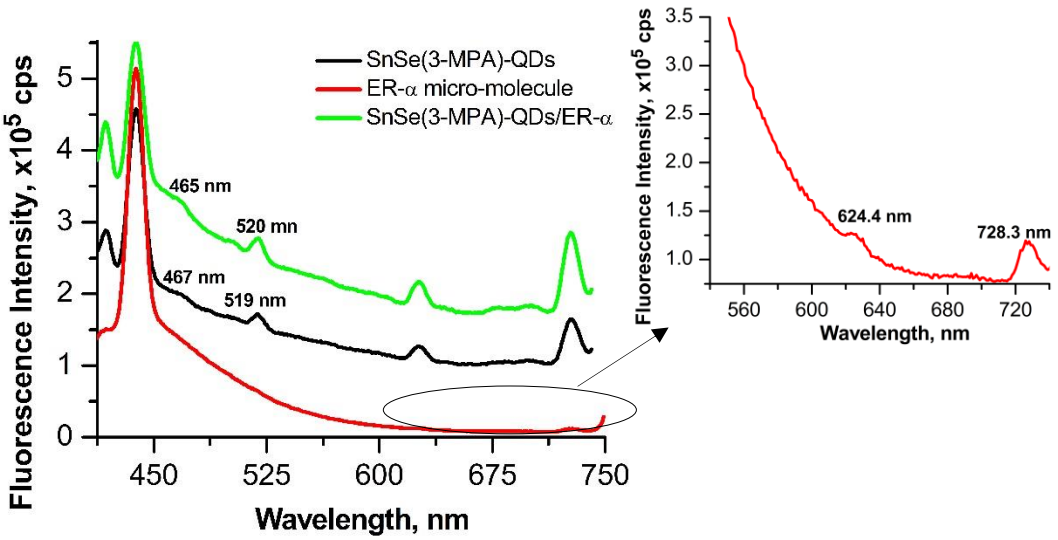

Figure 81: The fluorescence spectra of the intermediate estrogen receptor-α based biosensor components dispersed in 0.1 M phosphate buffer solution of pH 7.4.

The photo-electronic emission bands accentuated at near-infrared spectra region of the SnSe(3-MPA) quantum dots and the ER-α/SnSe(3-MPA) complex, labelled; 465 ± 5 nm and 519 ± 1 nm in Figure 81 were a resultant of the electronic transitions, within the electronic band gap of the SnSe(3-MPA) quantum dot's exciton. The other electronic transitions observed in the spectrum of SnSe(3-MPA) quantum dots at 626 nm and 727 nm, were associated with the electronic transitions at the carboxyl acid functional groups of the 3-mercaptopropionic acid capping on the quantum dot surface. These were also observed in the spectra of the estrogen receptor α (ER-α) (i.e. red spectrum) highlighted in Figure 81, consistent to the carboxylic acid derived amino acids present at the conserved C-terminus region of the ER-α. The ER-α (i.e. red spectrum) was distinguished by the lowest fluorescence efficiency compared to the SnSe(3-MPA) quantum dots (i.e. black spectrum) observed at the low fluorescence energies region from 456 nm to 750 nm. Doping the ER-α with the highly fluorescence energy efficient SnSe(3-MPA) quantum dots improved the energy efficiency by 18 folds, evaluated at 517 nm. The ability to induce the fluorescence efficiency of the ER-α implied the ability of the ER-α to act as an acceptor molecule as opposed to the SnSe(3-MPA) which exhibited typical donor properties.

5.2. Fluorescence spectroscopic behaviour of the ER-α/SnSe(3-MPA) films in the presence of the 17β-estradiol.

The fluorescence activity of the ER-α/SnSe(3-MPA) films towards the compound; 17β-estradiol was evaluated at concentration arrays of the 17β-estradiol from; 0 µM to 10 µM. A fluorescence wavelength from 450 nm to 750 nm was evaluated using an excitation wavelength of 385 nm. Fluorescence response profiles of the ER-α/SnSe(3-MPA) films at different concentrations of 17β-estradiol are presented in Figure 82 (**A**) with the relative calibration plot for the relative assay.

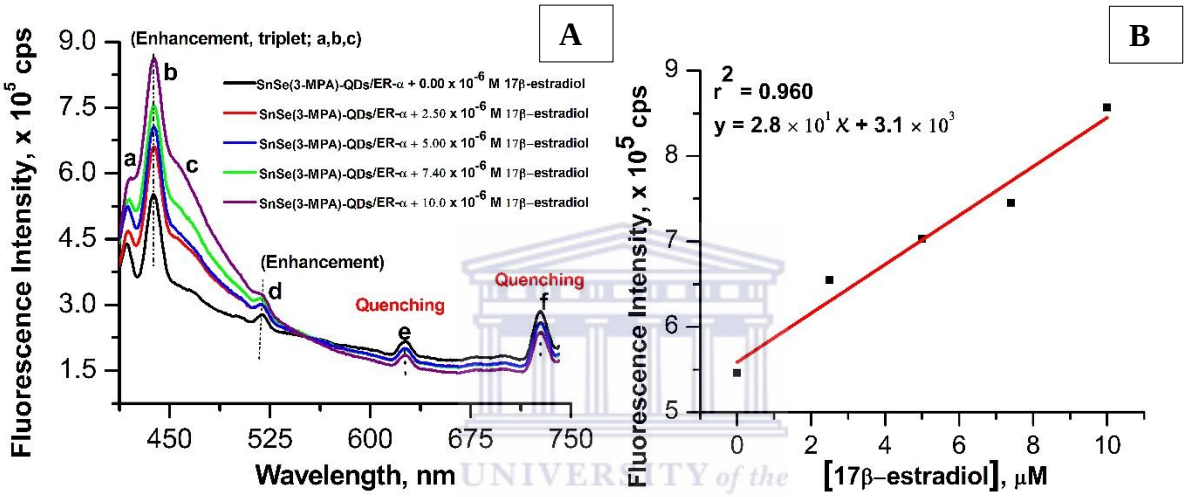

Figure 82: The fluorescence spectra of the ER-α/SnSe(3-MPA) films in 0.1 M phosphate buffer of pH 7.4 at 25 °C, at different concentrations of 17β-estradiol.

The triplet split peak labelled **a**, **b** and **c** (i.e. at: 422 nm, 438 nm, and 458 nm) in the fluorescence spectra highlighted in Figure 82 (**A**) of the ER-α/SnSe(3MPA) complex at zero molarity concentration of the 17β-estradiol was deduced to be due to, multiple fluorescent active amino acids residues of the ER-α. Relatively, increasing the concentrations of the analyte, 17β-estradiol resulted in the enhancement of the fluorescence efficiency of the signals observed at: **a**, **b**, **c** and **d**. The enhancement of fluorescence signals were relatively proportional to the observed quenching of the fluorescence efficiency observed at **e** and **f**. The fluorescence responses observed in Figure 82 (**A**) suggested, an allosteric association of the 17β-estradiol with different liable function groups in the ER-α (i.e. at its amino acid residues, in the amino acid sequence of the receptor), with diverse fluorescence active chromophores associated with their distinct mode of binding with the 17β-estradiol. This can be correlated to the high fluorescence activity of the amino acids; Arginine 394,

Glutamic acid 353 and Histidine 524 at the ligand binding domain of the ER-α, that are responsible for hydrogen bonding with the 17β-estradiol. The enhancement of fluorescence intensities were observed at: **a** (i.e. 422 nm), **b** (i.e. 438 nm), **c** (**i.e.** 458 nm) and **d** (i.e. 519 nm) and the quenching process were observed at: **e** (i.e. 625) nm and **f** (i.e. 726 nm). The fluorescence responses of the ER-α/SnSe(3-MPA) films fitted accurately with the linear regression equation presented in Figure 82 (**B**). The dynamic linear range (DLR) between 363 nM to 1039 nm and the detection limit (DL) of 500.54 nM were evaluated for the fluorescence induced bio-reactivity of the ER-α/SnSe(3-MPA) films at different concentrations of the; 17β-estradiol analyte. Different methods developed for evaluating different concentrations of the 17β-estradiol, comparing their detection limits {i.e. DL(s)} and the dynamic linear ranges {i.e. DLR(s)} are outlined in Table 9.

Table 9: The comparison of different detection methods; their analytical properties, and capability to detect the 17β-estradiol concentration arrays.

Method of detection	*Dynamic linear Range (DLR) (/nM)*	*Limit of detection (LOD) (/nM)*	*Method sensitivity (μM/μA)*
Electrochemical receptor based biosensor [i.e. AuE/SnSe(3MPA)/ER-α] (*NB: reported in this text)*	1150 – 2660	2350	-
Standardized-Electrochemical receptor based biosensor [i.e. AuE/SnSe(3-MPA)/ER-α] *(NB: reported in this text)*	1.69 - 13.5	1.9	2.6
Electrochemical based biosensor [*AuE/L-cysteine/SnSe(3-MPA)/ER-α*] *(NB: reported in this text)*	0.184 – 7.85	1.9	3.15
Fluorescence induced detection [i.e. with ER-α/SnSe (3-MPA) films] *(NB: reported in this text)*	100 -10000	8800	-
Enzyme based biosensor [i.e. AuE/ZnSe-(3-MPA)/CYP3A4] *(Ndangili, Jijana et al. 2011)*	80 - 290	0.1	-
Electrochemical biosensor [i.e. poly(L-serine) films modified electrodes] *(Song, Yang et al. 2008)*	100 - 30000	20	-
ELISA kit *[i.e. from AB Cam (reference number: ab 108667)]*	0.07 – 7.34	0.03	-
LC/MS/MS *(Petucci, Lloyd et al. 2010)*	0.009 – 3.67	0.009	-

Chapter 6 Research implications and conclusion

The distinct sensitivities of the biosensor methods developed for the detection of 17β-estradiol were reported from 1.34 nM/µA (i.e. the lowest reported value) to 3.125 µM/µA (i.e. the highest value). The lowest sensitivities were obtained for the AuE/L-cysteine/SnSe(3-MPA)/ER-α biosensor studied, under aerobic conditions. The electrochemical oxidation of the ER-α was determined to be greatly influenced by the presence of the reactive oxygen molecule, appertained to the electrochemical reduction of the reactive oxide radicals on the ER-α surface, resulting into the oxidative stress imposed on the estrogen receptor alpha active sites. The reduction peaks due to the oxidative stress on the ER-α were observed at the formal potential; $E_p^{o'}$of -149 mV. Relatively, the oxidative stresses imposed on the biosensor surface were determined to also affect the binding affinity of the biosensor, with respect to its capability to induce electron transfer reactions at the formal potential; $E_p^{o'}$ of 198 ± 50 mV, associated with the catalytic redox conversion of the ER-α by the analyte 17β-estradiol. The dynamic linear ranges (DLR) of the biosensor was also relatively affected wherein, the dynamic linear ranges of; (0.184 nM to 7.25 nM) and (3.95 nM to 6.09 nM) were reported for the ER-α/SnSe(3-MPA)/L-cysteine/AuE biosensor under anaerobic and aerobic conditions respectively. Nevertheless, the limit of detection was vaguely affected. The kinetic binding affinity (B_{max}) of 7 nM, indicated the high binding affinity of the developed ER-α/SnSe(3-MPA)/L-cysteine/AuE biosensor to the 17β-estradiol analyte concentrations. The electrochemical binding affinity was associated with a 50 % inhibition concentration (IC_{50}) of 3.4 nM. Comparison and method validation through the fluorescence induced binding of the 17β-estradiol to the ER-α provided 1000 folds higher detection limits and dynamic ranges compared to the electrochemical methods of detection. The platform re-usability studies indicated that the ER-α/SnSe(3-MPA)/L-cysteine/AuE biosensor electrodes can be employed once-off due to the huge loss of the surface electroactivity by more than 50 %. Nevertheless, these recycled biosensor films were capable of inducing secondary electrochemical effect, at the formal potential, $E_p^{o'}$of approximately 99 mV, where the current amplification was proportional to the concentration of the 17β-estradiol injected into the phosphate buffer solution. These studies were reported in cyclic voltammetry profiles in Figure 96 at the appendix section of this thesis. The high specificity of the developed biosensor methodology was due to the advantageous application of the ER-α, in vitro that is highly specific towards the subject

compound; 17β-estradiol. The estrogen receptor-α based biosensor developed in this research established a reliable high specific and selective approach to determination of even pico molarity levels of the 17β-estradiol analyte applicable to different scopes of applications, that can be focused to clinical evaluation assays and wastewater contaminant level screening of the 17β-estradiol. Food and drug administrative (FDA) agency reports more than twenty administered drugs with active ingredient being 17β-estradiol. The lowest observable effective concentration (LOEC) of 17β-estradiol to alter abnormalities related to development of the secondary reproductive characteristics in aquatic male minnow fatheads was reported to be initiated by concentration levels of 17β-estradiol between (4 – 420) pM and about (105 – 315) pM for its homologue compound; 17α-estradiol (Shapell, Hyndman et al. 2010). Different electrochemical approaches to determination of different concentration arrays of the 17β-estradiol compound were developed, these methodologies involved application of the ER-α/SnSe(3-MPA)/L-cysteine films immobilised on the gold electrode surfaces. Chemical tuning of the electrochemical properties of the biosensors was done; this was through eliminating the L-cysteine monolayer assemblies onto the gold electrode surface, this improved the dynamic linear ranges from (0.184 – 7.25) nM to (1.69 – 80) nM, in the presence and absence of L-cysteine, respectively. The catalytic oxidation of the estrogen receptor alpha, depended on the different concentrations of the 17β-estradiol present, occurred at Epº' of 211 mV ± 50 mV, for the biosensor assemblies pre-modified with L-cysteine. The un-specific reduction reactions were also observed at far negative formal potentials; Epº' at approximately -500 ± 10 mV {i.e. in the voltammogram of Figure 76 (**A**) and Figure 77 (**A**)}. Incongruously, the absence of the L-cysteine on the biosensor surface imposed 17β-estradiol-concentration dependent catalytic reduction of the ER-α on the biosensor surface at Epº' of approximately -648 ± 50 mV, with un-specific oxidation occurring at Epº' of approximately: 100 mV and 310 mV. The L-cysteine based biosensor assemblies were relatively stable. Studies of the terbium alloyed SnSe(3-MPA) quantum dots, indicated distinctively high photo-electrochemical activity and the improved electrochemical stability, this can favourably improve the applicability of these quantum dot nanomaterials. The indirect band gap of the Tb-SnSe(3MPA) quantum dots evaluated from the photon energy estimation was 2.8 eV, that is 0.3 magnitudes less than the unmodified SnSe(3-MPA) quantum dots, associated with the indirect band gap energy of 3.14 eV. These quantum dots not only showed improved conductivity, they exhibited greater surface to surface repulsion and improved fluorescence efficiencies. The

improved fluorescence efficiencies of the Tb-SnSe(3-MPA) quantum dot nanostructures was due to the terbium ions that are high fluorescent and known for their applications in the development of fluorometric probes (Zhang, Li et al. 1997, Beltyukova and Egorova 1998, Canada and N. 1998, Goèmez-Hens and Aguilar-Caballos 2002, Taha, Hassan et al. 2007, Kumara, Kumarib et al. 2011). 17β-estradiol is associated with the critical roles in diverse species genome, beginning with its function in regulation of menopausal cycle in female species, to regulation of the endocrine systems (Davis, Kennedy et al. 2000, Duellman, Calaoagan et al. 2010). Clinic and endocrinology studies have reported; 17β-estradiol to be responsible for the regulation of the activity in gene expression, in microvascular endothelial cells by raising mRNA levels of GTP-Cychohdrolase I (i.e. GTP is the guanosine triphosphine), that could result in cardiovascular disorders in diabetic woman, induced through down regulation of the gene expression; induced by high glucose levels (Asaka, Toshio et al. 2007). GTP-Hydroxylase-I gene mutations have also been reported present in the Parkinson and Segawa diseases {i.e. disordered of the central nervous system (CNS) reported by (Craig, R. et al. 1996, Chunyou, Wentao et al. 2008)}. The compound is associated with other effects, related to the presence of high concentrations in *Homo sapiens* by activating the ER-α (s) present. Herein, 17β-estradiol contingent post-inhibition and regulation of the vascular constriction were reported (Asaka, Toshio et al. 2007, Ba, Lu et al. 2007). 17β-estradiol binding to the estrogen receptor alpha in particular can trigger and activate many life cycles in the target cells due to the activation of the G-protein coupled co-activators, co-suppressors, the cyclic adenosine monophosphate (CAMP) signalling pathways (Levin 2001) and other ligation receptor specific mechanisms. However, physiological successive binding of the 17β-estradiol can initiate many adverse effects on the targets cells and tissues due to the modulation of the cell cycles and gene expression, that can lead to over-expression of genes and cell proliferation. Estrogen receptor alpha is reported to be expressed in most tumour cells, consequently in tumour therapies, a cell's responsiveness to the 17β-estradiol agonist is monitored, wherein positive (i.e. ER+) tumour cells (i.e. induced activation of the ER-α by the 17β-estradiol) are correlated to the tumorous tissues (Hill, Fuqua et al. 1989). 17β-estradiol's excessive concentration modulating effects; have been reported at micro-cellar and tissue levels, correlated to the ovarian disorders, cardiovascular disorders, pulmonary effects, gastrointestinal defects, and other diverse abnormalities in the central nervous system (Mikkolaa and Clarksona 2002, Garidou, Laffont et al. 2004). The authors (Mueller-Fahrnow and Egner 1999) reported in their binding assay of the estrogen receptor alpha,

a binding affinity of 0.005 nM for the substrate; 17β-estradiol. This research involved the invention of a technological approach that was able determine micro to nano molarity levels of 17β-estradiol with application of a highly substrate-specific ER-α (i.e. in this context the designation; substrate refers to the ligand or the analyte molecule) associated with very high sensitivity. The distinct electrochemical induced signals obtained for the ER-α-based biosensors were associated with the specific functional groups present at the ligand specific binding domain active site's amino acid sequence structure of the ER-α, which was formerly verified by the high binding affinity and efficiency with the target analyte; 17β-estradiol (E2).

Chapter 7 BIBLIOGRAPHY

1. Adhikar, U. and S. Scheiner (2013). "First Steps in Growth of a Polypeptide toward β-Sheet Structure." *Journal of Physical Chemistry B* **117**(39): 11575-11583.

2. Alberts, B., et al. (2002). The Lipid Bilayer. *Molecular Biology of the Cell*. N. Y. G. Science.

3. Alkhatib, A. and A. Nayfeh (2013). "A Complete Physical Germanium-on-Silicon Quantum Dot Self-Assembly Process." *Sci. Rep.* **3**.

4. Allen, O. J. (1964). "The Biosynthesis and Metabolism of Carotenoids and Retinol (Vitamin A)." *Journal of Lipid Research*: 281-299.

5. Anderson, I. E., et al. (2010). "Silanization of Low-Temperature-Plasma Synthesized Silicon Quantum Dots for Production of a Tunable, Stable, Colloidal Solution." *American Chemical Society* **116**: 3979-3987.

6. Ando, H., et al. (2001). "Signal transduction pathways and transcription factors involved in the gonadotropin-releasing hormone-stimulated gonadotropin subunit gene expression." *Comparative Biochemistry and Physiology Part B: Biochemistry and Molecular Biology* **129**(2–3): 525-532.

7. Andriole, E. J., et al. (2006). "Proton Affinity of Canavanine and Canaline, Oxyanalogues of Arginine and Ornithine, from the Extended Kinetic Method." *Journal of Physical Chemistry A* **110**(40): 11501-11508.

8. Angelika Krebs, et al. (2003). "The Three-dimensional Structure of Bovine Rhodopsin Determined by Electron Cryomicroscopy." *Journal of Biological Chemistry* **278**(50).

9. Asaka, M.-A., et al. (2007). "17b-Estradiol Antagonizes the Down-Regulation of Endothelial Nitric-Oxide Synthase and GTP Cyclohydrolase I by High Glucose: Relevance to Postmenopausal Diabetic Cardiovascular Disease." *Journal of Pharmacology and Experimental Therapeutics* **320**(2): 591-598.

10. Ataide, S. F. and M. Ibba (2006). "Small Molecules: Big Players in the Evolution of Protein Synthesis." *ACS Chemical Biology* **1**(5): 285-297.

11. Aumo, J., et al. (2005). "Hydrogenation of Citral over Activated Carbon Cloth Catalyst." *Industrial & Engineering Chemistry Research* **44**(14): 5285-5290.

12. Ba, Z. F., et al. (2007). "17b-Estradiol Modulates Vasoconstriction Induced by Endothelin Following Trauma-Hemorrhage." *American Physiological Society: Heart and Circulatory Physiology* **292**: 245-250.

13. Babine, R. E. and S. L. Bender (1997). "Molecular Recognition of Protein−Ligand Complexes: Applications to Drug Design." *Chemical Reviews* **97**(5): 1359-1472.

14. Bailey, R. E. and S. Nie (2003). "Alloyed Semiconducting Quantum Dots: Tuning the Optical Properties without Changing the Size." *Journal of American Chemical Society* **125**: 7100-7106.

15. Baker, D. R. and P. V. Kamat (2010). "Tuning the Emission of CdSe Quantum Dots by Controlled Trap Enhancement." *Langmuir* **26**(13): 11272-11276.

16. Bard, A. J. and L. R. Faulkner (2001). *Electrochemical Methods, Fundamentals and Applications.* New York, Wiley.

17. Barendt, P. A., et al. (2013). "Streamlined Protocol for mRNA Display." *ACS Combinatorial Science* **15**(2): 77-81.

18. Beltyukova, S. V. and A. V. Egorova (1998). "Terbium chelates for Fluorescence Immunoassays." *Journal of Pharmaceutical and Biomedical Analysis* **18**: 267-270.

19. Benner, S. A., et al. (1997). "Bona Fide Predictions of Protein Secondary Structure Using Transparent Analyses of Multiple Sequence Alignments." *Chemical Reviews* **97**(8): 2725-2844.

20. Berg, J., et al. (2002). *Biochemistry.* New York, W H Freeman.

21. Biswas, N., et al. (2007). "Structure and conformation of the disulfide bond in dimeric lung surfactant peptides SP-B1–25 and SP-B8–25." *Biochimica et Biophysica Acta (BBA) - Biomembranes* **1768**(5): 1070-1082.

22. Bolstad, H. M., et al. (2010). "Proteomic Analysis of Protein−Protein Interactions within the Cysteine Sulfinate Desulfinase Fe−S Cluster Biogenesis System." *Journal of Proteome Research* **9**(10): 5358-5369.

23. Bulgariu, L. and D. Bulgariu (2008). "Self-Assembled Monolayer of Thiols on Gold Electrodes Prepared by Gold Electro-chemical Deposition on Platinum Wire." *Chemical Bulletin* **53**(57): 1-2.

24. Burris, T. P., et al. (2013). "Nuclear Receptors and Their Selective Pharmacologic Modulators." *Pharmacological Rewievs* **67**: 710-778.

25. Campbell, C. G., et al. (2006). "Biologically directed environmental monitoring fate and transport of estrogenic endocrine disrupting compounds in water: A review, ." *Chemosphere* **65**: 1265-1280.

26. Canada, R. G. and P. D. N. (1998). "Binding of Terbium and Cisplatin to C13* Human Ovarian Cancer Cells using Time-resolved Terbium Luminescence." *Biochica et Biophyica Acta* **1448**: 85-98.

27. Carugo, O. and K. D. Carugo (2013). "A proteomic Ramachandran plot (PRplot)." *Amino Acids* **44**: 781–790.

28. Catak, S., et al. (2008). "Computational Study on Nonenzymatic Peptide Bond Cleavage at Asparagine and Aspartic Acid." *Journal of Physical Chemistry A* **112**(37): 8752-8761.

29. Chan, J. M., et al. (2010). Polymeric Nanoparticles for Drug Delivery. *Cancer Nanotechnolgy, Methods in Molecular Biology*. **624:** 163-175.

30. Charles R. Sanders Biomolecular Ligand-Receptor Binding Studies: Theory, Practice, and Analysis, Dept. of Biochemistry, Vanderbilt University.

31. Chen, H.-C., et al. (2009). "Determination of estrogenic compounds in wastewater using liquid chromatography-tandem mass spectrometry with electrospray and atmospheric pressure photoionization following desalting extraction." *Chemosphere* **74**(4): 508-514.

32. Chen, R. F. (1967). "Fluorescence Quantum Yields of Tryptophan and Tyrosine." *Analytical Letters* **1**(1): 35-42.

33. Cherkouk, C., et al. (2011). "Bioconjugation of the Estrogen Receptor hERa to a Quantum Dot dye for a Controlled Immobilization on a SiO2 surface." *Journal of Colloid and Interface Science* **355**: 442-447.

34. Cheskis, B. J., et al. (1997). "Estrogen Receptor Ligands Modulate Its Interaction with DNA." *Journal of Biological Chemistry* **272**: 11384-11391.

35. Choe, H.-W., et al. (2011). "Transmembrane signaling by GPCRs: Insight from rhodopsin and opsin structures." *Neuropharmacology* **60**(1): 52-57.

36. Chunyou, C., et al. (2008). "GTP Hysdroxylase I and Tyrosine Hydroxlase Gene Mutation in Familia and Spradic Dopa-Responsive Dystonia Patients." *PLOS ONE* **8**(6): 1-5.

37. Coates, J. (2000). Interpretation of Infrared Spectra, A Practical Approach. *Encyclopedia of Analytical Chemistry*. R. A. Meyers. Coates Consulting, Newton, USA, John Wiley & Sons Ltd.

38. Cooper, G. (2000). *The Cell: A Molecular Approach S.*

39. Craig, B., et al. (1996). "Double Transduction wuth GTP Hydroxylase I and Tyrosine Hydroxylase Is Necessary for Sponteneous Synthesis of L-DOPA Primary Fibroblast." *The Journal of Neuroscience* **16**(14): 4449-4456.

40. Creighton, T. E. (1993). Proteins, Structures and Molecular Properties.

41. Croft, W., et al. (2013). "A Physiologically Required G Protein-coupled Receptor (GPCR)-Regulator of G Protein Signaling (RGS) Interaction That Compartmentalizes RGS Activity." *Journal of Biological Chemistry* **288**(38): 27327-27342.

42. Darby, N. J. and T. E. Creighton (1995). "Functional properties of the individual thioredoxin-like domains of protein disulfide isomerase." *Biochemistry* **34**(37): 11725-11735.

43. DasGupta, D., et al. (2015). "From Ramachandran Maps to Tertiary Structures of Proteins." *The Journal of Physical Chemistry B* **119**(34): 11136-11145.

44. Davis, T., et al. (2000). "Histone Deacetylase Inhibitors Decrease Proliferation and Modulate Cell Cycle Gene Expression in Normal Mammary Epithelial Cells." *Clinical Cancer Research* **6**: 4334-4342.

45. Dechering, K., et al. (2000). "Estrogen receptors alpha and beta: two receptors of a kind?" *Curr Med Chem* **7**(5): 561-576.

46. DeGraw, A. J., et al. (2010). "Prediction and Evaluation of Protein Farnesyltransferase Inhibition by Commercial Drugs." *Journal of Medicinal Chemistry* **53**(6): 2464-2471.

47. Déméné, H. and I. P. Sugàr (1999). "Protein Conformation and Dynamics. Effects of Crankshaft Motions on 1H NMR Cross-Relaxation Effects." *The Journal of Physical Chemistry A* **103**(24): 4664-4672.

48. Ding, S.-Y., et al. (2003). "Quantum Dot Molecules Assembled with Genetically Engineered Proteins." *Nano Letters* **3**(11): 1581-1585.

49. Dominak, L. M., et al. (2010). "Microcompartmentation in Artificial Cells: pH-Induced Conformational Changes Alter Protein Localization." *Langmuir* **26**(8): 5697-5705.

50. Duellman, S. J., et al. (2010). "A novel steroidal inhibitor of estrogen-related receptor a (ERRa)." *Biochemical Pharmacology* **80**: 819-826.

51. Ebrahimi, F. A. W. and A. Chess (1998). "Olfactory G proteins: Simple and complex signal transduction." *Current Biology* **8**(12): 431-433.

52. Eric, V. and B. Mark (2009). "Amide bond formation: beyond the myth of coupling reagents." *The Royal Society of Chemistry* **38**: 606-631.

53. Fischer, G. and F. X. Schmid (1990). "The mechanism of protein folding. Implications of in vitro refolding models for de novo protein folding and translocation in the cell." *Biochemistry* **29**(9): 2205-2212.

54. Fotouhi, L., et al. (2012). "Electrochemical Behaviour and Voltammetric Determination of Sulfaguanidine at a Glassy Carbon Electrode." *International Journal of Electrochemical Sciences:* 3919 - 3928.

55. Gadaleta, R. M. and L. Magnani (2014). "Nuclear Receptors and Chromatin: An Inducible Couple." *Journal of Molecular Endocrinology* **52**(2): 137-149.

56. Garcia-Raso, A., et al. (1986). "Oxidation of .alpha.-amino acids and .alpha.-hydroxy acids by Fremy's salt. A model for oxidases?" *The Journal of Organic Chemistry* **51**(22): 4285-4287.

57. Garidou, L., et al. (2004). "Estrogen Receptor a Signaling inInflammatory Leukocytes Is Dispensable for 17b-Estradiol-Mediated Inhibition of Experimental Autoimmune Encephalomyelitis." *Journal of Immunology* **173**: 2435-2442.

58. Ghanemi, A. (2015). "Targeting G protein coupled receptor-related pathways as emerging molecular therapies." *Saudi Pharmaceutical Journal* **23**(2): 115-129.

59. Gill, R., et al. (2008). "Semiconductor Quantum Dots for Bioanalysis." *Angewandte Chemie* **47**: 7602-7625.

60. Gitti, R. K., et al. (2005). "Backbone Dynamics of the Olfactory Marker Protein As Studied by 15N NMR Relaxation Measurements." *Biochemistry* **44**(28): 9673-9679.

61. Goèmez-Hens, A. and M. P. Aguilar-Caballos (2002). "Terbium-Sensitized Luminescence: A Selective and Versatile Analytical Approach." *Trends in Analytical Chemistry* **21**(2): 131-141.

62. Gustafsson, J.-A. (1999). "Estrogen Receptor – A New Dimension in Estrogen Mechanism of Action." *Journal of Endocrinology* **163**: 379-383.

63. Gustafsson, J.-A. (2016). "Historical overview of nuclear receptors." *The Journal of Steroid Biochemistry and Molecular Biology* **157**: 3-6.

64. Gutkind, J. S. (1998). "The Pathways Connecting G Protein-coupled Receptors to the Nucleus through Divergent Mitogen-activated Protein Kinase Cascades." *The Journal of Biological Chemistry* **273**: 1839-1842.

65. Held, C., et al. (2011). "Measuring and Modeling Activity Coefficients in Aqueous Amino-Acid Solutions." *Industrial & Engineering Chemistry Research* **50**(1): 131-141.

66. Heldring, N., et al. (2007). "Estrogen Receptors: How Do They Signal and What Are Their Targets." *Physiological Reviews* **87**(3): 905-931.

67. Hickey, S. G., et al. (2008). "Size and Shape Control of Colloidally Synthesized IV-VI Nanoparticulate Tin(II) Sulfide." *Journal of the American Chemical Society* **130**: 14978-14980.

68. Hildebrandt, N. (2011). "Biofunctional Quantum Dots: Controlled Conjugation for Multiplexed Biosensors." *Americal Chemical Society, Nano* **5**(7): 5286-8290.

69. Hill, S. M., et al. (1989). "Estrogen Receptor Expression in Human Breast Cancer Associated with an Estrogen Receptor Gene Restriction Fragment Length Polymorphism." *Cancer Research* **49**: 145-148.

70. Ho, B. K. and R. Brasseur (2005). "The Ramachandran plots of glycine and pre-proline." *BMC Structural Biology* **5**(1): 1-11.

71. Ivanov, I., et al. (2006). "Relative pKa Values from First-Principles Molecular Dynamics: The Case of Histidine Deprotonation." *Journal of Physical Chemistry B* **110**(12): 6565-6371.

72. Iwunze, M. O. (2007). "The characterization of the fluorescence of l-histidine in simulated body fluid." *Journal of Photochemistry and Photobiology A: Chemistry* **186**(2–3): 283-289.

73. Jackson, R. F. W., et al. (1992). "Preparation of enantiomerically pure protected 4-oxo .alpha.-amino acids and 3-aryl .alpha.-amino acids from serine." *The Journal of Organic Chemistry* **57**(12): 3397-3404.

74. Jensen, E. V. and V. C. Jordan (2003). "The Estrogen Receptor: A Model for Molecular Medicine." *Clinical Cancer Research* **9**: 1980-1989.

75. Julian, R. R., et al. (2002). "Cooperative Salt Bridge Stabilization of Gas-Phase Zwitterions in Neutral Arginine Clusters." *Journal of Physical Chemistry* **106**(1): 32-34.

76. Kafka, A. P., et al. (2009). "Histidine Residues in the Peptide d-Lys6-GnRH: Potential for Copolymerization in Polymeric Nanoparticles." *Molecular Pharmaceutics* **6**(5): 1483-1491.

77. Karas, R. H., et al. (2001). "Effects of Estrogen on the Vascular Injury Response Receptor a,b (Double) Knockout Mice." *Journal of the American Heart Association* **89**: 534-539.

78. Klinge, C. M., et al. (1997). "Binding of type II nuclear receptors and estrogen receptor to full and half-site estrogen response elements in vitro." *Nucleic Acids Research* **25**(10): 1903-1912.

79. Kobilka, B. (2013). "The Structural Basis of G-Protein-Coupled Receptor Signaling." *Angewandte Chemical International Letters* **52**: 6380-6388.

80. Kobilka, B. K. (2007). "G Protein Coupled Receptor Structure and Activation." *Biochim Biophysc Acta* **1768**(4): 794-807.

81. Kong, Y., et al. (2011). "Identification of Aspartic Acid Enantiomers Based on Molecularly Imprinted Polyaniline." *Chinese Journal of Chemistry* **29**(12): 2659-2663.

82. Korlann, S. D., et al. (2005). "Chemical Tuning of the Electronic Properties in a Periodic Surfactant-Templated Nanostructured Semiconductor." *Journal of the American Chemical Society* **127**: 12516-12527.

83. Kovalenko, M. V., et al. (2004). "Spectral, Optical and Photocatalytic Charecteristics of Quantum-Sized Particle of CdTe." *Theoretical and Experimetal Chemistry* **40**(4).

84. Kuma, B. R. and T. S. Rao (2012). "AFM Studies on Surface Morphology, Topography and Texture of Nanostructured Zinc Aluminium Oxide Thin Films." *Digest Journal of nanomaterial and Biostructures* **7**(4): 1881-1889.

85. Kumar, P. and K. Singh (2009). "Wurtzite ZnSe quantum dots: Synthesis, Characterization and PL Properties." *Journal of Optoelectronic and Biomedical Materials* **1**(1): 59-69.

86. Kumara, S., et al. (2011). "Doping studies of Tb (terbium) and Cu (copper) on CdSe Nanorods." *Colloids and Surfaces A: Physicochemical and Engineering Aspects* **389**: 1-5.

87. Lalko, J., et al. (2007). "Fragrance material review on β-ionone." *Food and Chemical Toxicology* **45**(1, Supplement 1): S241-S247.

88. Leifeld, O., et al. (1999). "Self Organized Growth of Ge Quantum Dots on Si(001) Substrates Induced by Sub-Monolayer C coverages." *Nanotechnology* **10**: 122-126.

89. Levin, E. R. (2001). "Genome and Hormones: Gender Differences in Physiology Invited Review: Cell localization, physiology, and Nongenomic Actions of Estrogen Receptors." *Journal of Applied Physiology* **91**: 1860-1867.

90. Li, H. (2008). Synthesis and Characterization of Aqueous Quantum Dots for Biomedical Applications, Drexel University.

91. Li, L. S., et al. (2004). "High Quality ZnSe and ZnSNanocrystals Formed by Activating Zinc Carboxylate Precursors." *Nano Letters* **4**(11): 2261-2264.

92. Li , L. S., et al. (2007). "Room temperature synthesis of HgTe nanocrystals." Journal of *Colloid and Interface Science* **308**: 254-257.

93. Li, S. and M. Hong (2011). "Protonation, Tautomerization, and Rotameric Structure of Histidine: A Comprehensive Study by Magic-Angle-Spinning Solid-State NMR." *Journal of American Chemical Society* **133**(5): 1534-1544.

94. Li, T., et al. (2002). "Effect of the Intermolecular Disulfide Bond on the Conformation and Stability of Glial Cell Line-Derived Neurotrophic Factor." *Protein Engineering* **15**(1): 59-64.

95. Lin, K.-L. (2014). "Phase Identification Using Series of Selected Area Diffraction Patterns and Energy Dispersive Spectrometry within TEM." *Microscopy Research* **2**: 57-66.

96. Little, W., et al. (2014). "Structural origin of light emission in germanium quantum dots." *Sci. Rep.* **4**.

97. Liu, Z., et al. (2007). "Effects of Buffer Layers on the Stress and Morphology of GaN epilayer Grown on Si Substrate by MOCVD." *Journal of Crystal Growth* **298**: 281-283.

98. Lodish, H., et al. (2000). *Molecular Cell Biology. 4th edition.* ; 2000. Section 17.3.

99. Marques, F. A. M., et al. (2009). "Electric Field Effects on the Carrier Migration in Self-assembled InAs/GaAs Quantum Dots." *Microelectronics Journal* **40**: 838-840.

100. Mattram, C. (1990). "Electrode Material for Electrosynthesis." *Chem. Rev* **90**: 837-865.

101. McMurry, J., et al. (2013). *Fundamentals of General, Organic, and Biological Chemistry.*

102. Michalet, X., et al. (2006). "Single-Molecule Fluorescence Studies of Protein Folding and Conformational Dynamics." *Chemical Reviews* **106**(5): 1785-1813.

103. Mikkolaa, T. S. and T. B. Clarksona (2002). "Estrogen Replacement Therapy, Atherosclerosis, and Vascular Function." *Cardiovascular Research* **53**: 605-619.

104. Mishra, N. C. (2010). Introducion to Proteomics, Principles and Application, WilleySeries in Methods of Biochemical Analysis**:** 39.

105. Mittendorf, K. F., et al. (2012). "Tailoring of Membrane Proteins by Alternative Splicing of Pre-mRNA." *Biochemistry* **51**(28): 5541-5556.

106. Moller, W. and R. Amons (1985). "Phosphate-Binding Sequence in Nucleotide-Binding Poteins." *FEBS Letters* **186**(1).

107. Moreels, I., et al. (2008). *Colloidal Semiconductor Quantum Dots: From synthesis to Photonic Applications*. IEEE/LEOS Benelux Chapter.

108. Mueller-Fahrnow, A. and U. Egner (1999). "Ligand-Binding Domain of Estrogen Receptors." *Pharmaceutical Biotechnology*: 550-556.

109. Munro, A. M., et al. (2008). "Colloidal CdSe Quantum dot Electroluminescence: Ligands and Light-emitting Diodes." *Microchimica Acta* **160**: 345-350.

110. Na, C. and T. M. Olson (2007). "Relative Reactivity of Amino Acids with Chlorine in Mixtures." *Environmental Science & Technology* **41**(9): 3220-3225.

111. Nagy, P. I. and B. Noszál (2000). "Theoretical Study of the Tautomeric/Conformational Equilibrium of Aspartic Acid Zwitterions in Aqueous Solution." *Journal of Physical Chemistry A* **104**(29): 6834-6843.

112. Ndangili, P. M., et al. (2010). "A potential masking approach in the detection of dopamine on 3-mercaptopropionic acid capped ZnSe quantum dots modified gold electrode in the presence of interferences." *Journal of Electroanalytical Chemistry* **643**: 77–81.

113. Ndangili, P. M., et al. (2011). "3-Mercaptopropionic acid capped ZnSe quantum dot-cytochrome P450 3A4 enzyme biotransducer for 17β-estradiol." *Journal of Electroanalytical Chemistry* **653**(1–2): 67-74.

114. Ndangili, P. M., et al. (2011). "3-Mercaptopropionic acid capped ZnSe quantum dot-Cytochrome P450-3A4 enzyme biosensor for 17β-estradiol." *Journal of Electroanalytical Chemistry* **653**: 67-74.

115. Neghmouche, N. S. and T. Lanez (2013). "Calculation of Diffusion Co-Efficient and Layer Thickness for Oxidation of Ferrocene Using Voltammetry Techniques." *International Journal of Chemical Sciences,* **1**(1).

116. Norako, M. E., et al. (2012). "Synthesis and Characterization of Wurtzite-Phase Copper Tin Selenide Nanocrystals." *Journal of the American Chemical Society* **134**: 23-26.

117. Northrop, R. B. (2010). *Signals and Systems in Biomedical Engineering*. Boca Raton, Tylor and Francis Group.

118. Nose, K., et al. (2009). "Colloidal Synthesis of Ternary Copper Indium Diselenide Quantum Dots and Their Optical Properties." *Journal of Physical Chemistry* **113**: 3455-3460.

119. Nuedling, S., et al. (1999). "17b-Estradiol Stiimulates Expression of Endothelial and Inducible NO Synthase in Rat Myocardium In-Vitro and In-Vivo." *Cardiovascular Research* **43**: 666-674.

120. Nxusani, E., et al. (2012). "3-Mercaptopropionic Acid Capped Ga_2Se_3nanocrystal-CYP3A4 Biosensor for the Determination of 17-Alpha-Ethinyl Estradiolin Water." *Nano Hybrids* **1**: 1-22.

121. Odoi, M. Y., et al. (2006). "Observation of Enhanced Energy Transfer in Individual Quantum Dot-Oligophenylene Vinylene Nanostructures." *Journal of the American Chemical Society* **128**(11): 3506-3507.

122. Oedzene, M. and Karagozler (1999). "Electrochemical Preparation and Sensor Properties of Conducting Polyaniline Films." *Turk J Chem* **23**: 89-98.

123. Ohno, H. and K. Fukumoto (2007). "Amino Acid Ionic Liquids." *Accounts of Chemical Research* **40**(11): 1122-1129.

124. Okimoto, N., et al. (2004). "Cooperative Motions of Protein and Hydration Water Molecules: Molecular Dynamics Study of Scytalone Dehydratase." *Journal of the American Chemical Society* **126**(40): 13132-13139.

125. Otero, E. and S. G. Urquhart (2006). "Nitrogen 1s Near-Edge X-ray Absorption Fine Structure Spectroscopy of Amino Acids: Resolving Zwitterionic Effects." *Journal of physical Chemistry A* **110**(44): 12121-12128.

126. Palczewski, K. (2006). "G Protein–Coupled Receptor Rhodopsin." *Annual Review of Biochemistry* **75**(1): 743-767.

127. Pan, Y., et al. (2009). "Structural Characterization of an Integral Membrane Protein in Its Natural Lipid Environment by Oxidative Methionine Labeling and Mass Spectrometry." *Analytical Chemistry* **81**(1): 28-35.

128. Pare, G., et al. (2002). "Estrogen Receptor-a Mediates the Protective Effects of Estrogen Against Vascular Injury." *Circulation Research* **90**: 1087-1092.

129. Pawlak, M., et al. (2012). "General molecular biology and architecture of nuclear receptors." *Current Topics in Medicinal Chemistry* **12**(6): 486-504.

130. Pearce, S. T. and V. C. Jordan (2004). "The biological role of estrogen receptors alpha and beta in cancer." *Crit Rev Oncol Hematol* **50**(1): 3-22.

131. Petucci, C., et al. (2010). "Trace LC/MS/MS quantitation of 17β-estradiol as a biomarker for selective estrogen receptor modulator activity in the rat brain." *Journal of Mass Spectrometry* **45**(1): 65-71.

132. Pike, A. C. W., et al. (1999). "Structure of the Ligand-Binding Domain of Oestrogen Receptor Beta in the Presence of a Partial Agonist and a Full Antagonist." *European Molecular Biology Organization* **18**(17): 4608-4618.

133. Plošnik, A., et al. (2015). "Computational study of binding affinity to nuclear receptors for some cosmetic ingredients." *Chemosphere* **135**(0): 325-334.

134. Plošnik, A., et al. (2015). "Computational study of binding affinity to nuclear receptors for some cosmetic ingredients." *Chemosphere* **135**: 325-334.

135. Pushpendra, K. and S. Kedar (2009). "ZnSe quantum dots: Synthesis, characterization and PL properties, Journal of optoelectronic and Biomedical Materials." *Wurtzite **1***(1): 59 - 69.

136. Read, F. H. (1980). *Electromagnetic Radiation.* Chichester, New York, John Wiley & Sons.

137. Rehm, H. (2006). Protein Biochemistry and Proteomics.

138. Remko, M., et al. (2008). "Effect of Metal Ions (Li+, Na+, K+, Mg2+, Ca2+, Ni2+, Cu2+, and Zn2+) and Water Coordination on the Structure and Properties of l-Arginine and Zwitterionic l-Arginine." *Journal of Physical Chemistry A* **112**(13): 7652-7661.

139. Reynolds, C. H. (2014). "Protein–Ligand Cocrystal Structures: We Can Do Better." *ACS Medicinal Chemistry Letters* **5**(7): 727-729.

140. Righetti, H. P. G. (2005). Proteomics Today, Protein Assesment and Biomakers Using Mass Spectrometry, Willey Intersciences Series on Mass Spectrometry.

141. Rios, A., et al. (2000). "Formation and Stability of Organic Zwitterions in Aqueous Solution: Enolates of the Amino Acid Glycine and Its Derivatives." *Journal of the American Chemical Society* **122**(39): 9373-9385.

142. Roos, E. C., et al. (1993). "Synthesis of .alpha.-substituted .alpha.-amino acids via cationic intermediates." *The Journal of Organic Chemistry* **58**(12): 3259-3268.

143. Saidel, L. J., et al. (1952). "The absorption Spectra of Amino Acids in the Region Two Hundred to Two Hundred Millimicrons." *Journal of Biological Chemistry* **197**: 285-291.

144. Schmid, F.-X. (2001). Biological Macromolecules UV-visible Spectrophotometry. *Encyclopedia of Life Sciences,* Macmillan Publishers Ltd, Nature Publishing Group.

145. Scott D., K., et al. (2005). "Chemical Tuning of the Electronic Properties in a Periodic Surfactant-Templated Nanostructured Semiconductor." *Journal of American Chemical Society* **127**: 12516-12527.

146. Shanzer, A., et al. (1979). "Stereospecific synthesis of .alpha.-amino-.beta.-hydroxy acids." *The Journal of Organic Chemistry* **44**(22): 3967-3969.

147. Shao, S. and R. S. Hegde (2011). "Membrane Protein Insertion at the Endoplasmic Reticulum." *Annu. Rev. Cell Dev. Biol* **27**(25–56).

148. Shapell, N. W., et al. (2010). "Comparative Biological effects and Potency of 17a- and 17b-Estradiol in Fathead Minnows." *Aquatic Toxicology* **100**: 1-8.

149. Sharma, M. and S. Yashonath (2007). "Size dependence of solute diffusivity and Stokes Einstein Relationship: Effects of van de-Waals Interaction." *Diffusion fundamentals* **7**: 11.11-11.15.

150. Shen, F., et al. (2011). "Photocatalytic Activity of TiO_2 Nanoparticles Sensitized by $CuInS_2$ Quantum Dots." *Journal of the American Chemical Society* **50**: 9131-9137.

151. Shi, L., et al. (2007). "Luminescent Quantum Dots Fluorescence Resonance Energy Transfer-Based Probes for Enzymatic Activity and Enzyme Inhibitors." *Analytical Chemistry* **79**: 208-214.

152. Shonle, H. A. and H. H. Mitchell (1920). "THE ESTERIFICATION OF ALPHA AMINO ACIDS." *Journal of the American Chemical Society* **42**(6): 1265-1277.

153. Singh, K. P., et al. (2009). "Quantum dot doped solid polymer electrolyte for device application." *Electrochemistry Communications* **11**: 1247–1250.

154. Skafar, D. F. and S. Koide (2006). "Understanding the Human Estrogen Receptor-Alpha Using Targeted Mutagenesis." *Molecular and Cellular Endocrinolgy* **246**: 83-90.

155. Soltani, N., et al. (2012). "Band Gap of Cubic and Hexagonal CdS Quantum Dots-Experimental and Theoretical Studies." *Chalcogenide Letters* **9**(7): 321-328.

156. Song, J., et al. (2008). "Electrochemical determination of estradiol using a poly(l-serine) film-modified electrode." *Journal of Applied Electrochemistry* **38**(6): 833-836.

157. Stokes, K., et al. (2004). "Estrogen Response Element and the Promoter Context of the Human and Mouse Lactoferrin Genes Influence Estrogen Receptor-Mediated Transactivation Activity in Mammary Gland Cells." *Journal of Molecular Endocrinology* **33**: 315-334.

158. Stouwdam, J. W. and R. A. J. Janssen (2008). "Red, Green, and Blue Quantum Dot LEDs with Solution Processable ZnO Nanocrystal Electron Injection Layers." *Royal Society of Chemistry* **18**: 1889-1894.

159. Strehlow, W. H. and E. L. Cook (1973). "Compilation of Energy Band Gaps in Elemental and Binary Compound Semiconductors and Insulators." *Journal of Physical and Chemical Reference Data* **2**(1): 163-200.

160. Strohmeier, M., et al. (2003). "Accurate C13 and N15 Chemical Shift and N14 Quadrupolar Coupling Constant Calculations in in Amino Acid Crystals: Zwitterionic, Hydrogen-Bonded Systems." *Journal of Physical Chemistry* **107**: 7629-7642.

161. Strug, I., et al. (2012). "IR based Protein & Peptide Quantitation." *Assay Tutorials* **32**(13).

162. Sugase, K., et al. (2007). "Mechanism of Coupled Folding and Binding of an Intrinsically Disordered Protein." *Nature* **447**.

163. Sun, K., et al. (2009). "Applications of Colloidal Quantum Dots." *Microelectronics Journal* **40**: 644-649.

164. Sundarrajan, C., et al. (1999). "Association of Oestrogen Receptor Gene Polymorphisms with Outcome of Ovarian Stimulation in Patients Undergoing IVF." *Molecular Human Reproduction* **5**(9): 797-802.

165. Suo, B., et al. (2010). "Poly (vinyl alcohol) thin film filled with CdSe-ZnS quantum dots: Fabrication, characterization and optical properties." *Materials Chemistry and Physics* **119**(1-2): 237-242.

166. Suzuki, M., et al. (1973). "Synthesis of amino acids and related compounds. 6. New convenient synthesis of .alpha.-C-acylamino acids and .alpha.-amino ketones." *The Journal of Organic Chemistry* **38**(20): 3571-3575.

167. Taha, E. A., et al. (2007). "Fluorimetric Determination of Some Sulfur Containing Compounds Through Complex Formation with Terbium (Tb+3) and Uranium (U+3)." *Journal of Fluorescence* **17**: 293-300.

168. Tanenbaum, D. M., et al. (1998). "Crystallographic comparison of the estrogen and progesterone receptor's ligand binding domains." *Proceedings of the National Academy of Sciences of the United States of America* **95**(11): 5998-6003.

169. Teale, F. W. J. and G. Weber (1957). "Ultraviolet fluorescence of the aromatic amino acids." *Biochemical Journal* **65**(3): 476-482.

170. Tengvall, P., et al. (2003). "Preparation of Multilayer Plasma Protein Films on Silicon by EDC/NHS Coupling Chemistry." *Colloids and Surfaces B: Biointerfaces* **28**: 261-272.

171. Teresa, M., et al. (2002). "High Probability of Disrupting a Disulphide Bridge Mediated by an Endogenous Excited Tryptophan Residue." *Protein Science* **11**: 588-600.

172. Tetenbaum, J. and L. M. Miller (2001). "A New Spectroscopic Approach to Examining the Role of Disulfide Bonds in the Structure and Unfolding of Soybean Trypsin Inhibitor." *Biochemistry* **40**(40): 12215-12219.

173. Tian, Z., et al. (2009). "Are Carboxyl Groups the Most Acidic Sites in Amino Acids? Gas-Phase Acidities, Photoelectron Spectra, and Computations on Tyrosine, p-Hydroxybenzoic Acid, and Their Conjugate Bases." *Journal of American Chemical Society* **131**(3): 1174-1181.

174. Tilley, D. G. and H. Rockman (2011). "G Protein–Dependent and G Protein–Independent Signaling Pathways and Their Impact on Cardiac Function." *Circulation Reaserch* **109**: 217-230.

175. Tsujishita, H., et al. (1993). "Potential-scaled molecular dynamics and potential annealing: effective conformational search techniques for biomolecules." *Journal of Physical Chemistry* **97**(17): 4416-4420.

176. Valko, M., et al. (2006). "Free Radicals, Metals and Antioxidants in Oxidative Stress-Induced Cancers." *Chemico-Biological Interactions* **160**: 1-40.

177. Vo-DinH, T. (2010). Proteins Nanotechnology, Protols, Instrumentation and Applications, Humana Press Inc.

178. Walling, M. A. and J. A. Novak (2009). "Quantum Dots for Live Cell and In Vivo Imaging." *Int. J. Mol.Sci* **10**: 441-491.

179. Walsh, C. (1979). Enzymic Reaction Mechanisms. San Franscico, W H Freeman and Company.

180. Walsh, G. (2002). Biochemistry and Biotechnology, John Willey & Sons.

181. Walter, P., et al. (1985). "Cloning of the Human Estrogen Receptor cDNA." *Biochemistry* **82**: 7889-7893.

182. Wang, K. L., et al. (2007). "Ge/Si Self-Assembled Quantum Dots and Their Optoelectronic Device Applications." *Precceding of the Institute of Electrical and Electronics Engineers* **95**: 1866-1883.

183. Wang, Y., et al. (2008). "Mercaptopyridine Surface-Functionalized CdTe Quantum Dots with Enhanced Raman Scattering Properties." *Journal of Physical Chemistry* **112**: 996-1000.

184. Wang, Y. Q., et al. (2002). "Engineering Vertically Aligned InAs/GaAs Quantum Dot Structures via Anion Exchange." *Solid State Communications* **122**: 553-556.

185. Whitelegge, J. P. (2013). "Integral Membrane Proteins and Bilayer Proteomics." *Analytical Chemistry* **85**(5): 2558-2568.

186. Wu, X. and S. Wang (2001). "Helix Folding of an Alanine-Based Peptide in Explicit Water." *The Journal of Physical Chemistry B* **105**(11): 2227-2235.

187. Xu, C., et al. (2015). "Library of Antifouling Surfaces Derived From Natural Amino Acids by Click Reaction." *ACS Applied Materials & Interfaces* **7**(31): 17337-17345.

188. Yanagawa, H. (2013). "Exploration of the Origin and Evolution of Globular Proteins by mRNA Display." *Biochemistry* **52**(22): 3841-3851.

189. Yang, W. Y., et al. (2003). "On the Extended β-Conformation Propensity of Polypeptides at High Temperature." *Journal of the American Chemical Society* **125**(52): 16220-16227.

190. Yang, Z. and H.-T. Chang (2010). "CdHgTe and CdTe Quantum Dot Solar Cells Displaying an Energy Conversion Efficiency Exceeding 2%." *Solar Energy Materials & SolarCells* **94**: 2046-2051.

191. Ye, X., et al. (2003). "Investigations of Heme Protein Absorption Line Shapes, Vibrational Relaxation, and Resonance Raman Scattering on Ultrafast Time Scales." The Journal of *Physical Chemistry A* **107**(40): 8156-8165.

192. Yoon, S. H., et al. (2010). "Estrogen Receptor a Gene Polymorphisms in Patients with Idiopathic Premature Ovarian Failure." *Human Reproduction* **25**(1): 283-287.

193. Yu, W. W., et al. (2006). "Water-Soluble Quantum Dots for Biomedical Applications." *Biochemical and Biophysical Research Communications* **348**: 781-786.

194. Yu, W. W., et al. (2006). "Water-soluble quantum dots for biomedical applications." *Biochemical and Biophysical Research Communications* **348**: 781–786.

195. Zhang, H., et al. (2003). "The Influence of Carboxyl Groups on the Photoluminescence of Mercaptocarboxylic Acid-Stabilized CdTe Nanoparticles." *Journal of Physical Chemistry B* **107**: 8-13.

196. Zhang, H. J., et al. (1997). "Luminescence Properties of the Langmuir-Blodgett Film of Terbium(III) Stearoylanthranilate." *Thin Solid Films* **310**: 274-278.

197. Zhao, Y., et al. (2004). "Proteomic Analysis of Integral Plasma Membrane Proteins." *Analytical Chemistry* **76**(7): 1817-1823.

198. Zhong, Z., et al. (2004). "The Surface Chemistry of Au Colloids and Their Interactions with Functional Amino Acids." *Journal of Physical Chemistry B.* **108**: 4046-4052.

199. Zhu, Y., et al. (2002). "Abnormal Vascula Function and Hypertension in Mice Deficient Esrogen Receptor b." *Science* **295**(505): 505-508.

200. Zhuang, Y. X., et al. (2009). "Growth and Properties of Self-assembled Monolayers on Metals." *Journal of Physics: Conference Series* **152**.

Chapter 8 APPENDIX

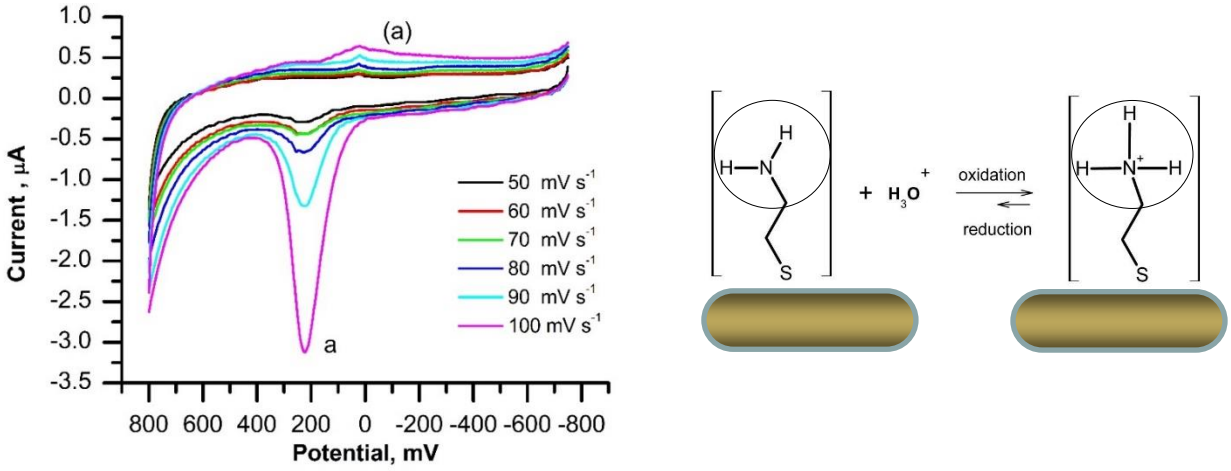

Figure 83: The cystamine modified gold electrode surfaces in 0.1 M phosphate buffer solution of pH 7.4 at different scan rates from 50 mV/s to 100 mV/s at 25 °C.

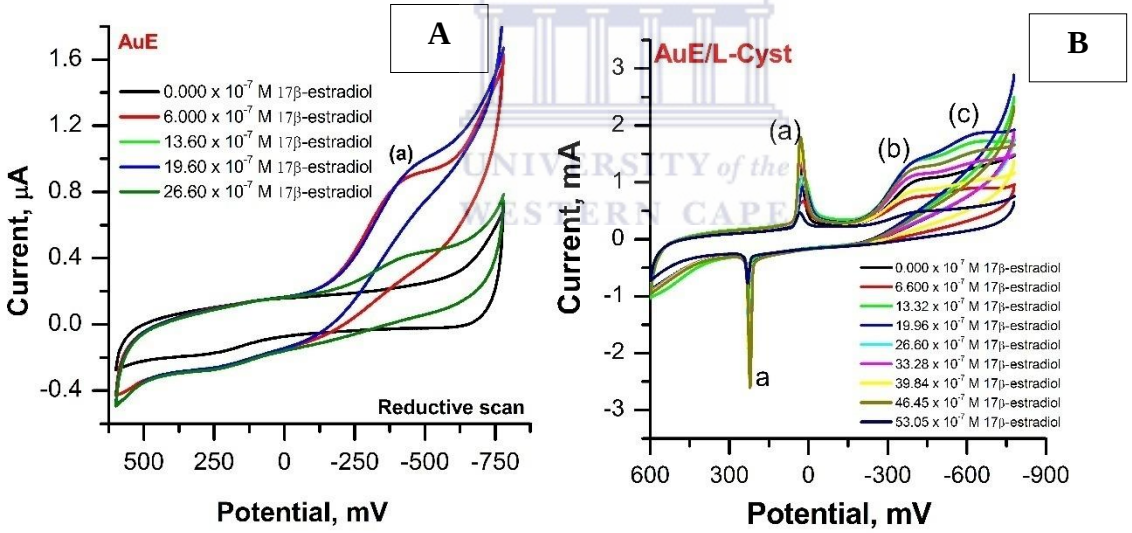

Figure 84: The electrochemical activity of the (**A**) bare (i.e. AuE) and (**B**) L-cysteine modified gold electrode in 0.1 M phosphate buffer solution of pH 7.4 at 30 mV/s, 25 °C, in the presence of different concentrations of 17β-estradiol.

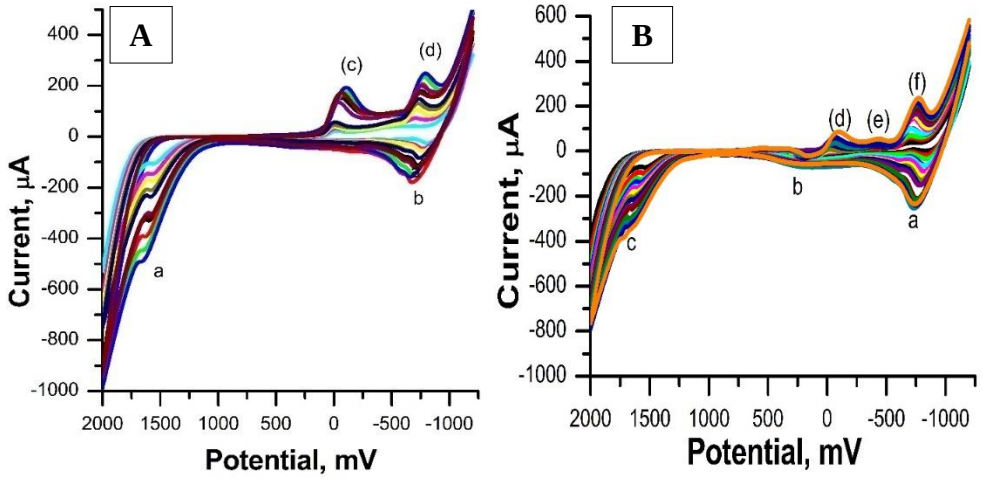

Figure 85: The cyclic voltammetry responses of the; (**A**) bare platinum electrode and (**B)** SnSe(3-MPA) quantum dots functionalised platinum electrode, in 0.1 M phosphate buffer of pH of 7.4 at scan rates between 5 mV/s and 60 mV/s, at 25 °C.

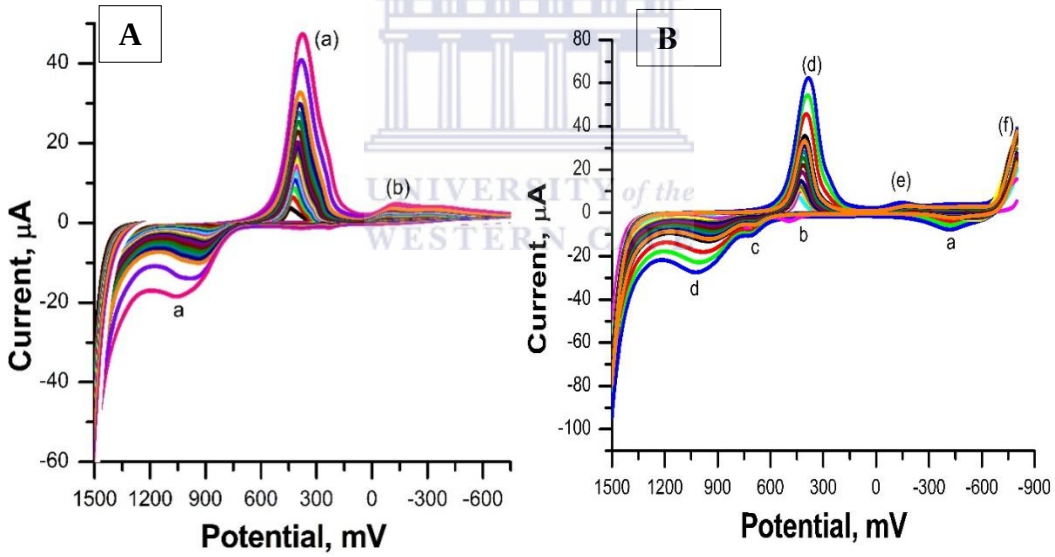

Figure 86: The cyclic voltammetry responses of; (**A**) the bare gold and (**B**) the gold electrode modified with SnSe(3-MPA) quantum dots at scan rates between 2 mV/s and 250 mV/s in 0.1 M phosphate buffer solution of pH = 7.4 at 25 °C.

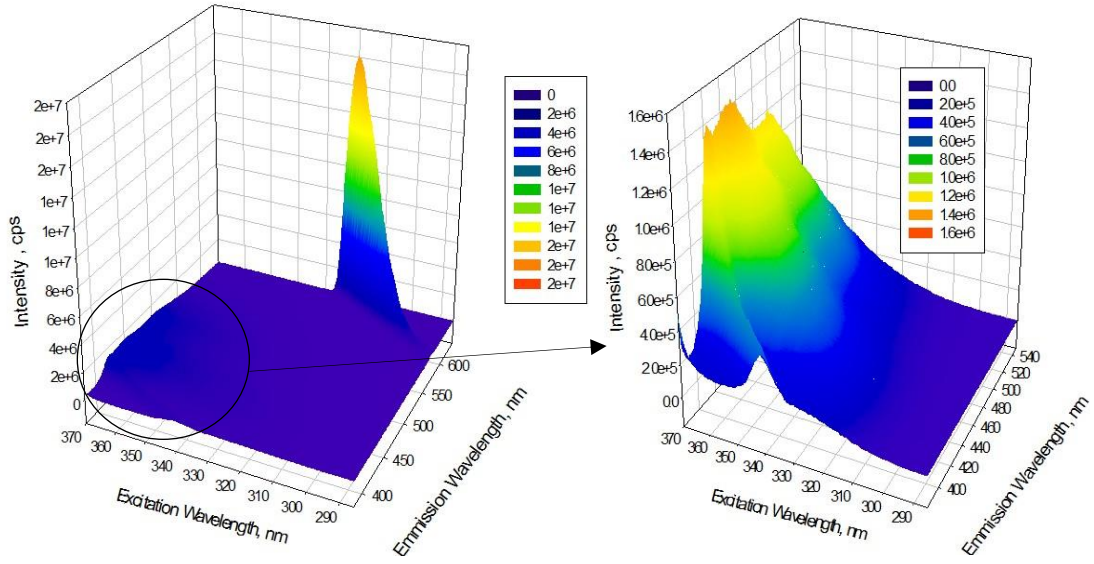

Figure 87: The 3D fluorescence studies of the SnSe(3-MPA) quantum dots films in 0.1 M phosphate buffer solution of pH 7.4.

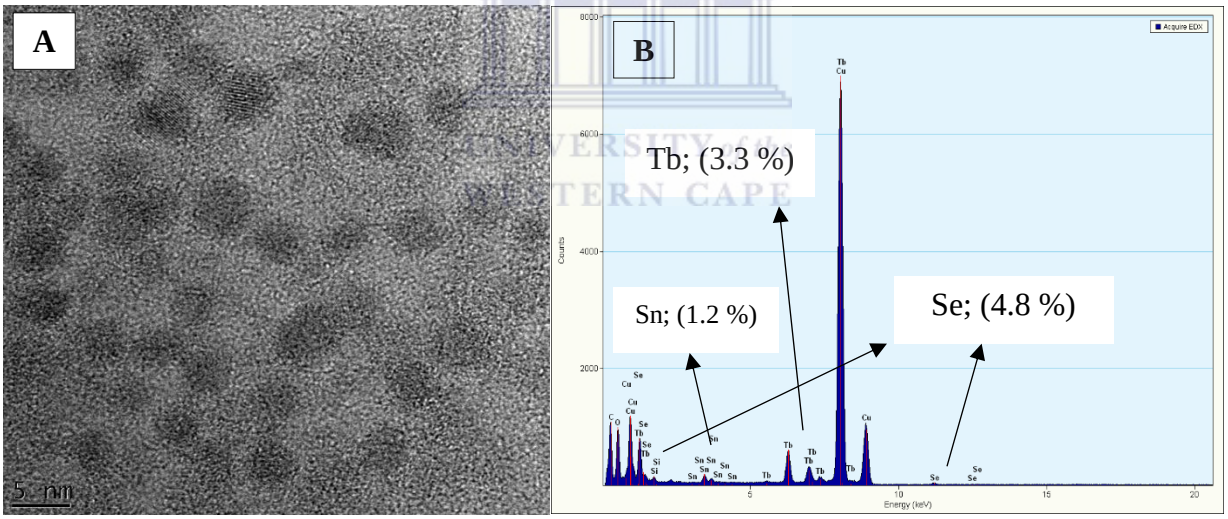

Figure 88: The (**A**) transmission electron microscopy (TEM) images and (**B**) electron dispersive X-ray (EDX) spectrum of: the terbium alloyed tin selenide quantum dots capped with 3-mercaptopropionic acid {i.e. Tb-SnSe(3-MPA)}.

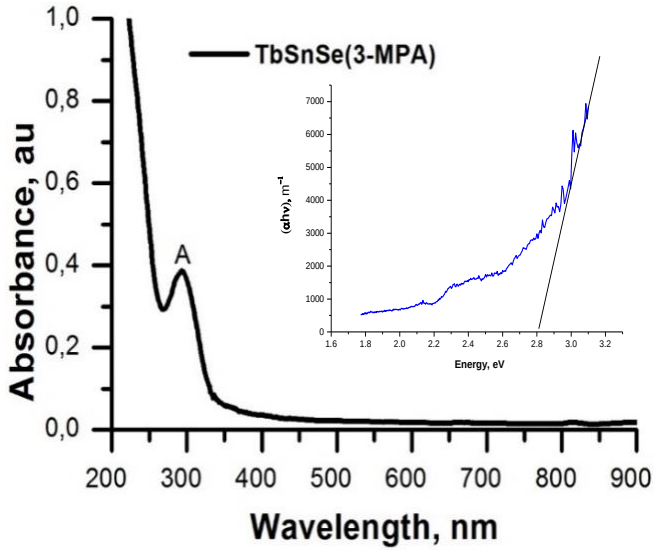

Figure 89: The ultra-violet to visible (UV-Vis) spectrum of the Tb-SnSe(3-MPA) alloyed quantum dots, and (i.e. insert) the related photon energy estimation of the indirect band gap of the Tb-SnSe(3-MPA) quantum dots.

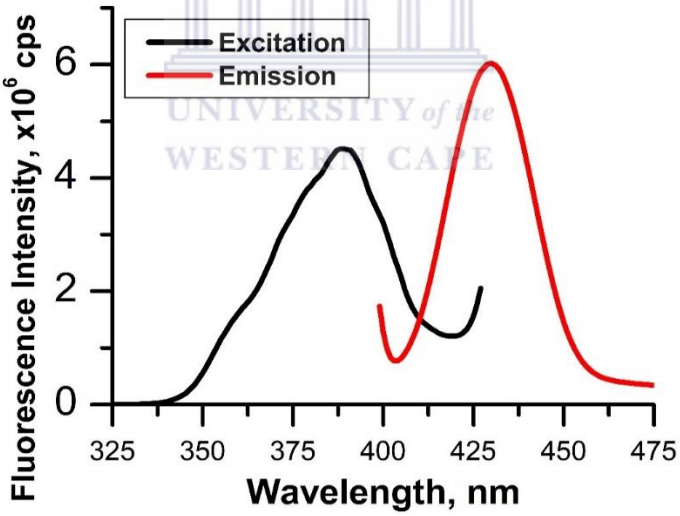

Figure 90: The fluorescence excitation and emission profiles of the Tb-SnSe(3-MPA) quantum dots .

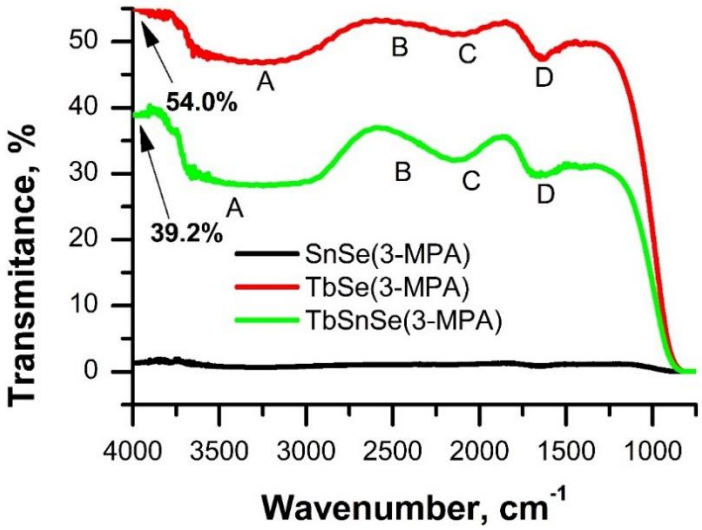

Figure 91: The Fourier transform infrared (FTIR) spectra of; SnSe(3-MPA) (i.e. **BLACK**), TbSe(3-MPA) (i.e. **RED**) and Tb-SnSe(3-MPA) (i.e. **GREEN**), quantum dot films.

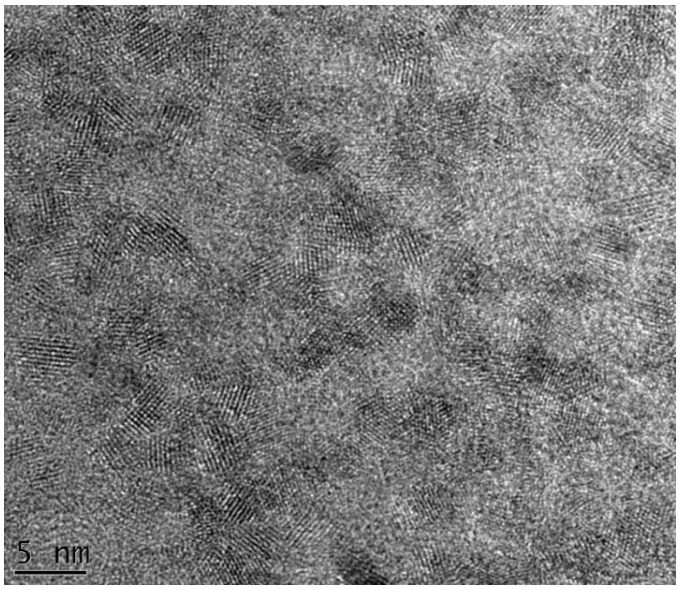

Figure 92: The TEM image of the mercaptosuccinic acid capped tin selenide quantum dots {i.e. SnSe(MSA) quantum dots}.

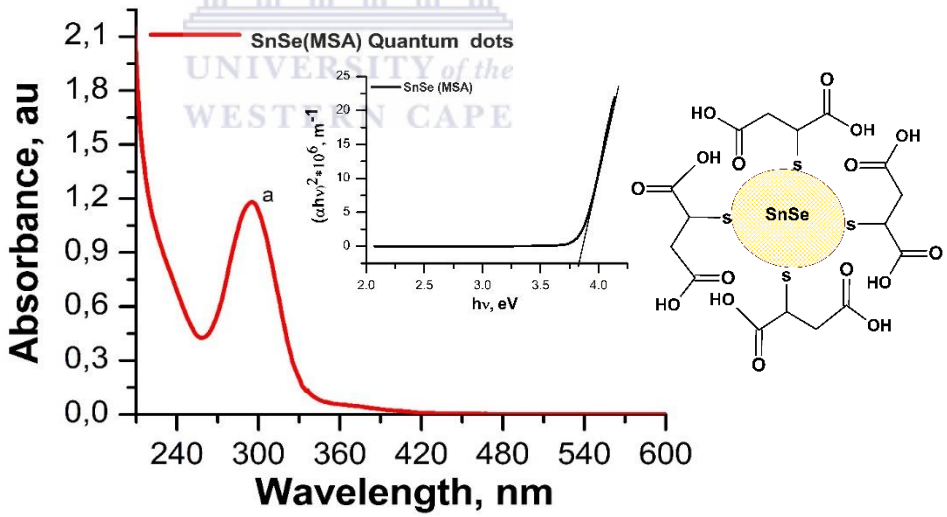

Figure 93: The UV-Vis absorption profile of the SnSe(MSA) quantum dots.

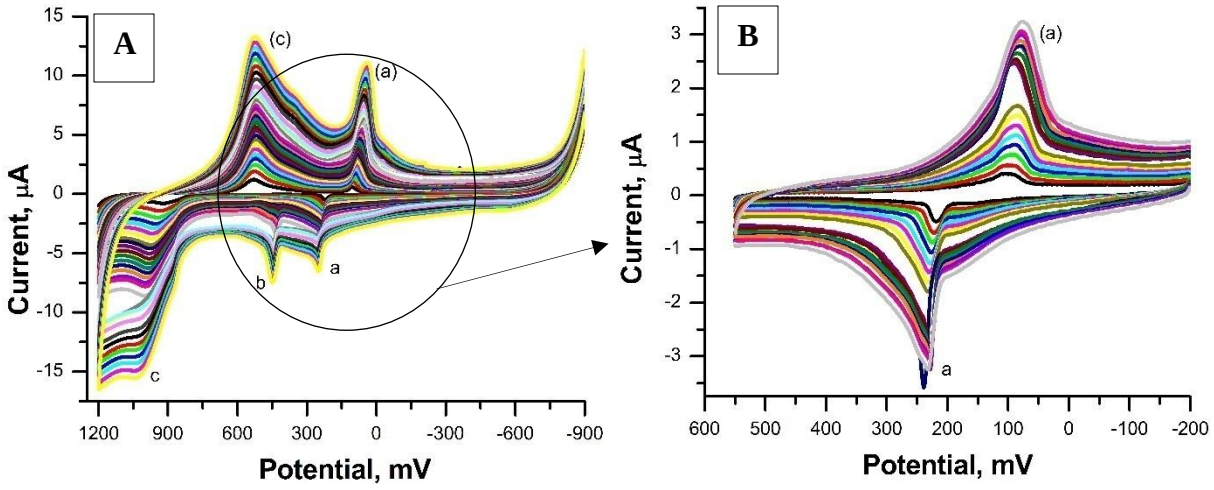

Figure 94: The cyclic voltammetry profiles of the SnSe(MSA) quantum dots, modified on the gold electrode surface in 0.1 M phosphate buffer solution, of pH 7.4 at different scan rates between 5 mV/s to 250 mV/s, at the potential windows between; (**A**) 1200 mV to -900 mV and (**B**) from 600 mV to -200 mV.

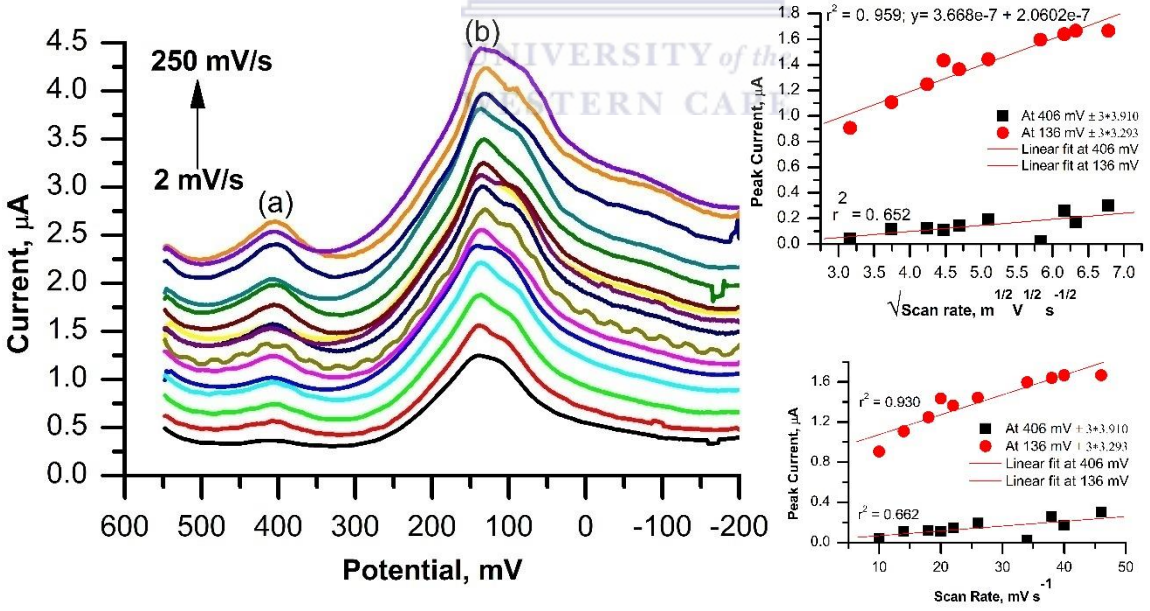

Figure 95: The O-square-wave voltammetry studies of the SnSe(MSA) quantum dots in 0.1 M phosphate buffer solution of pH 7.4 at different scan rates between 5 mV/s to 250 mV/s.

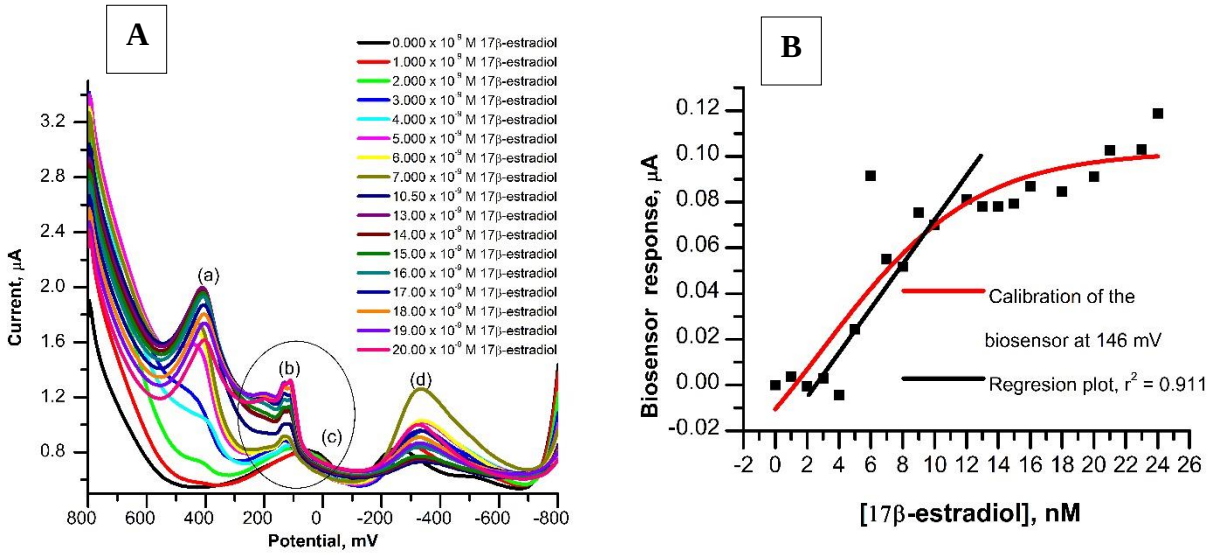

Figure 96: (**A**) The recycled ER-α/SnSe(3-MPA)/L-cysteine/AuE biosensor surfaces; responses at different concentrations of the 17β-estradiol in 0.1 M phosphate buffer solution of pH = 7.4, at a scan rate of 30 mV/s and (**B**) the corresponding calibration plot of the biosensor.

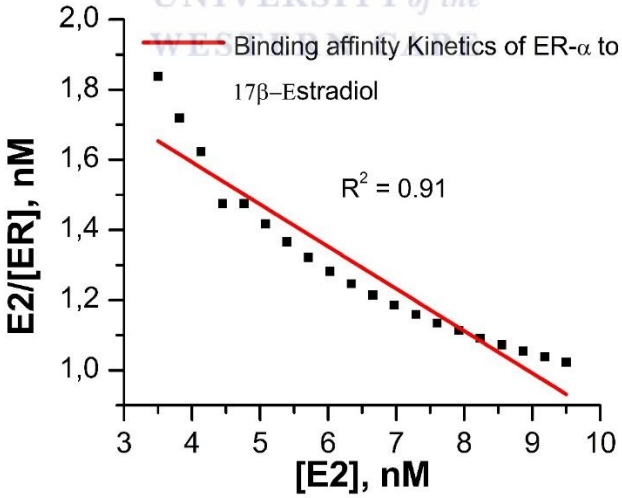

Figure 97: The kinetic binding affinity curve of the biosensor reactive surface; ER-α/SnSe(3-MPA)/L-cysteine/AuE.